Ion Irradiation Effects on Two-Dimensional Layered Materials

by

Tan Shi

A dissertation submitted in partial fulfillment
of the requirements for the degree of
Doctor of Philosophy
(Nuclear Engineering and Radiological Sciences)
in the University of Michigan
2020

Doctoral Committee:

Professor Igor Jovanovic, Chair
Professor Fei Gao
Professor Zhong He
Associate Professor Emmanuelle Marquis

Tan Shi

tanshi@umich.edu

ORCID ID: 0000-0001-9813-2148

© Tan Shi 2020

All Rights Reserved

ACKNOWLEDGEMENTS

First of all, I would like to express my deepest appreciation to my committee chair Prof. Igor Jovanovic. I would not be able to come to study at the University of Michigan without your trust and support, and this dissertation would not have been possible without your patient guidance and concrete suggestions. Next, I would like to express my sincere gratitude to our collaborators Prof. Joshua Robinson and Prof. Saptarshi Das at the Pennsylvania State University for the guidance on two-dimensional material characterization and transistor device testing. Our collaborations will not be successful without your dedicated support. I would like to express my greatest appreciation to my committee member Prof. Fei Gao, who provides me tremendous help in molecular dynamics simulations. I also would like to thank postdoctoral researcher Dr. Qing Peng for the concrete advice on material simulations. In addition, I would like to thank my committee members Prof. Zhong He and Prof. Emmanuelle Marquis for the thoughtful comments and suggestions on my dissertation work.

Throughout my Ph.D. studies, I learned tremendously from all the competent colleagues. I would like to specifically thank my research partner Roger Walker and Andrew Arnold for the time and effort you put into our research projects. Also, I would like to thank Prof. M.-W. Lin, Dr. Jason Nattress, Dr. Kyle Hartig, Kristofer Ogren, Tingshiuan Wu, as well as all the other group members for your feedback and suggestions on my research.

I also would like to thank the support from the funding sources. This work has

been partially supported by the United States Defense Threat Reduction Agency through Grant No. HDTRA1-14-1-0037, and Rackham Graduate Student Research Grant at University of Michigan. The material simulation work has been supported in part through computational resources and services provided by Advanced Research Computing at the University of Michigan. I also would like to thank the staff of the Michigan Ion Beam Laboratory and the Penn State Materials Characterization Laboratory for their assistance in carrying out the irradiation experiments and material characterization.

Finally, I would like to thank my family, especially my wife, my parents, my grandparents, my aunt, and my mother- and father-in-law for their unconditional support throughout these years.

TABLE OF CONTENTS

ACKNOWLEDGEMENTS ii

LIST OF FIGURES vi

LIST OF TABLES xv

LIST OF APPENDICES xvi

LIST OF ACRONYMS xvii

ABSTRACT xix

CHAPTER

I. Interactions Between Ions and Two-Dimensional Materials . 1

1.1 Introduction to two-dimensional materials 1
1.2 Motivation and scope of the study 3
1.3 Fundamentals of ion-matter interactions 6
1.3.1 Interatomic potentials 6
1.3.2 Ion energy loss through matter 11
1.4 Ion damage and modification of two-dimensional materials . . 13
1.5 Organization of the dissertation 15

II. Molecular Dynamics Simulation of Proton Irradiation of Graphene 17

2.1 Introduction 17
2.2 Methods 19
2.2.1 Methods for *ab-initio* MD simulations 19
2.2.2 Methods for classical MD simulations 22
2.3 Results and discussion 25
2.3.1 Defect structures and defect generation probabilities from *ab-initio* MD simulations 25

2.3.2 Defect structures and defect generation probabilities from classical MD simulations 30
2.3.3 Comparison of results from *ab-initio* and classical MD simulations 37
2.3.4 Proton irradiation at oblique angles 39
2.3.5 Discussion 46
2.4 Summary 49

III. Proton and Heavy Ion Irradiation of Layered WSe_2 50

3.1 Introduction 50
3.2 Methods 51
3.3 Results and discussion 54
3.3.1 Proton irradiation of exfoliated WSe_2 54
3.3.2 Proton irradiation of MOCVD-grown WSe_2 63
3.3.3 Heavy-ion irradiation of exfoliated WSe_2 73
3.4 Summary 80

IV. Ion Irradiation of MoS_2 Field-Effect Transistors 82

4.1 Introduction 82
4.2 Methods 85
4.2.1 Experimental procedure 85
4.2.2 Simulation methodology 87
4.3 Results and discussion 96
4.3.1 Helium ion irradiation of MoS_2 field-effect transistors 96
4.3.2 Proton irradiation of MoS_2 field-effect transistors . . 101
4.3.3 Defect structures and generation probabilities from classical MD simulations 104
4.4 Summary 111

V. Conclusions and Future Work 116

5.1 Summary and conclusions 116
5.2 Future work 120

APPENDICES 122

BIBLIOGRAPHY 134

LIST OF FIGURES

Figure

1.1 Atomic structure of (a) graphene and (b) TMD with a representative material of monolayer MoS_2 shown. 2
1.2 Potential as a function of the interatomic distance. 7
1.3 Ion trajectory after collision with a target atom. The impact parameter b is defined in the schematic trajectory. 9
2.1 (a) The studied system in the SIESTA simulation. The position of the hydrogen atom was sampled in the blue rectangular triangle based on the structure symmetry. (b) The studied system in the LAMMPS simulation. For oblique incidence of the hydrogen atom, the polar and azimuthal angles are defined in the figure. 20
2.2 Defect types as a function of the impact position of the proton for an incident energy of (a) 0.1 keV, (b) 1 keV, (c) 10 keV, and (d) 100 keV at a vertical incident angle simulated with the *ab-initio* MD code SIESTA. The origin of the polar coordinate system is the position of the selected carbon PKA and the marker positions correspond to the impact positions of the proton. For defect configurations with no, one, two, three and four atoms being ejected out of the simulation system, they are labeled as FP (purple), SV (blue), DV (green), TV (orange), and QV (pink), respectively. 26
2.3 Different types of defects obtained from the SIESTA simulations for no (FP), one (SV), two (DV), three atoms (TV), and four atoms (QV) ejected from the simulation box after proton irradiation. The defect configurations labeled in Figure 2.2 are shown in this figure. . 28
2.4 Defect types as a function of the impact position of the proton for an incident energy of (a) 0.1 keV, (b) 1 keV, (c) 10 keV, and (d) 100 keV at normal incidence simulated with the LAMMPS code. The origin of the polar coordinate system is the position of the selected carbon PKA and the marker positions correspond to the proton impact positions. For defect configurations with no, one, two, three, four, and five atoms being ejected out of the simulation system, they are labeled as FP (purple), SV (blue), DV (green), TV (orange), QV (pink), and PV (yellow), respectively. 31

2.5 Different types of defects defined in Figure 2.4 for no (FP), one (SV), and two atoms (DV) ejected from the simulation box after proton irradiation. The defect types obtained from the LAMMPS code were classified based on the positions of the vacancies and interstitials. . 32
2.6 Defect types as a function of the impact position of the proton for an incident energy of (a) 0.2 keV, (b) 0.5 keV, (c) 2 keV, (d) 5 keV, (e) 20 keV, and (f) 50 keV at normal incidence simulated with the LAMMPS code. For defect configurations with no, one, two, three and four atoms being ejected out of the simulation system, they are labeled as FP (purple), SV (blue), DV (green), TV (orange), and QV (pink), respectively. 35
2.7 The generation probabilities of different types of defects calculated from the SIESTA and LAMMPS simulations. 36
2.8 The number of sampled ion positions for different proton energies at a normal incidence angle simulated with the LAMMPS code. The defect generation probabilities presented in Figure 2.4 were determined based on the number of sampled positions shown here. 37
2.9 The generation probabilities of different types of defects as a function of the azimuthal angle of the incident proton at an energy of 10 keV for a polar angle of (a) 30° and (b) 75°. 40
2.10 Defect types as a function of the impact position of the proton for an incident energy of 10 keV at different azimuthal incident angles. The study was performed at a polar angle of 30° and 75°. At a polar angle of 30°, the results for an azimuthal angle of (a) 30° and (b) 75° are shown here. At a polar angle of 75°, the results for an azimuthal angle of (c) 30° and (d) 75° are shown here. The relationships between the incident angle, impact position and graphene structure lead to the differences shown in this figure. 41
2.11 Example of TV formation dynamics. The PKA first hits the brown carbon atom and then hits the pink carbon atom. All three atoms are ejected from the graphene surface at the end. The red arrow shows the direction of the PKA. 42
2.12 The generation probabilities of (a) SV, (b) DV, and (c) multiple vacancies (more than DV) as a function of the polar angle of the incident proton. 44

2.13 Defect types as a function of the impact position of the proton at different incident angles. At an incident energy of 1 keV, the results are shown for a polar angle of (a) 30° and (b) 60°, respectively. At an incident energy of 100 keV, the results are shown for a polar angle of (c) 30° and (d) 60°, respectively. The azimuthal angle was randomly sampled between 30° and 90° due to the crystal symmetry. The SV probability increases with the polar angle, as manifested by an elongated impact area along the proton direction. At 1 keV, a significant increase in the DV probability can be observed from (a) to (b). In comparison, there is only a moderate change at 100 keV, as shown from (c) to (d). 45
2.14 Defect types as a function of the impact position of the proton for an incident energy of 2 MeV at normal incidence simulated with the LAMMPS code. For defect configurations with no, one, two, three, four, five, seven, and nine atoms being ejected out of the simulation system, they are labeled as FP, SV, DV, TV, QV, PV, 7V, and 9V, respectively. 48
3.1 The stability of the exfoliated flakes in (a) medium vacuum and (b) air has been demonstrated via XPS. The two peaks in the W $4f_{7/2}$ window both correspond to WSe_2. No significant tungsten oxide formation was found to occur within the time frame of these measurements. The initial W $4f_{7/2}$ positions and shifts were (a) 32.35 eV, + 0.01 eV; (b) 32.31 eV, + 0.09 eV. 55
3.2 The binding energy shift of the W $4f_{7/2}$ peak position (∼35 eV) as a function of proton fluence. Data points at zero fluence correspond to control samples. 55
3.3 The binding energy shift of the Se $3d_{5/2}$ peak position (∼54 eV) as a function of proton fluence. 56
3.4 The binding energy shift of O 1s peak position (∼532 eV) from surface oxygen as a function of proton fluence. 56
3.5 The depth profile of ionization and dpa in SiC estimated from the SRIM/TRIM simulation. (a) Ionization depth profile of 2-MeV proton in SiC; (b) dpa of 2-MeV proton in SiC at 10^{17} protons/cm^2. The monolayer collisions calculation type was used in the SRIM/TRIM simulation. 57
3.6 VBO between WSe_2 and SiC in the WSe_2/SiC heterostructure. The VBO was calculated using XPS spectra and was found to decrease after proton irradiation. It is assumed that the bandgap was not modified by the proton beam exposure (CBM: conduction band minimum). 59

3.7 XPS spectra used in the calculation of VBO between WSe_2 and SiC upon exposure with 2-MeV protons at a fluence of 10^{16} protons/cm^2. The VBO between WSe_2 and SiC in the WSe_2/SiC heterostructure can be calculated using XPS by determining the binding energy difference between (a) W 4f and (b) Si 2p in WSe_2/SiC heterostructure, energy difference between (c) W 4f and (e) valence band edge in bulk WSe_2, and energy difference between (d) Si 2p and (f) valence band edge in bulk SiC. 60
3.8 UV-Vis-NIR spectra before and after 2-MeV proton irradiation at a fluence of 10^{16} protons/cm^2. (a) The measured UV-Vis-NIR spectra reveal irradiation-induced changes in the optical properties of the SiC substrate. Magnified regions of the plot (a) depict the changes in the absorption edge corresponding to (b) the SiC bandgap and (c) the new absorption edge created around 1.1 eV due to the irradiation-induced vacancy-rich region deep in the SiC substrate. 62
3.9 Binding energy shifts induced in the Se 3d and W 4f peaks of the exfoliated and MOCVD WSe_2 samples by exposure to 2-MeV protons at various fluence levels. 66
3.10 Binding energy shifts induced in the C 1s and Si 2p peaks of the SiC substrates by exposure to 2-MeV protons at various fluence levels. . 67
3.11 Energy loss of protons as a function of proton energy at the WSe_2 and SiC surface and penetration depth of protons within SiC substrate estimated with SRIM/TRIM simulation [1]. 200-keV and 2-MeV protons were used in our experiment. 200-keV protons have a shorter range in the substrate but have a higher stopping power compared with 2-MeV protons. 68
3.12 (a) Binding energy shifts induced in the Se 3d and W 4f peaks of the exfoliated and MOCVD WSe_2 by exposure to 200-keV protons at a fluence of 10^{16} protons/cm^2. (b) Binding energy shifts induced in the C 1s and Si 2p peaks of the SiC substrates by exposure to 200-keV protons at a fluence of 10^{16} protons/cm^2. Data from control samples is provided for comparison in both plots. Two exfoliated samples and one MOCVD sample were irradiated. Data from control samples is provided for comparison in both plots. Four exfoliated control samples and four MOCVD control samples were used. . . . 69
3.13 (a) Schematic band alignment between exfoliated WSe_2 and SiC. The bulk bandgap of WSe_2 is used due to the thick nature of the exfoliated flakes. (b) Schematic band alignment between MOCVD WSe_2 and SiC. The single layer bandgap value of WSe_2 is used due to the ultra-thin nature of MOCVD grown material. (c) Shifts in the valence band offset between WSe_2 and SiC induced by exposure to protons at a fluence of 10^{16} protons/cm^2. Several control samples were also analyzed and averaged together. 71

3.14 The depth profile of ionization and dpa in SiC estimated from the SRIM/TRIM simulation. (a) Ionization depth profile of heavy ions in SiC; (b) dpa of heavy ions at a fluence of 10^{16} protons/cm^2. The monolayer collisions calculation type was used in the SRIM/TRIM simulation. 74
3.15 The change of XPS W 4f spectrum after heavy-ion irradiation with (a) 2.5-MeV Fe, (b) 5-MeV Fe, and (c) 4-MeV Ag ions at a fluence level of 10^{16} ions/cm^2. The XPS spectrum intensity is expressed in the units of counts per second (CPS). The appearance of two additional peaks at ∼36 eV and ∼38 eV after irradiation indicates the oxidation of tungsten. 75
3.16 The change of XPS Si $2p_{3/2}$ spectrum after heavy-ion irradiation with (a) 5-MeV Fe, (b) 2.5-MeV Fe, and (c) 4-MeV Ag ions at a fluence of 10^{16} ions/cm^2. The appearance of new peak indicates the oxidation of silicon. 76
3.17 Compositional analysis of WSe_2/SiC heterostructure from XPS studies. The compositional ratio of C:Si, Se:W, SiO_x:SiC and WO_x:WSe_2 of WSe_2/SiC heterostructure before and after heavy-ion irradiation. No oxidation of silicon and tungsten has been detected before irradiation. 78
3.18 The change of XPS spectrum near the valence band region after heavy-ion irradiation with (a) 2.5-MeV Fe, (b) 5-MeV Fe, and (c) 4-MeV Ag ions at a fluence of 10^{16} ions/cm^2. 79
4.1 Schematic of the device fabrication and irradiation procedure. The irradiated and unirradiated components are painted in blue and green, respectively. (a) In the standard approach the entire FET device is irradiated. (b) The substrate and MoS_2 flakes are irradiated. The contacts are fabricated after the irradiation. (c) The MoS_2 flakes are irradiated and then transferred to a new substrate for device fabrication. (d) The substrate is irradiated and new MoS_2 flakes are exfoliated onto the irradiated substrate for device fabrication. (e) PMMA-assisted wet flake transfer process. The flakes are first coated with PMMA and then removed from the substrate in a NaOH bath. Next, the PMMA and flakes are rinsed in deionized water and transferred to a new substrate. The PMMA is then removed by acetone, leaving the irradiated MoS_2 flakes on the new substrate. 86

4.2 (a) Top and side view of the simulated system in the LAMMPS code. The system consists of 1512 MoS_2 atoms and one incident ion (in red). The S atoms in the top and bottom layer are distinguished by yellow and orange color, respectively. The Mo atoms (in blue) are located in the middle layer in the side view. (b) Two ion position sampling schemes were used based on the critical ion impact radius. When the ion energy is low, ion impact positions were uniformly sampled in a MoS_2 unit cell (area contoured by the dashed line). When the ion energy is high, impact positions were uniformly sampled within a circle around the Mo atom and two overlapped circles around the S atoms (areas contoured by the solid line). 88
4.3 Energy transfer between Mo and S atoms as a function of the ion impact position with the ZBL, REBO, and combined ZBL/REBO potential. For a Mo ion incident on a Mo PKA, the energy transfer is shown for an ion kinetic energy of (a) 0.1 keV, (c) 10 keV, and (e) 1000 keV. For a S ion incident on a S PKA, the energy transfer is shown for an ion kinetic energy of (b) 0.1 keV, (d) 10 keV, and (f) 1000 keV. 91
4.4 MoS_2 defect formation energies with the REBO potential. V_S and V_{Mo} represent single S and Mo vacancy, respectively. $V_{2S,\ neighbor}$ corresponds to two missing neighbor S atoms at the same layer. $V_{2S,\ top\text{-}bottom}$ corresponds to a S vacancy at the bottom of another top S vacancy. V_{3S} corresponds to three S vacancies at the same layer next to the same Mo atom. V_{MoS3} is a V_{3S} plus a Mo vacancy in the center. V_{MoS6} is a vacancy cluster with one Mo atom and six neighboring S atoms. Mo_{S2} corresponds to a Mo antisite occupying a $V_{2S,\ top\text{-}bottom}$ site. $S2_{Mo}$ corresponds to two S atoms occupying a Mo site. The defect formation energies based on first-principles calculations from KC *et al.* [2] and Zhou *et al.* [3] are also shown. 93
4.5 Radiation damage due to He^+ exposure. Representative transfer characteristics of MoS_2 FETs from an unirradiated control sample with neither the flakes nor the substrate being irradiated, and post radiation samples with both the flake and the substrate irradiated (BI), only the flake irradiated (FI), and only the substrate irradiated (SI). 390-keV He^+ ions were used at a total fluence of (a)-(d) 10^{14} ions/cm^2, (e)-(h) 10^{15} ions/cm^2, and (i)-(l) 10^{16} ions/cm^2. 96
4.6 Statistical analysis of He^+ irradiation at a fluence of 10^{15} ions/cm^2. Overlaid transfer characteristics of all MoS_2 FETs correspond to (a) control samples (CS), (b) samples with both flakes and substrate irradiated (BI), (c) samples with flakes irradiated (FI), and (d) samples with substrate irradiated (SI) at a fluence of 10^{15} He^+ ions/cm^2. (e) Mean and standard deviation of subthreshold slope, threshold voltage, and field effect electron mobility for all four sample configurations. 98

4.7 Statistical analysis of proton irradiation. Overlaid transfer characteristics of all MoS_2 FETs correspond to (a) control samples (CS), (b) samples with both flakes and substrate irradiated (BI), (c) samples with flakes irradiated (FI), and (d) samples with substrate irradiated (SI) at a fluence of 1.26×10^{16} protons/cm^2. (e) Mean and standard deviation of subthreshold slope, threshold voltage, and field effect electron mobility for all four sample configurations. 102
4.8 (a) Sputtering yields of Mo and S atoms per incident He ion as a function of the He ion energy. The sputtering yields of S atoms in the top and bottom layer of a monolayer MoS_2 are labeled with R_{S_top} and R_{S_bottom}, respectively. (b) Probability of defective sites per incident He ion as a function of the He ion energy. 106
4.9 Sputtering yields of (a) Mo atoms, (b) top layer S atoms, and (c) bottom layer S atoms are classified by the atom species of the PKA. . . 107
4.10 Probability of defect size as a function of the number of sputtered Mo (X-axis) and S atoms (Y-axis) for a He energy of (a) 0.1 keV, (b) 1 keV, (c) 10 keV, (d) 100 keV, (e) 1000 keV, and (f) 2000 keV. The probability of zero sputtered Mo and S atom corresponds to the probability of structural disorder without atom being ejected. The scale for the color map is 1×10^{-5} to 1 in (a), 1×10^{-6} to 1×10^{-1} in (b) and (c), and 1×10^{-7} to 1×10^{-2} in (d)–(f). 109
4.11 (a) Sputtering yields of Mo and S atoms per incident proton as a function of the proton energy. The sputtering yields of S atoms in the top and bottom layer of a monolayer MoS_2 are labeled with R_{S_top} and R_{S_bottom}, respectively. (b) Probability of defective sites per incident proton as a function of the proton energy. 112
4.12 Sputtering yields of (a) Mo atoms, (b) top layer S atoms, and (c) bottom layer S atoms are classified by the atom species of the PKA. . . 113
4.13 Probability of defect size as a function of the number of sputtered Mo (X-axis) and S atoms (Y-axis) for a proton energy of (a) 0.1 keV, (b) 1 keV, (c) 10 keV, (d) 100 keV, (e) 1000 keV, and (f) 2000 keV. The probability of zero sputtered Mo and S atom corresponds to the probability of structural disorder without atom being ejected. The scale for the color map is 1×10^{-6} to 1×10^{-2} in (a)–(c) and 5×10^{-8} to 5×10^{-4} in (d)–(f). 114
A.1 Optical image of exfoliated WSe_2. (a) Optical image of exfoliated WSe_2 flakes on 6H-SiC substrate taken by white light interferometry (optical profilometry). (b) Using this technique, the thickness of the WSe_2 flakes can also be measured. The thickness ranges from several layers to several microns. The sparse coverage of exfoliated material allows the substrate to be examined in XPS measurements. 123

A.2 Images of the exfoliated and directly grown WSe_2 flakes on the SiC substrate. (a) Optical image of exfoliated WSe_2 flakes on the SiC substrate; b) Image of MOCVD-grown WSe_2 flakes on the SiC substrate taken via scanning electron microscopy. Bright white streaks correspond to vertical growth of the WSe_2, leading to fins rather than flakes. 124
A.3 Proton-irradiated samples before and after irradiation. (a) Digital camera image of the TMD samples before irradiation. The samples are transparent due to the wide bandgap of SiC and the nanoscale dimensions of the WSe_2 and MoS_2. (b) Digital camera image of the TMD samples after proton irradiation. Control samples (unlabeled) and samples exposed to 10^{15} protons/cm^2 are mostly transparent. Samples exposed to 10^{16} protons/cm^2 and 10^{17} protons/cm^2 turn black due to proton beam damage. 124
A.4 Representative XPS survey spectra of the WSe_2/SiC heterostructures. (a) Survey spectrum of the WSe_2/SiC heterostructure generated via mechanical exfoliation of the WSe_2. (b) Survey spectrum of the WSe_2/SiC heterostructure generated via direct growth of the WSe_2 by MOCVD. Both spectra are presented without charge correction. The major elemental peaks are labeled here. A trace amount of sodium was also detected on the sample with the exfoliated WSe_2. It is noted that for the case of MOCVD growth of WSe_2, there is a prominent selenium Auger line that overlaps with the C 1s peak. . . 125
A.5 Representative initial core-level XPS spectra for WSe_2/SiC heterostructures. (a) High-resolution core-level spectra of the WSe_2/SiC heterostructure generated via mechanical exfoliation of the WSe_2. (b) High-resolution core-level spectra of the WSe_2/SiC heterostructure generated via direct growth of the WSe_2 by MOCVD. Spectra are charge corrected as discussed in the main text. Constituent compounds are labeled here. It is noted that for the case of MOCVD growth of WSe_2, there is a prominent selenium Auger line that overlaps with the C 1s peak. The signal from that line was separated from the C 1s signals using data from pristine bulk samples in the high-resolution data, and was subtracted from the spectra presented here. The background has also been subtracted in the spectra. . . . 126
A.6 Change of Oxygen 1s peak spectrum after heavy ion irradiation. O 1s spectra before (black) and after the irradiation (red) for sample exposed to the heavy ions. The initial oxygen spectra contain two chemical environments – one for adsorbed moisture and the other for organic contaminants. The final spectra contain those two peaks and a third peak corresponding to metal oxides. 127

C.1 Energy transfer between Mo and S atoms as a function of the ion impact position with the ZBL, REBO, and combined ZBL/REBO potential. For a Mo ion incident on a S PKA, the energy is shown for an ion kinetic energy of (a) 0.1 keV, (c) 10 keV and (e) 1000 keV. For a S ion incident on a Mo PKA, the energy is shown for an ion kinetic energy of (b) 0.1 keV, (d) 10 keV and (f) 1000 keV. 131
C.2 Probability of defect size as a function of the number of sputtered Mo (X-axis) and S atoms (Y-axis) for a He energy of (a) 0.33 keV, (b) 3 keV, (c) 30 keV, and (d) 300 keV. The probability of zero sputtered Mo and S atom corresponds to the probability of structural disorder without atom being ejected. The scale for the color map is 1×10^{-5} to 1 in (a), 1×10^{-6} to 1×10^{-1} in (b) and (c), and 1×10^{-7} to 1×10^{-2} in (d). 132
C.3 Probability of defect size as a function of the number of sputtered Mo (X-axis) and S atoms (Y-axis) for a proton energy of (a) 0.3 keV, (b) 3 keV, (c) 30 keV, and (d) 300 keV. The probability of zero sputtered Mo and S atom corresponds to the probability of structural disorder without atom being ejected. The scale for the color map is 1×10^{-6} to 1×10^{-2} in (a)–(c) and 5×10^{-8} to 5×10^{-4} in (d). . . 133

LIST OF TABLES

Table

2.1 Graphene defect generation probabilities induced by 2-MeV protons simulated with the LAMMPS code. 47

3.1 Initial binding energies of core level peaks for WSe_2 and SiC in a heterostructure. 64

3.2 Summary of the results from the SRIM/TRIM simulation. The dpa was calculated with a fluence of 10^{16} ions/cm^2 at the top 10 nm of the material, corresponding to the detection depth of XPS measurement. The monolayer collisions calculation type was used in the SRIM/TRIM simulation. The depth profiles of ionization and dpa in the SiC substrate induced by heavy ions are shown in Figure 3.14. . 74

4.1 Stopping powers and ranges of protons and He ions in the irradiated materials estimated from SRIM/TRIM [1]. A displacement threshold energy of 31.7 eV and 5.0 eV were used for Mo and S atoms, respectively [4]. 101

LIST OF APPENDICES

Appendix

A. Optical images and XPS spectra of ion-irradiated WSe_2 samples . . . 123

B. MoS_2 field-effect transistor device fabrication procedure 128

C. Supplementary simulation results on proton and helium ion irradiation of MoS_2 130

LIST OF ACRONYMS

2D material two-dimensional material

BI both the MoS_2 flakes and substrate irradiated

CBO conduction band offset

CMOS complementary metal-oxide-semiconductor

CS control samples

$\boldsymbol{D_{IT}}$ density of interface states

DFT density functional theory

dpa displacement per atom

DV double-vacancy

FET field-effect transistor

FI only the MoS_2 flakes irradiated

LJ Lennard-Jones

MD molecular dynamics

MOCVD metal organic chemical vapor deposition

$\mathbf{MoS_2}$ molybdenum disulfide

MOSFET metal–oxide–semiconductor field-effect transistor

PKA primary knock-on atom

PV penta-vacancy

QV quad-vacancy

REBO reactive empirical bond order

SEE single event effect

SEM scanning electron microscopy

SI only the SiO_2 substrate irradiated

SS subthreshold slope

SV single-vacancy

SW Stone-Wales

SY sputtering yield

TMD transition metal dichalcogenide

TV triple-vacancy

UV-Vis-NIR ultraviolet-visible spectroscopy

VBM valence band maximum

VBO valence band offset

$\boldsymbol{V_T}$ threshold voltage

$\mathbf{WSe_2}$ tungsten diselenide

XPS X-ray photoelectron spectroscopy

ZBL Ziegler-Biersack-Littmark

ABSTRACT

Two-dimensional materials (2D materials) refer to atomically thin layered crystalline materials with strong intralayer bonding and weak interlayer van der Waals bonding. Since the discovery of graphene, a single layer of graphite, in 2004, 2D materials have attracted great attention due to their attractive mechanical, chemical, and electronic properties. Among all 2D materials, semiconducting transition metal dichalcogenides (TMDs), such as molybdenum disulfide (MoS_2) and tungsten diselenide (WSe_2), have shown great promise for next-generation semiconductor devices. As the feature size in the state-of-the-art complementary metal-oxide-semiconductor (CMOS) technology is approaching its fundamental limit, TMD-based transistors offer a prospect for transistor downsizing and exhibit favorable electronic properties including high on-and-off current ratio, low subthreshold slope, and high mobility. However, for these atomically thin materials, where the ultimate limit of their thickness is a monolayer, it is not fully understood how ion irradiation affects their properties. First, ion radiation can be used as an effective tool to provide controlled modifications to 2D materials so that defect engineering and material functionalization can be realized. Second, due to their reduced size and power consumption, 2D material-based electronics holds promise for space applications, where the intensity of cosmic rays is high. Therefore, understanding radiation effects on 2D materials is crucial for their use in radiation-harsh environments. In this dissertation, for different 2D materials (graphene, WSe_2, and MoS_2), the impact of ion irradiation on material structure, surface chemistry, and electronic properties was studied by molecular dynamics (MD) simulations and ion irradiation experiments.

First, a comprehensive study of graphene defects induced by proton irradiation was performed by MD simulations. The defect generation probabilities at different proton energies were determined by classical MD simulations and validated by *ab-initio* MD simulations. It is shown that with increasing proton energy, defect structures transition from single vacancies to a rich variety of defect configurations. The defect probabilities also show large dependence on the proton incident angle, which, combined with the proton energy, can be used to effectively tune the ratios of generation probabilities of different defect structures. Next, X-ray photoelectron spectroscopy (XPS) was used to study the impact of ion irradiation on WSe_2 chemical and electronic properties. With 2-MeV protons, no detectable oxidation was observed even at a high fluence level of 10^{17} protons/cm^2. Starting from a fluence of 10^{16} protons/cm^2, charge transfer between WSe_2 and SiC substrate was observed due to a combination of radiation-induced defects and charge trapping in pre-existing defects. Lastly, the degradation of MoS_2 field-effect transistor (FET) electrical performance induced by high-energy protons and helium ions was studied at different fluences. By irradiating individual FET components, the damage to MoS_2 and SiO_2 dielectric was decoupled. The nuclear stopping power was shown to play an important role in the generation of interface states and structural defects. With 390-keV He ions, degradation of I-V characteristics became statistically significant at a fluence level of 10^{15} ions/cm^2. Nevertheless, a high on-state current and a high on-and-off current ratio were still maintained at this high fluence level, indicating a strong radiation resilience of MoS_2. MD simulations were also performed to study the defect generation probabilities and sputtering yields within monolayer MoS_2 as a function of the proton and helium ion energy. With increasing ion energy, larger defect size can be produced; however, point defects such as S vacancies are still the dominant defect structures.

CHAPTER I

Interactions Between Ions and Two-Dimensional Materials

1.1 Introduction to two-dimensional materials

2D materials represent a family of crystalline materials with strong intralayer bonding and weak interlayer van der Waals bonding. Due to their reduced dimensionality and unique structure, 2D materials show unusual mechanical [5, 6], chemical [7], electronic [8], and physical properties [9]. For example, graphene, a single layer of graphite (see Figure 1.1(a)), has the highest tensile strength and elastic modulus among all natural materials by virtue of its strong sp^2 covalent bonding [6]. Molybdenum disulfide (MoS_2) has extremely low hydrogen adsorption energy, which is promising for hydrogen evolution reaction in electrocatalysis [10, 11]. Since electron and phonon transport are confined in a planar space [9], 2D materials can exhibit excellent charge carrier mobility [12, 13] and high thermal conductivity [14, 15], according to both first-principles calculations and experiments. Also, tunable band structures of 2D materials can be achieved by doping [16], straining [17], heterostructures [18], and thickness tuning [7]. Transition metal dichalcogenide (TMD) monolayers also show excellent optical properties and can reach a 5–10% light absorbance in the visible range within sub-nanometer thickness [19]. Because of all these interesting

properties, 2D materials have found interesting applications in chemical sensing [20], catalysis [10], electronics [21], and photovoltaics [19].

One important research thrust associated with 2D materials is the development of ultra-thin transistors, with a goal to sustain the Moore's law of transistor downscaling. In 1975, Moore predicted that the total number of transistors in an integrated circuit would double every year before ∼1980 and would double approximately every two years after 1980. The actual trend followed this prediction or became even faster in the last 30–40 years until recently, when the pace of growth has slowed down. With reduced transistor size, gate control becomes more difficult and tunneling leakage current becomes more important as the device dimensions are reaching their physical limits. Therefore, a search is underway for alternative materials and device designs, including alternative channel materials and high-κ dielectrics, which could overcome the limits of the traditional silicon metal–oxide–semiconductor field-effect transistor (MOSFET) technology.

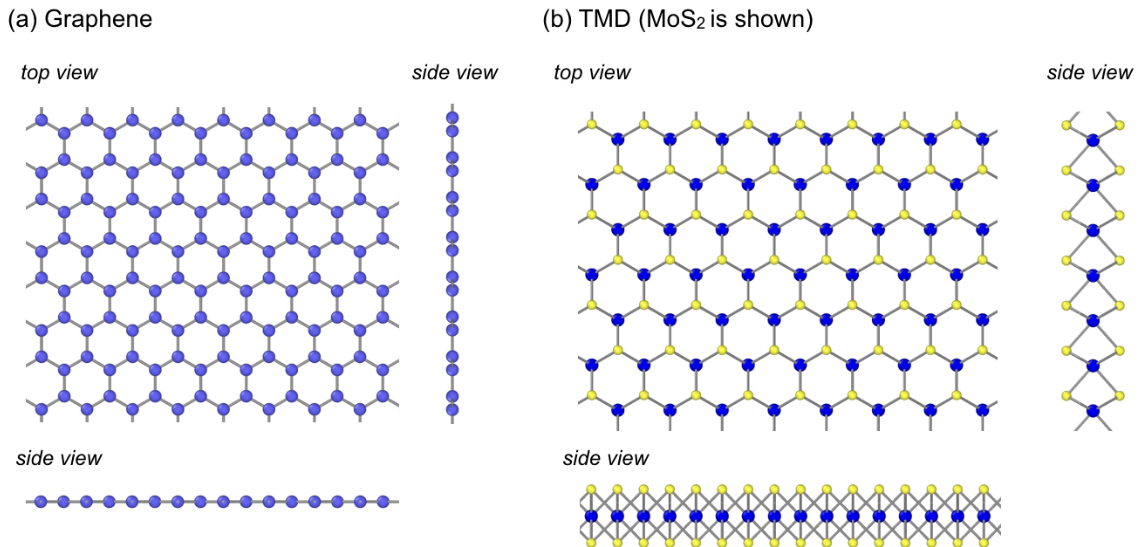

Figure 1.1: Atomic structure of (a) graphene and (b) TMD with a representative material of monolayer MoS_2 shown.

2D layered materials offer a prospect for further transistor downsizing, where the

ultimate limit is a single layer for the channel material. Graphene shows excellent charge mobility; however, it does not have a bandgap, which is why a graphene-based transistor cannot be effectively turned off. Although it is possible to open a bandgap in graphene by various routes [22, 23], the bandgap is usually small and there is also an associated tradeoff in mobility [24]. Among all 2D materials, 2D TMDs are semiconductors and are therefore promising candidates for digital electronics. TMDs is a group of materials consisting of one transition metal atom (*e.g.*, Mo, W, Ti) and two chalcogens atoms (S, Se or Te). TMDs have a general chemical formula of MX_2, where M represents the metal atom and X represents the chalcogen atom. Monolayer TMD has a hexagonal lattice structure with three atomic layers in which the metal layer is sandwiched by two layers of chalcogen atoms (see Figure 1.1(b)). Examples of TMD materials are MoS_2, $MoSe_2$, $MoTe_2$, WSe_2, WS_2, *etc.*. With the recent advances in device fabrication, single-layer MoS_2 field-effect transistor (FET) has been demonstrated in 2011 with good performance [25]. The mobility was found to be 200 cm^2 V^{-1} s^{-1} with a high on-and-off current ratio of 10^8. FET devices based on multilayer MoS_2 with similar or improved performance have also been fabricated [13]. Furthermore, MoS_2 FETs solely based on 2D materials with boron nitride as the high-κ dielectric have been demonstrated with an electron mobility of 33 cm^2 V^{-1} s^{-1} and an on-and-off ratio larger than 10^6 [26]. The inverter, NAND gate, and static random access memory have also been made with MoS_2 transistors as the basic building blocks [27].

1.2 Motivation and scope of the study

In order to better understand the potential for the use of 2D materials in extreme environments, this work is focused on the study of ion irradiation effects on 2D materials and 2D electronics. Although past studies of ion-induced effects on these materials have been reported, it is still not completely understood how high-energy

radiation would affect their properties. Fundamentally, the properties of 2D materials can differ from their bulk counterparts due to the reduced dimensionality. For most applications, 2D channel materials have a thickness ranging from monolayer to several layers. On one hand, reduced thickness leads to reduced interaction probability with the incident radiation. On the other hand, interaction probability per atom number density does not differ significantly from bulk materials since the microscopic cross sections do not change; however, more sputtering effects might be expected due to the larger surface-area-to-volume ratio. Furthermore, the presence of radiation-induced defects at or close to the interface between 2D and surrounding materials, such as substrates, could have a great impact on their intrinsic properties [9]. It is also unclear how energy is dissipated in 2D materials after energy deposition from the incident radiation. Thus, in order to better understand ion radiation effects, many questions remain to be answered.

In addition to the fundamental questions related to the damage mechanisms, this study was motivated by the following two applications. First, ion radiation can be used as an effective tool to provide controlled modification of 2D materials so that defect engineering and material functionalization can be realized. This is also known as the ion modification technique. With controlled radiation conditions, ions can be used to tune material properties and produce desirable defects. Therefore, understanding ion irradiation effects is important for providing new routes for tailing 2D material properties. Second, 2D electronics are promising candidates for space applications due to their lower power consumption and weight. The component of cosmic rays in space which is intense and difficult to shield are protons and heavy charged particles. How these high-energy ions would damage 2D materials has not been studied in sufficient detail to date. In addition, there is also interest in using these materials in other radiation-harsh environment such as nuclear power systems and defense systems. While radiation effects on MOSFETs have been studied extensively

in the past [28, 29], similar assessment has yet to be performed for 2D materials.

In this dissertation, the impact of ion irradiation on material structure, surface chemistry and electronic properties was studied by molecular dynamics (MD) simulations and ion irradiation experiments. In order to understand the impact of ion irradiation on material properties, it is important to know the defect structures and their generation probabilities under different irradiation conditions. In this work, with graphene as a representative 2D material, the defect generation process was examined at various proton energies and incident angles through MD simulations. Protons were selected for this study because they are a major component of cosmic rays in outer space. Knowing the response at each proton energy and incident angle is essential in determining the aggregated proton irradiation damage in space, In addition, although proton irradiation experiments for different types of 2D materials have been performed in prior research [30–33], the defect structures are not clearly understood. The simulation results can provide useful microscopic information on the collision dynamics and defect generation process. Due to the lack of accurate interatomic potentials for new types of 2D materials, a novel simulation approach based on first principles was demonstrated so that the full dynamics of the ion interaction process can be modeled with an efficient position sampling scheme.

Next, TMD materials were studied due to their prospect for use in 2D electronics. The surface chemistry and electronic properties of WSe_2/SiC heterostructures were investigated using MeV-energy protons and heavy ions. From this study, the chemical stability of WSe_2 and the impact of ion irradiation on the WSe_2/SiC interface were examined. Lastly, electrical degradation of MoS_2 FETs was studied using a new irradiation and device fabrication procedure with protons and helium ions as probe particles. Although radiation effects on 2D FETs have been reported in the past [32, 34], it is sometimes difficult to isolate the impact of irradiation on standalone ultra-thin 2D layer due to the radiation damage to the dielectric. For dielectric of different

qualities and thicknesses, the results are not directly comparable between different studies. In this work, the MoS_2 channel layer and the SiO_2 dielectric were irradiated separately in order to understand the effects intrinsic to MoS_2. MD simulations were also performed to determine the probability of structural defects at experimental conditions and at a wide range of ion energies.

1.3 Fundamentals of ion-matter interactions

1.3.1 Interatomic potentials

The interactions between an incident ion and target atoms depend on the potential energy between the atoms. If the potential energy is known or can be approximated, force, acceleration, and energy transfer can all be computed accordingly. Interatomic potential functions are usually used to describe the system's potential energy. For example, in MD simulations, various formulations of potential functions are introduced to describe a range of material systems so that the material structure and movement of atoms can be modeled. The interatomic potentials can take different analytical forms representing different aspects of the interaction physics. Based on the number of atoms involved, the interatomic potentials can be classified into two groups: pair potential and many-body potential. The pair potential describes the interactions between two atoms, whereas many-body potential takes into account the interactions among multiple neighboring atoms simultaneously. For example, for a three-body potential, the effects of bond angle and bond order can be included so that the interatomic potential formalism can provide a better description of the bonding environment of a specific material structure.

Figure 1.2 shows a typical potential profile as a function of the interatomic distance r between two atoms. In the context of ion interactions, it corresponds to the potential between an incident ion and an atom within the target material. As shown

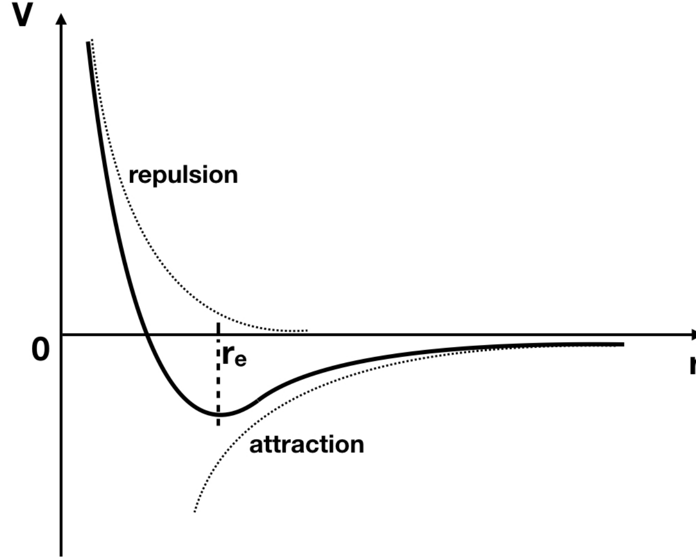

Figure 1.2: Potential as a function of the interatomic distance.

in Figure 1.2, repulsive force is dominant at small r while attractive force is dominant at large r. Here, r_e is defined as the equilibrium position where the force, the slope of the potential, is equal to zero. The range for r_e is around 0.15–0.3 nm [35]. In order to provide an estimation of the radius of the atomic shell, a second reference distance is used here: the Bohr radius of the hydrogen atom r_h, which has a value of 0.053 nm. Based on these two reference distances, different potential functions can be used to describe the potentials at different distances, according to the classification used in Ref. [35]. When $r > r_e$ and when the two atoms are getting closer, the outer electron shells start to overlap and an weak attractive force is manifested. When $r_h < r < r_e$, the inner electron shells start to overlap and the repulsion in this region can be described by the Born-Mayer potential [36]:

$$V(r) = C_1 \exp(-r/C_2), \tag{1.1}$$

where C_1 and C_2 are material-dependant constants. This potential provides a good approximation for an ion impact parameter that is close to r_e [35]. When $r < r_h$,

the nuclei are screened by the electrons in the inner shells. the screened Coulomb potential [37, 38] can be used to describe this range of separation distance:

$$V(r) = \left(\frac{Z_1 Z_2 q_e^2}{4\pi\epsilon_0 r}\right) \exp\left(-r/r_{sc}\right), \tag{1.2}$$

where q_e is the elementary charge, ϵ_0 is the vacuum permittivity, and the screening radius r_{sc} can be expressed as

$$r_{sc} = \left(\frac{9\pi^2}{128}\right)^{1/3} \frac{r_h}{(Z_1^{2/3} + Z_2^{2/3})^{1/2}}. \tag{1.3}$$

Here, Z_1 and Z_2 are the atomic number of the ion and the target atom, respectively. When $r \ll r_h$, the repulsive force between the two nuclei is dominant. The pure Coulomb potential can be used to describe the nuclei-nuclei interactions in this region:

$$V(r) = \frac{Z_1 Z_2 q_e^2}{4\pi\epsilon_0 r}. \tag{1.4}$$

The pure Coulomb potential can be considered as an extreme condition of the screened Coulomb potential with the exponential term to be unity. To the first approximation, for $r < r_e$, the total potential can be expressed as the sum of the Born-Mayer potential shown in Equation (1.2) and the screened Coulomb potential shown in Equation (1.2). However, it is worth noting that when r is approximately equal to r_h or slightly larger (between the Born-Mayer regime and screened Coulomb regime), there is no universal formalism that can be used to describe the interatomic interactions with great accuracy. Therefore, more sophisticated empirical potential functions are developed for different material systems with each of them having a certain range of applicability.

After the interatomic potential is defined, the energy transfer between an incident ion and a target atom can be determined. As shown in Figure 1.3, the impact param-

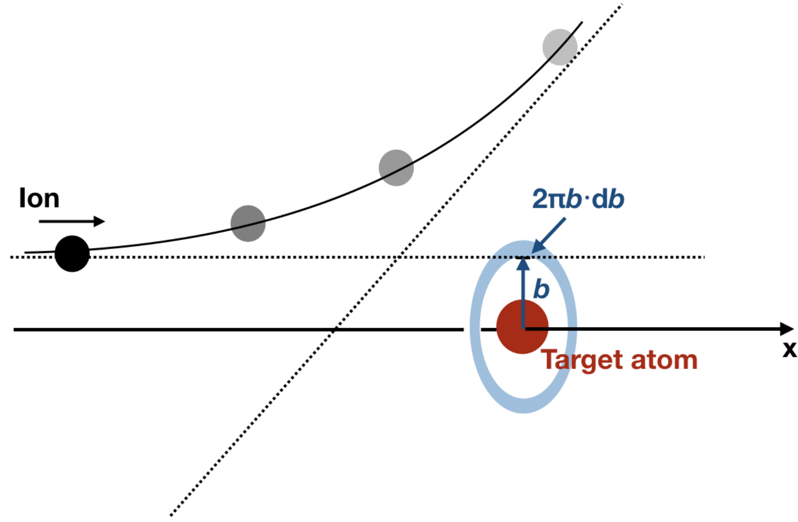

Figure 1.3: Ion trajectory after collision with a target atom. The impact parameter b is defined in the schematic trajectory.

eter b is defined as the perpendicular distance between the initial direction of the ion and the initial position of the target atom. Assuming that the initial kinetic energy of the ion is E_i and the energy transfer at an impact parameter b is T, the differential energy transfer cross section can be expressed as

$$\sigma_s(E_i, T)\ \mathrm{d}T = 2\pi b\ \mathrm{d}b. \tag{1.5}$$

The total cross section can then be calculated by:

$$\sigma(E_i) = \int_{T_{min}}^{T_{max}} \sigma_s(E_i, T)\mathrm{d}T, \tag{1.6}$$

where T_{min} and T_{max} are the minimum and maximum energy transferred, respectively. The T_{max} corresponds to a head-on collision and is found to be:

$$T_{max} = \gamma E_i = \frac{4M_1M_2}{(M_1 + M_2)^2}E_i, \tag{1.7}$$

where M_1 and M_2 are the atomic mass of the incident ion and the target atom, respectively. Next, the average energy transferred can be computed:

$$T_{avg} = \frac{\int_{T_{min}}^{T_{max}} T\sigma_s(E_i, T)\ \mathrm{d}T}{\int_{T_{min}}^{T_{max}} \sigma_s(E_i, T)\ \mathrm{d}T}. \tag{1.8}$$

For the calculation of average energy transfer from ions that can lead to displacement damage, T_{min} is equal to the threshold displacement energy T_d, which is defined as the minimum kinetic energy required by the target atom to be permanently displaced to a different lattice site.

Taking the Rutherford scattering as an example, based on the pure Coulomb potential shown in Equation (1.4), the total scattering cross section is [35]

$$\sigma_s(E_i, T) = \frac{\pi b_0^2 \gamma E_i}{4T^2}, \tag{1.9}$$

where b_0 is defined as

$$b_0 = \frac{Z_1 Z_2 q_e^2}{4\pi\epsilon_0 E_i} \frac{M_1 + M_2}{M_2}. \tag{1.10}$$

From Equation (1.8), the average energy transferred is as follows:

$$T_{avg} = \frac{\int_{T_{min}}^{T_{max}} T\sigma_s(E_i, T)\ \mathrm{d}T}{\int_{T_{min}}^{T_{max}} \sigma_s(E_i, T)\ \mathrm{d}T} = \frac{T_{min}\ln(T_{max}/T_{min})}{1 - T_{min}/T_{max}}. \tag{1.11}$$

Assuming that E_{min} is equal to E_d and T_{max} is much larger than the threshold displacement energy E_d, the expression can be simplified to

$$T_{avg} \approx E_d \ln\left(\frac{\gamma E_i}{E_d}\right). \tag{1.12}$$

Since a pure Coulomb potential is used, these results are only valid for near head-on collisions, which means that the atomic displacement can only be produced when the incident ion is close to the target atom. This is valid for light ions with a kinetic

energy that is larger than ~1 MeV [35]. For heavy ions, other potentials such as the inverse square potential need to be used. When a more complex potential is used, such analytical expressions cannot be derived easily. In addition, cascade collisions could take place after the initial ion collision, and the threshold displacement energy varies with the direction of the incident ion [39]. Therefore, computational simulations are used in this work to calculate the energy transfer for different ion impact positions. Nevertheless, the derivations presented here illustrates the relationship between the interatomic potential and the energy transfer during the ion collision process.

1.3.2 Ion energy loss through matter

When an ion slows down in a material, it interacts with the medium by two primary mechanisms: inelastic collisions with electrons in the medium (electronic energy loss) and elastic collisions with nuclei (nuclear energy loss):

$$\left(-\frac{dE}{dx}\right)_{total} = \left(-\frac{dE}{dx}\right)_{electronic} + \left(-\frac{dE}{dx}\right)_{nuclear}, \tag{1.13}$$

where $\left(-\frac{dE}{dx}\right)_{electronic}$ and $\left(-\frac{dE}{dx}\right)_{nuclear}$ represent the electronic and nuclear stopping power, respectively. The energy loss by radiation is usually negligible.

When the ion energy is high and the impact parameter is small relative to the screening radius r_{sc} defined in Equation (1.3), pure Coulomb potential can be used to describe the nuclear energy loss. When the ion energy is low and the impact parameter is of the same order of magnitude as the screening radius, screened Coulomb potential needs to be used because the screening effect from the shell electrons cannot be ignored. Different descriptions of the screening effect have been developed from the 1930s to the 1950s, including the Bohr potential [40], Thomas-Fermi potential [41], Lenz-Jenzen potential [42], and Molière potential [43]. Besides these, the Ziegler-Biersack-Littmark (ZBL) universal screening potential has also been developed from

first-principles calculations with free-electron approximation [44, 45]. The potential energy can be expressed as [45]

$$E_{ZBL} = \frac{1}{4\pi\epsilon_0}\frac{Z_1 Z_2 q_e^2}{r}\Phi(r/r_a), \tag{1.14}$$

$$r_a = \frac{0.46850}{Z_1^{0.23} + Z_2^{0.23}}, \tag{1.15}$$

$$\Phi(x) = 0.1818e^{-3.1998x} + 0.5099^{-0.9423x} + 0.2802^{-0.4029x} + 0.0282e^{-0.2016x}. \tag{1.16}$$

The ZBL potential is widely used for the study of high-energy ion collisions [1].

Regarding the damage induced by nuclear energy loss, more massive ions lead to a higher extent of structural damage due to their greater energy transfer to the target atoms. The probability of defect formation also depends on the atom threshold displacement energy. For example, according to atomistic simulations, the threshold displacement energies for Mo and S atoms in monolayer MoS_2 are ~20 eV and 6.9 eV, respectively, indicating that S vacancies are more likely to be formed [46].

For the electronic energy loss, since the movement of electrons needs to be considered, quantum-mechanical calculations need to be used to accurately determine the ion-electron interactions. Electronic stopping power can be calculated with first-principles simulations using time-dependent density functional theory (DFT) [47, 48]. If the ion velocity is higher than the velocity of the bound electrons, the Bethe–Bloch formula provides a good approximation, which has the form [49]:

$$\left(-\frac{dE}{dx}\right)_{electronic} = \frac{4\pi n Z_1^2}{m_e c^2 \beta^2}\left(\frac{q_e^2}{4\pi\epsilon_0}\right)^2\left[\ln\left(\frac{2m_e c^2\beta^2}{I(1-\beta^2)}\right) - \beta^2\right], \tag{1.17}$$

where n is the electron density of the target material, m_e is the electron rest mass, c is the speed of light, β is the ratio of the ion velocity to the speed of light, and I is the mean excitation potential. If the ion energy is low and there are electrons bounded with the ion, the ion effective charge becomes lower and corrections need to be made.

Electronic energy loss leads to ionization and excitation. For semiconductors and metals, individual ionization or excitation usually does not produce a physical defect. Secondary low-energy electrons from ion-induced ionization have a negligibly low probability to knock out a nucleus within the commonly studied range of ion energy and ion fluence [46]. However, the total electronic energy deposition from the ion stopping can produce heating within a localized volume along the ion track over a short time scale and lead to structural disorder according to the thermal spike model [50]. It has been shown by MD simulations that swift heavy ions can produce defects in suspended and supported graphene with an energy loss threshold of 8.0 keV/nm and 6.5 keV/nm, respectively [51]. For light ions such as protons and helium ions in the keV and MeV range, defects induced by electronic energy loss from the heating effect could be ignored due to the lower electronic stopping power.

1.4 Ion damage and modification of two-dimensional materials

Ion irradiation of 2D materials has been investigated by previous studies [52]. Different effects have been observed for various ion species at a range of fluence levels. A brief summary is provided here based on the observed effects. First, structural defects can be produced by ion irradiation. For light ions such as protons and helium ions, noticeable damage usually occurs at a fluence on the order of $\sim 10^{16}$ ions/cm^2 [30, 53]. Structural damage of suspended and supported graphene induced by 2-MeV protons was studied by Raman spectroscopy at different fluences [30]. It was shown that graphene is more susceptible to damage when there are fewer layers and when it is not supported by a substrate. The dependence of MoS_2 and WSe_2 defect generation on the helium fluence was also investigated via Raman spectroscopy and scanning transmission electron microscopy [53, 54]. With the increase of helium ion fluence, a semiconductor-metal-insulator transition was observed and explained by the preferential sputtering of chalcogen atoms and the dominance of metallic bonds

at intermediate helium fluence [53, 54]. Besides material-level damage, degradation of MoS_2 and graphene FETs has been probed by MeV-level protons [32, 55]. Decrease of conductivity and shift of threshold voltage were observed due to the generation of interface states and oxide charges. A more comprehensive explanation of the damage mechanisms of FET devices is included in Chapter IV. In contrast to light ions, heavy ions usually lead to detrimental effects to 2D materials and devices. It was reported that large morphological changes were created by swift heavy ions with a kinetic energy of $\sim$100 MeV at oblique incident angles [56, 57]. Layer folding, surface tracks, and surface protrusions were observed [56, 57]. For 2D FET devices, the degradation induced by heavy ions was shown to occur at a much lower fluence level compared to proton irradiation [58]. This is because heavy ions can cause higher displacement damage due to their higher atomic mass and higher energy transferred per collision.

Besides damage effects, ion irradiation can also be used to pattern 2D materials, introduce desired dopants, and tune material properties. Focused ion beams can be used for patterning and etching of 2D materials [53, 54, 59–61]. For example, thin nanoribbons with various widths can be fabricated by use of a helium ion microscope with sub-nanometer precision [54]. Focused ion beam with Ga^+ ions can be used to etch a MoS_2 thin film layer by layer [62]. Lateral homo-junction in fewer layer WSe_2 was also demonstrated by irradiating only half of the channel area with a focused helium beam [53]. There is also interest in using ions to produce graphene nanopores for DNA sequencing and water purification [63–65]. For the purpose of intentional doping, ion irradiation can either be used to create vacancies as favorable dopant sites or directly be used as doping species. For direct ion implantation, the ion energy needs to be low so that structural damage can be minimized. Doping with ion irradiation in a controlled manner was demonstrated in multiple experiments with nitrogen, boron, and heavy metals [66–68]. MD simulations have also been used to study the possible routes of controlled defect production and ion implantation [69–71].

It is noted that radiation-induced single event effects (SEEs) is an important area for the evaluation of radiation hardness of digital electronics. However, this area has not been studied in prior work mostly due to the fact that the development of 2D-based electronics is still in the basic research stage. SEEs refer to detrimental phenomena (latchup, upset, burnout, *etc.*) induced by one charged particle. For example, due to the large number of charge carriers produced by an incident charged particle, the digital state at a sensitive node can be flipped, or the induced current can surpass the damage threshold. These effects can affect or lead to catastrophic failure of electronics operation. SEE has been extensively studied for silicon complementary metal-oxide-semiconductor (CMOS) technology [72, 73], so for the use of 2D electronics in space, the assessment of SEE is also necessary in the future.

1.5 Organization of the dissertation

Chapter I describes the motivation for this research and provides a general introduction to ion irradiation effects on 2D materials. In Chapter II, proton irradiation damage on graphene is investigated using MD simulations. Defect generation probabilities and defect structures are discussed for different proton energies and incident angles. In addition, *ab-initio* and classical MD simulations are compared to evaluate the accuracy of the widely used classical MD approach. In Chapter III, X-ray photoelectron spectroscopy (XPS) was used to determine the change of chemical and electronic properties of WSe_2 fabricated from mechanical exfoliation and metal organic chemical vapor deposition (MOCVD) growth after proton and heavy-ion irradiation. In Chapter IV, the electrical characteristics of MoS_2 FETs were studied after proton and helium ion irradiation. Different FET components were irradiated separately to isolate the radiation effects to MoS_2. In addition, MD simulations were performed to determine the physical damage induced by proton and helium ions for a wide range of energies. Since the work in each chapter adopts a different approach and studies a

different 2D material, a more relevant comprehensive literature review is provided in the introduction section of each chapter.

Previously published results are incorporated into this dissertation. Chapter II includes portions of the paper entitled *"Proton irradiation of graphene: insights from atomistic modeling"* published in the journal *Nanoscale*. The material is reproduced from Ref. [74] with permission from the Royal Society of Chemistry. Chapter III uses portions of the paper entitled *"Effects of energetic ion irradiation on* WSe_2/SiC *heterostructures"* [75] published in the journal *Scientific Reports* with the permission of reuse from Springer Nature, and portions of the paper entitled *"Stability of the tungsten diselenide and silicon carbide heterostructure against high energy proton exposure"* [76] published in the journal *Applied Physics Letters* with the permission of reuse from AIP Publishing. The experimental section of Chapter IV includes portions of the paper entitled *"Extraordinary Radiation Hardness of Atomically Thin* MoS_2*"* [77] published in the journal *ACS Applied Materials & Interfaces*. The results are reprinted with permission from Ref. [77] (Copyright 2019 American Chemical Society). The use of previously published materials has been approved by all co-authors.

CHAPTER II

Molecular Dynamics Simulation of Proton Irradiation of Graphene

2.1 Introduction

It has been demonstrated that ion irradiation can modify the structural, electronic, mechanical, magnetic, and optical properties of 2D materials [78–80]. For example, electronic properties can be modified by creating vacancies and filling them with selected dopants [67, 81]. Transport properties of layered transition metal dichalcogenides can be tuned by irradiation with a focused ion beam [54, 82]. Ion bombardment can form graphene nanopores [64, 83, 84] for DNA translocation [65] and membrane devices for water purification [85]. Improvement of graphene mechanical properties such as Young's modulus with controlled Ar^+ irradiation has also been reported [86]. Although the effect of ion bombardment of graphene has been simulated previously over a range of energies and incident angles [69–71, 81, 87], the impact of proton irradiation has not yet been investigated. The proton, as the nucleus of the lightest element (hydrogen), has the capability to produce small and controlled defects so that the desired material structure and morphology can be realized. It would be challenging to achieve the same effect with swift heavy ions or ions with high atomic masses, which usually form large defect clusters [88, 89]. Experiments

have shown that unusual magnetic properties could be induced in graphene by proton-induced defects [90, 91], and techniques such as XPS and Raman spectroscopy have been used to characterize the electronic and structural properties of 2D materials with proton-induced defects [30, 75, 76]. To complement these experimental efforts, it is desirable to study the types of defects that are created by protons from a microscopic perspective. In addition, protons are a major component of cosmic rays, accounting for approximately 90% of the nuclei in cosmic rays. The use of 2D materials has been proposed for low-weight, low-power electronic devices in space applications, which is why it is important to understand their response to proton irradiation. Knowing the defect type and concentration is required for the estimation of the transport properties, mechanical properties, and thermal conductivity of irradiated graphene [92]. In this work, both classical and *ab-initio* MD methods were used to study the defect structures and defect generation probabilities induced by protons in graphene, as a representative 2D material.

Classical MD simulation tools, such as LAMMPS [93], have been widely used to simulate ion damage of graphene and other nanostructures. Here, in addition to LAMMPS, an *ab-initio* MD method is also used, in which the full interaction dynamics is simulated and different ion impact positions are sampled. Unlike graphene, an accurate and extensively-tested potential might not exist for novel 2D materials. In this case, a direct modelling based on first principles could be an appealing method. Although the *ab-initio* method is computationally expensive, it is demonstrated that with limited number of sample points, it can be used to determine the defect generation probability induced by low-energy ions.

With the classical MD code LAMMPS, an extensive study on proton-induced effects has been carried out for a proton energy range of 0.1–100 keV at various incident angles, which is limited by *ab-initio* MD simulations due to the computational expense required. However, the *ab-initio* MD method provides an accurate approach

to validate the classical MD simulations. Different defect configurations are classified and analyzed. Since protons originating from space radiation have a broad energy spectrum and is incident over a wide range of angles, our results at different proton energies and incident angles will be useful for calculating the aggregate damage effects induced by the aforementioned space proton flux. By establishing the relationship between the ion impact positions and defect types, more insight can be provided into the variation of defect generation probabilities as a function of proton energy and angle, which could also be useful for the understanding of the irradiation response of other 2D materials and ion species.

2.2 Methods

2.2.1 Methods for *ab-initio* MD simulations

Ab-initio MD simulations were performed with the SIESTA program, which uses a self-consistent density functional method with standard norm-conserving pseudopotentials [94]. As shown in Figure 2.1(a), the studied system consists of one layer of graphene of 98 carbon atoms in the $x - y$ plane and one hydrogen atom initially positioned 1.0 nm above the graphene layer. The ion charge was not simulated explicitly: the neutral hydrogen atom was used to study the impact of proton (the term "proton" is used interchangeably with the term "hydrogen atom" in this chapter). Periodic boundary conditions were applied in all three directions. The number of carbon atoms was chosen as a trade-off between the simulation speed and the interference of defect-defect interactions due to periodic boundary conditions. In the z direction, the distance between graphene and its image plane was set to 5.0 nm to avoid interactions between image systems. Double-ζ plus polarization basis sets were used with a cutoff energy of 120 Ry and a Monkhorst-Park k-point sampling mesh of $2 \times 2 \times 1$ point. The generalized gradient approximation with the PBE

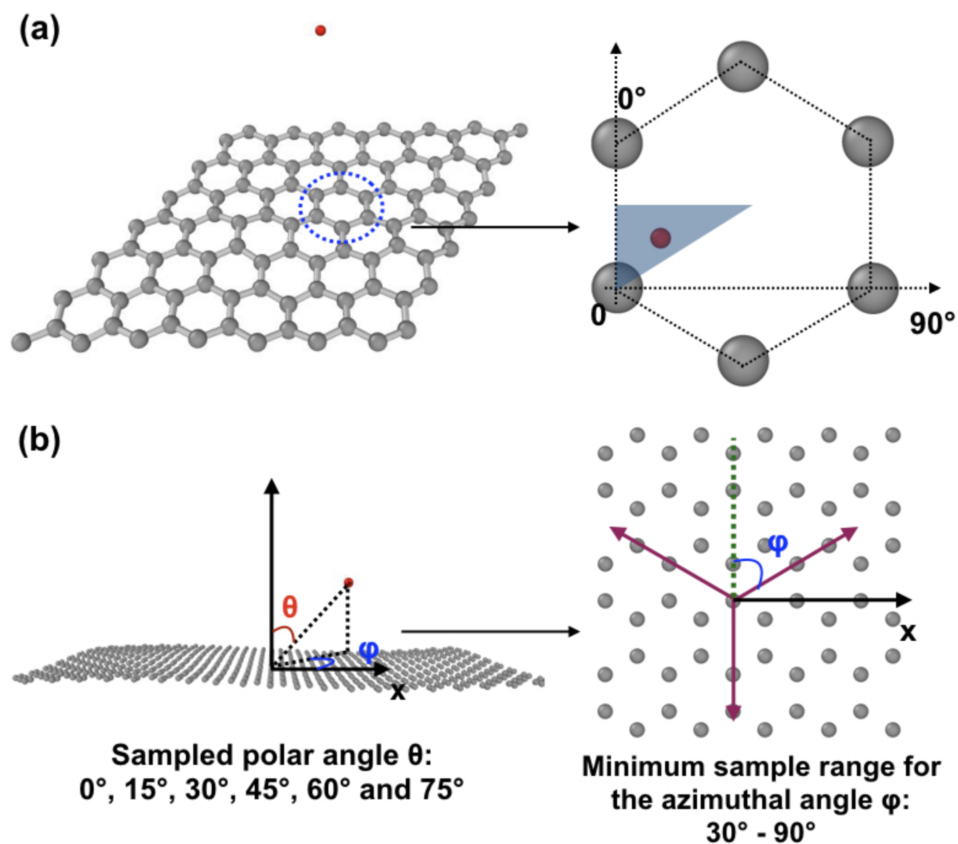

Figure 2.1: (a) The studied system in the SIESTA simulation. The position of the hydrogen atom was sampled in the blue rectangular triangle based on the structure symmetry. (b) The studied system in the LAMMPS simulation. For oblique incidence of the hydrogen atom, the polar and azimuthal angles are defined in the figure.

exchange correlation functional was used [95]. The lattice constant was optimized to be 0.247 nm according to energy minimization.

Different impact positions were sampled with four different proton energies (E_H): 0.1, 1, 10 and 100 keV. The incident direction was perpendicular to the graphene surface and each simulation only involved the incidence of one hydrogen atom without defect accumulation. Around 80 impact positions were performed for an E_H of 0.1, 1 and 10 keV, and approximately 50 simulations were performed for an E_H of 100 keV. For each simulation, the system was first relaxed at 300 K with a Nosé thermostat for 5 ps with a timestep of 1 fs. The hydrogen atom was then positioned to the top of the desired impact position. Next, the system was relaxed again for 20–120 fs, during which the movement of the hydrogen atom and the carbon primary knock-on atom (PKA) was constrained in order to maintain their relative position. The procedure described above was used to avoid repetitively running the 5-ps-long relaxation for all the different cases. The tolerance of the density matrix was fixed at 10^{-5} during the initial relaxation period. After full relaxation, the hydrogen atom was given an initial kinetic energy to initiate the collision process. During the collision and the following relaxation process, the Verlet MD method with a variable timestep was applied. A variable timestep algorithm was implemented into the SIESTA code to optimize the simulation time because extremely short timesteps are mandatory to simulate the collision process. With a higher bound of 1 fs, the actual timestep was chosen as the smallest timestep derived from the following two criteria: the displacement distance per step and the energy transfer per step. For every atom, the displacement per step was set to be less than 2.5×10^{-3}–2.5×10^{-2} nm depending on the initial velocity of the hydrogen atom. The energy loss per step was controlled to be less than 3% of the kinetic energy of the incident atom; energy transfer is inaccurate if the energy loss per step is too large. Extensive testing with various ion energies and positions was performed to make sure that the choice of the timestep

can yield self-consistent result from the energy transfer process. A smaller timestep is required for higher ion energy and smaller impact distance. For an E_H of 0.1 keV and 1 keV, a minimum timestep of 10^{-3} fs is sufficient, however, for an E_H of 100 keV, a minimum timestep of 10^{-5}–10^{-4} fs is required to properly compute the energy transferred. The tolerance of the density matrix was maintained at 10^{-5} during the C-H collision but was increased to 10^{-3}–10^{-4} during the final relaxation period. In order to avoid ejected carbon atom or hydrogen atom from re-entering the simulation box due to the periodic boundary conditions, their kinetic energies were forced to zero if their projected distance to the graphene surface along the z direction was larger than 0.8–1.0 nm, which is sufficiently large to avoid perturbation to the relaxation of the defected structure. After the ion bombardment, the system was relaxed with a timestep of 1 fs until the structure of the system was stable for 500 fs.

2.2.2 Methods for classical MD simulations

The classical MD simulations were performed with the LAMMPS code [93]. As shown in Figure 2.1(a), one layer of graphene of 756 atoms with a lattice constant of 0.253 nm was created in LAMMPS with periodic boundary conditions in the x and y directions and a fixed boundary condition in the z direction. The incident hydrogen atom was initially placed 0.3–0.5 nm distance away from the surface of graphene, which is beyond the defined cutoff distance of the ZBL potential between the hydrogen atom and carbon atoms. The universal repulsive potential from the ZBL formalism [96] was used to describe the screened nuclear repulsive force at short range. It was used here because a very small impact distance is required to create defects with the incident hydrogen atom. The ZBL cutoff distance was set to be 0.25–0.5 nm depending on the ion energy, while ensuring that further increase of the cutoff distance does not cause significant change of the energy transfer during the collision process. Here, the chemical effect between hydrogen and carbon atoms was

ignored, which is justified for high-energy ions, where the energy transfer from long-range interactions is small. For low-energy ions, for example at a hydrogen energy of 0.1 keV, this could lead to a slight underestimation of the energy transfer. However, a smooth connection between the ZBL potential and a chemical potential could also lead to errors at intermediate interatomic distance near the connection point. The effective charge of a high-energy ion depends on its velocity. For example, for a proton energy of 0.1 keV and 100 keV, the effective charge is estimated to be 0.85 and 0.20, respectively [44]. Although the ion effective charge is not taken into account in the ZBL formalism, the ZBL potential has shown good agreement with experimental data when predicting the ion stopping power [96]. The Tersoff/ZBL potential from the LAMMPS package was applied for the potential between carbon atoms. In the Tersoff/ZBL potential, the Tersoff and ZBL are smoothly connected by a Fermi-like function where short interatomic distance is dominated by the ZBL potential and long interatomic distance is dominated by the Tersoff potential. The parameters described in Ref. [97] were used to define the Tersoff/ZBL potential, which were also used in a prior work in which the ion bombardment of graphene was studied [69].

After the potentials were defined, the system energy was minimized and then the system was relaxed for 2 ps with a timestep of 0.1 fs with NVT ensemble at 300 K. After the relaxation, the position of the hydrogen atom was re-positioned based on the position of the selected carbon PKA at the center of the graphene system. The impact position of the hydrogen atom relative to the PKA was defined as its projected position in the graphene plane following the direction of its initial velocity. Although there is thermal vibration of the PKA during the time when the hydrogen atom is approaching the graphene surface, this only leads to a small change to the impact position and is minimized by placing the hydrogen atom right above the potential cutoff distance. The hydrogen atom was then given an initial velocity and the irradiation process was simulated with the NVE ensemble with an adaptive

timestep for a period of 0.5–1 ps depending on the ion energy. During the irradiation, three different timesteps were used for the following three phases to optimize the total simulation time. In the first phase, C-H interactions will take place. The hydrogen atom interacts with the PKA and then might collide with another carbon atom with a very small probability. The timestep used for the C-H collision process ranged from 10^{-2} fs to 10^{-5} fs for an ion energy range of 0.1 keV to 100 keV. A smaller timestep needs to be used for a higher ion kinetic energy to ensure that the energy transferred during the collision process is not affected by the coarse timestep. In the second phase, C-C interactions will take place. The initial PKA will have a certain probability to collide with other carbon atoms and cause cascade collisions. The timestep used for the C-C collisions ranged from 2×10^{-2} fs to 2×10^{-4} fs for an ion energy range of 0.1 keV to 100 keV. In the third phase, if there are atoms being ejected, it takes time for them to escape the simulation box and further relaxation also takes place. A timestep of 0.02 fs was used during this phase. After the ion irradiation, the system was relaxed with NVT ensemble at 300 K for 10 ps with a timestep of 0.1 fs. In order to classify different types of defects, the system energy was minimized again after the relaxation and the centro-symmetry parameter [98] was computed in LAMMPS to quantify the local environment of each atom. Based on the centro-symmetry parameter of each atom, different defect configurations were identified.

Using the described approach, the defect structures were simulated first at different proton energies ranging from 0.1 keV to 100 keV at normal incidence. Since the thermal vibration of atoms affects the collision process and the resulting defect type, for the same ion energy, the same impact position was simulated three different times with a different random number seed for the initial relaxation process. Thus, the defect map shown in Figure 2.4 was generated three times for the same ion energy although one of them is shown here. However, all the data were included when the

defect generation probabilities were calculated. Next, oblique incident angles were studied with different azimuthal and polar angles, as defined in Figure 2.1(b). To study the effect of azimuthal angle, different azimuthal angles were sampled at an E_H of 10 keV at a polar angle of 30° and 75°. The azimuthal angles were sampled at 0°, 15°, 30°, 45°, 60°, 75° and 90°. To study the effect of polar angle, the polar angles were sampled at 15°, 30°, 45°, 60° and 75° for an E_H of 0.1, 1, 10 and 100 keV. The azimuthal angle was randomly selected between 30° and 90° due to the crystal lattice symmetry, as illustrated in Figure 2.1(b). In total, approximately 200,000 simulations were performed.

2.3 Results and discussion

2.3.1 Defect structures and defect generation probabilities from *ab-initio* MD simulations

The defect types as a function of the proton impact position are shown in Figure 2.2 with the defect structures drawn in Figure 2.3. As shown in Figure 2.3(a), due to the symmetry of the graphene hexagonal lattice structure, the impact positions only need to be sampled from 0° to 60° relative to the carbon PKA. Generally, a higher fraction of the ion kinetic energy can be imparted to the PKA when the distance between the two atoms is closer. Due to the small defect cross section from the proton irradiation, a bisection method was used to first find the onset impact position for single-vacancy (SV) within which more impact positions were sampled.

From Figure 2.2(a), it is shown that at 0.1 keV, the dominant defect type is SV. At the boundary of SV and intact in Figure 2.2(a), there is one instance of Frenkel pair (FP) corresponding to the situation where the PKA does not have enough energy to escape the graphene surface and finally pulls back to another crystal site (in the image system). In this work, the term FP is used to describe all the defect structures

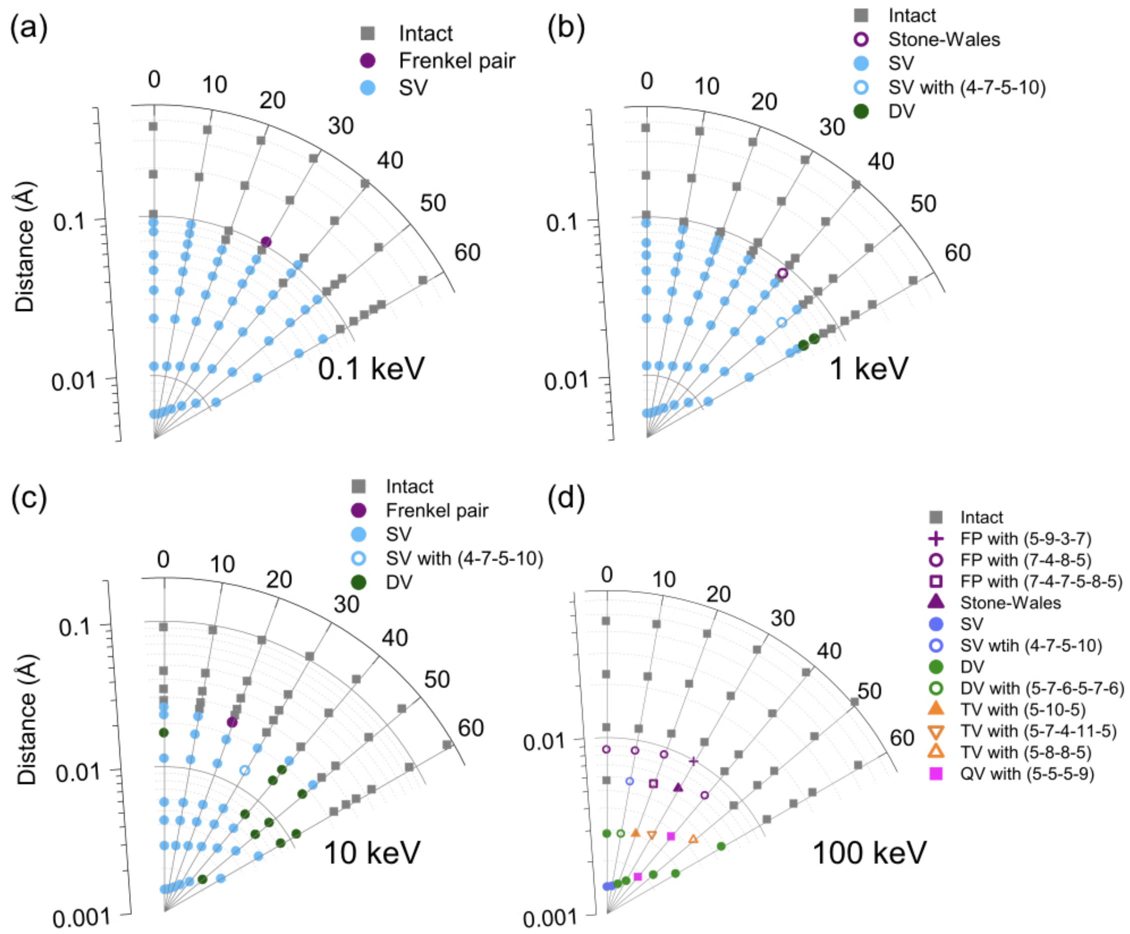

Figure 2.2: Defect types as a function of the impact position of the proton for an incident energy of (a) 0.1 keV, (b) 1 keV, (c) 10 keV, and (d) 100 keV at a vertical incident angle simulated with the *ab-initio* MD code SIESTA. The origin of the polar coordinate system is the position of the selected carbon PKA and the marker positions correspond to the impact positions of the proton. For defect configurations with no, one, two, three and four atoms being ejected out of the simulation system, they are labeled as FP (purple), SV (blue), DV (green), TV (orange), and QV (pink), respectively.

without atom being ejected. Along a direction of 40° relative to the PKA, one instance is observed of no defect at a radius smaller than those that can cause SV. Intuitively, one would expect a larger energy transfer at a closer impact position and, accordingly, a SV at this impact position. However, due to the random thermal movement of the carbon atoms, even if the initial impact position were fixed, the energy transfer to the PKA during the collision process and the ejected direction of the PKA could vary. In addition, at 0.1 keV, the maximum energy transferred to the PKA is very close to the threshold displacement energy. Therefore, it is possible that the PKA relaxes back from an impact distance smaller than those at which the PKA does not relax back. This also means that the defect map shown in Figure 2.2 is not completely deterministic. The same effect has also been seen in Figure 2.4(a) from the LAMMPS simulation.

At an E_H of 1 keV, the dominant defect type is still SV, as shown in Figure 2.2(b). However, the double-vacancy (DV) starts to form. The DVs are created when the hydrogen atom is 60° relative to the PKA because the closest neighbor of the PKA is right along the path of the PKA. The relaxed 5-8-5 structure, which is also the most common DV structure from the simulation, is shown in Figure 2.2(f).

At an E_H of 10 keV, the SV cross section becomes smaller (see Figure 2.2(c)) because the interaction time around the PKA becomes shorter. As a result, a closer distance is required for the same amount of energy transferred, which leads to a smaller SV cross section. The relative probability of DV becomes higher than that of 1 keV because the incident proton is more energetic. Besides the cluster of DVs at 60°, there are also two isolated instances of DV at 0° and 50°. The DV at 0° is formed by the PKA hitting the second carbon atom at the opposite end of the carbon ring. The DV at 50° is formed by the incident proton hitting the second carbon atom (structure shown in the right image of Figure 2.5(g)). The DVs are more frequently formed by a second collision with the carbon PKA. Such a second collision with proton is less

likely to happen due to its smaller size.

At an E_H of 100 keV, due to the higher kinetic energy of the incident ion, different defect structures with multiple vacancies can be formed (see Figure 2.2(d)). As higher ion energy leads to more complicated cascade collisions and longer relaxation time, longer computational time is required for each simulation, which limits the number of impact positions to be sampled. Defect structures up to four vacancies have been obtained. Ejecting more atoms is still possible but less likely, as shown later from the LAMMPS simulation. The total defect cross section continues decreasing with increasing proton energy. Defects can only be produced within a radius of $\sim$0.01 Å, corresponding to an extremely small defect cross section. Thus, for light ions, in order to simulate the defect generation probabilities efficiently, it is important to first exclude the areas where the energy transfer is too small to produce any defects.

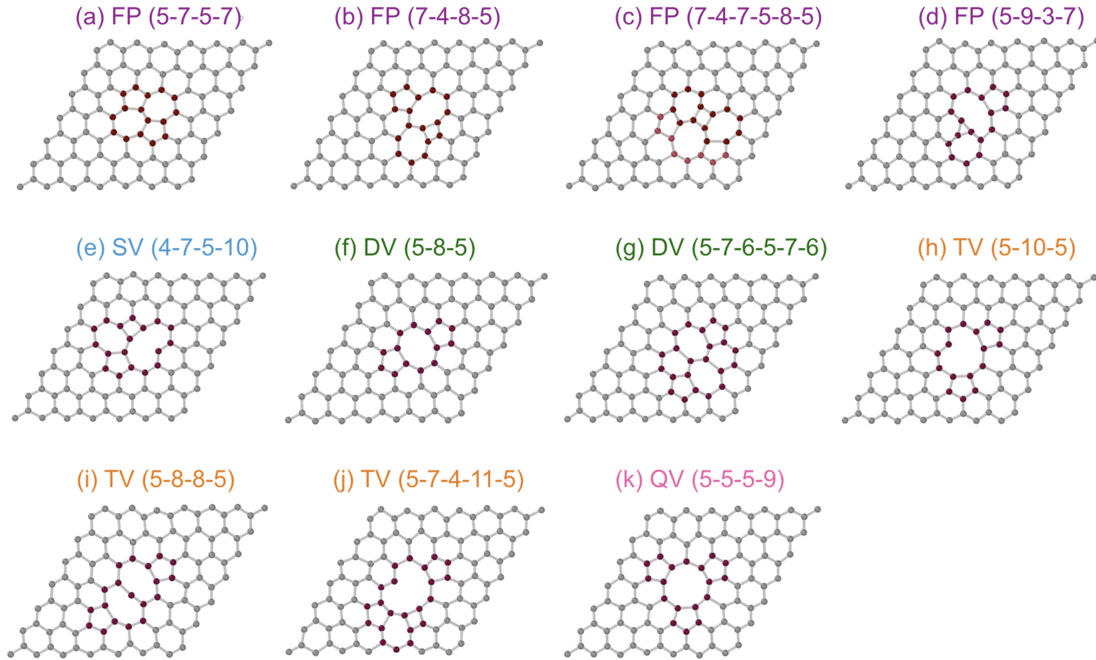

Figure 2.3: Different types of defects obtained from the SIESTA simulations for no (FP), one (SV), two (DV), three atoms (TV), and four atoms (QV) ejected from the simulation box after proton irradiation. The defect configurations labeled in Figure 2.2 are shown in this figure.

The different types of defects from the SIESTA simulations are shown in Figure 2.3. At an E_H of 1 keV, a Stone-Wales (SW) defect (see Figure 2.3(a)) is produced after the PKA forms a dangling bond beneath the graphene surface for ∼1 ps. The SW defect has been observed experimentally after electron irradiation [99, 100]. According to the DFT calculation, it has a formation energy of ∼4.8 eV and a high formation/removal energy barrier of ∼9.2 eV due to the large atom arrangement needed [101]. The 7-4-8-5 structure shown in Figure 2.3(b) is formed by a lateral movement of the PKA atom located at the intersection of the 7-4-8 rings. The same structure has also been identified by atomistic simulation as a radiation-induced defect with a formation energy of 11.3 eV [102]. The 7-4-7-5-8-5 defect (see Figure 2.3(c)) is created by 100-keV proton after a more violent local disorder, which has also been reported by atomistic simulation of graphene nanoribbon after annealing at high temperature [103]. The structure in Figure 2.3(d) can be considered as a carbon atom placed in the bond center of two adjacent atoms (the "bridge" site), which corresponds to an energetically favorable site for adatom [92]. The three carbon atoms that are bonded with each other are positioned below the graphene plane in order to accommodate to this topological structure. With one missing carbon atom, the 4-7-5-10 defect (see Figure 2.3(e)) can be formed instead of a commonly seen 5-9 structure. According to Ref. [104], it can be transformed to the 5-9 structure by bond rotation with an energy barrier of ∼1.2 eV. For DV structures, as shown in Figure 2.3(g), a 5-7-6-5-7-6 structure (not the SW defect) can be formed by rotation of two C-C bonds after two adjacent carbon atoms are removed. Compared with other DV structures such as 5-8-5 or 555-777, this structure is found to be energetically unstable [105]. For the triple-vacancy (TV), the 5-10-5 structure (see Figure 2.3(h)) has the lowest energy among all TV defects with a formation energy of 10.63 eV according to the tight-binding calculation [106]. In comparison, the 5-8-8-5 defect and 5-7-4-11-5 defect (see Figure 2.3(i) and (j)) are less energetically favorable by having higher for-

mation energies [106]. Regarding the quad-vacancy (QV), the 5-5-5-9 structure has been observed twice, corresponding to the most stable QV structure with a formation energy of 11.84 eV [106]. It can be noted that, besides the defect structures shown in Figure 2.3, other types of topological defects can also be formed, as later shown from the LAMMPS simulations. Due to the high energy injection from the protons, a rich variety of defects can be produced including both low-energy defects and those that are energetically unfavorable.

2.3.2 Defect structures and defect generation probabilities from classical MD simulations

The defect types as a function of the proton impact position at normal incidence from the LAMMPS simulation are presented in Figure 2.4. For FP, SV and DV, a finer classification of the defect structures was performed, as explained in Figure 2.5. For FP (see Figure 2.5(a)–(c)), type 1 corresponds to a carbon atom near the top or bottom position of another carbon atom (the "top" site). FP type 2 corresponds to a vacancy along with an adatom between two adjacent carbon atoms (the "bridge" site). The FP type 3 includes all the other FP structures, which are less likely to occur. According to the *ab-initio* calculation [101], the "bridge" site has the lowest formation energy (6.3 eV) whereas an exact "top" site has a formation energy of 7.2 eV. It was also reported in Ref. [101] that, compared with the exact "top" site, it is more stable to have an adatom slightly shifted from the top, which gives a formation energy of 6.8 eV. Among all the proton-induced defects, the SW defect does not have a high probability to occur, which is consistent with prior MD results [107].

For SV (see Figure 2.5(d)–(f)), type 1 is a simple SV with 5-9 structure. SV type 2 is actually a DV with one adatom at the top/bottom/bridge location. The SV type 3 includes all the other SV configurations. For DV (see Figure 2.5(g)–(i)), type 1 is defined as the DV configurations where the distance between two missing atoms

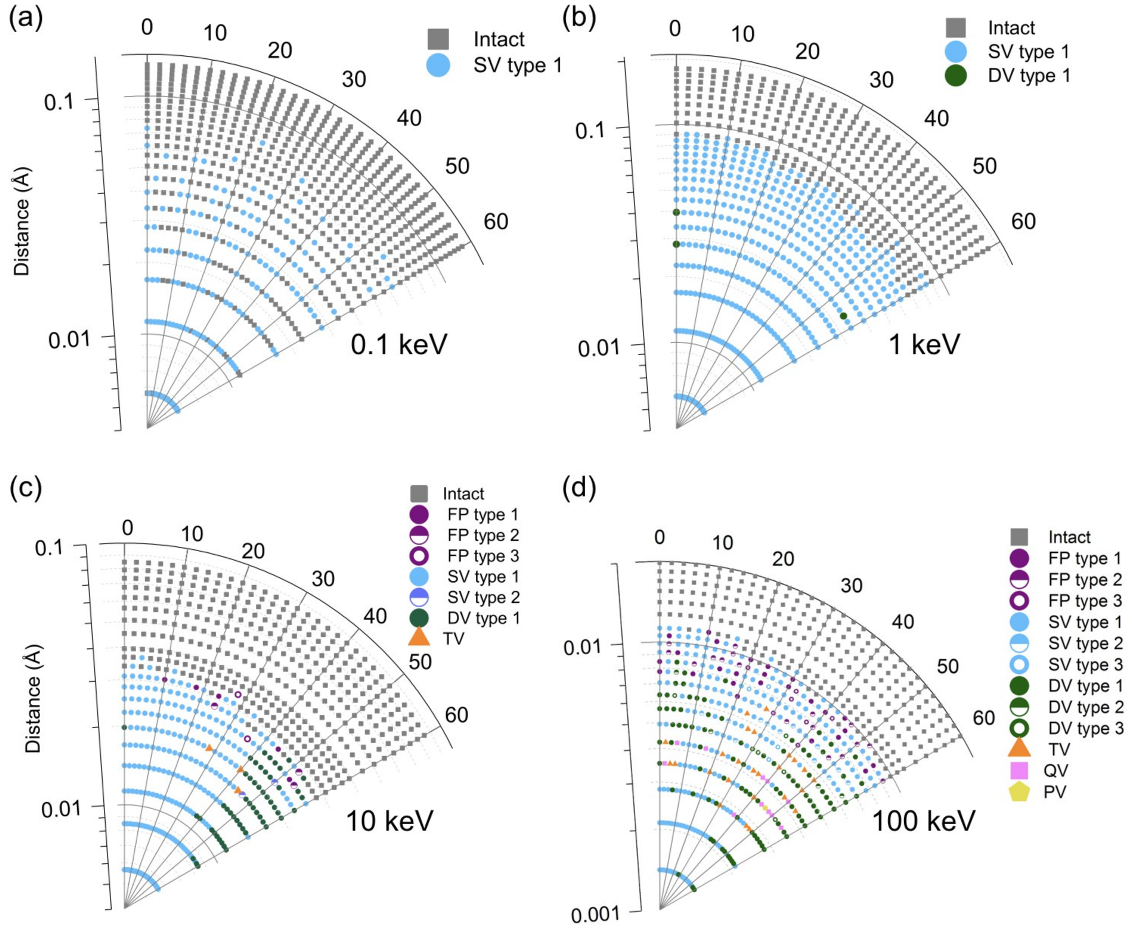

Figure 2.4: Defect types as a function of the impact position of the proton for an incident energy of (a) 0.1 keV, (b) 1 keV, (c) 10 keV, and (d) 100 keV at normal incidence simulated with the LAMMPS code. The origin of the polar coordinate system is the position of the selected carbon PKA and the marker positions correspond to the proton impact positions. For defect configurations with no, one, two, three, four, and five atoms being ejected out of the simulation system, they are labeled as FP (purple), SV (blue), DV (green), TV (orange), QV (pink), and PV (yellow), respectively.

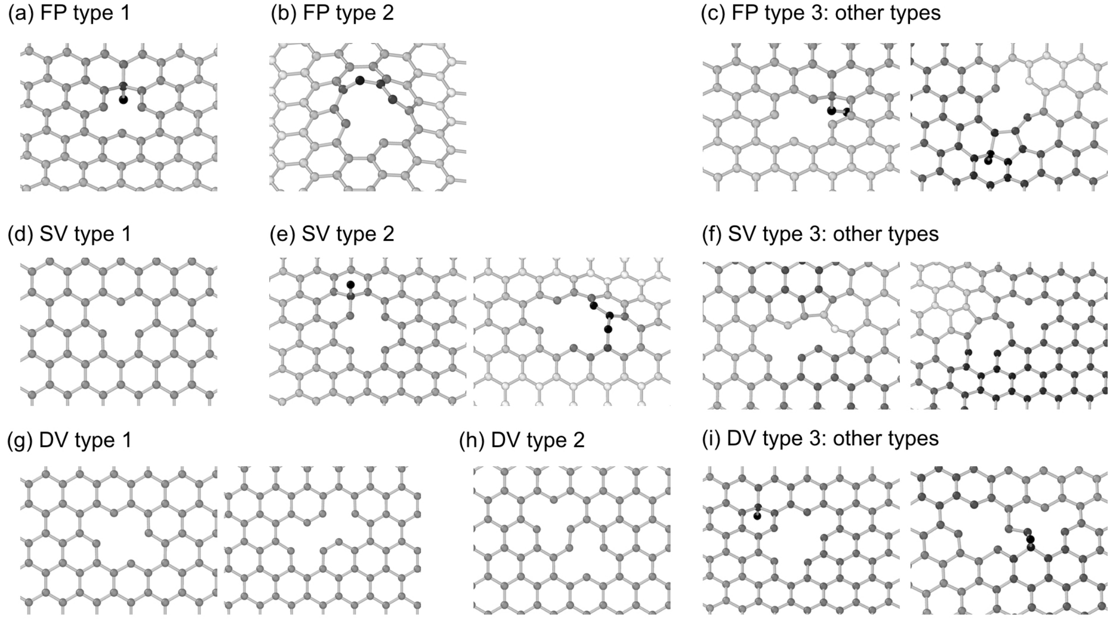

Figure 2.5: Different types of defects defined in Figure 2.4 for no (FP), one (SV), and two atoms (DV) ejected from the simulation box after proton irradiation. The defect types obtained from the LAMMPS code were classified based on the positions of the vacancies and interstitials.

is equal to or smaller than $2a_0$, where a_0 is the distance between two neighboring atoms. There are only three configurations satisfying this condition, corresponding to two missing atoms within the same carbon ring. They are grouped together because these defects can be easily formed due to the short distance between the two missing atoms. Type 2 is defined as configurations where the distance between two missing atoms is larger than $2a_0$. Type 2 defects are usually formed by the relaxation of a large local disorder, creating two single vacancies far away from each other. The DV type 3 includes all the other DV structures, for example, a defect with TV and one adatom. The structures in the type 3 of FP, SV, and DV are usually complicated. Some of them involve the rotation of bonds and some of them form complex structures by breaking the planar crystal structure. In general, the number of possible structures increases with the number of missing atoms since more defect combinations occur with more vacancies. Therefore, for structures with more than two missing atoms, a

finer defect classification was not attempted.

At an E_H of 0.1 keV (see Figure 2.4(a)), only SV can be formed because the proton energy is low. Instead of a sharp boundary between the SV and no defect, the SV probability decreases gradually with increasing impact position (or radius). As explained earlier for the SIESTA simulation, this is because the energy transferred to PKA is very close to the threshold displacement energy so that the PKA energy and direction will also be influenced by the random thermal motion of the carbon atoms. At 1 keV (see Figure 2.4(b)), the dominant defect type is still SV with a low probability of DV. Interestingly, no FP is formed at both 0.1 keV and 1 keV. At an E_H energy of 10 keV (see Figure 2.4(c)), all three types of FP and SV are observed. In addition, DV type 1 and TV can also be formed. Although SV type 3 is not shown in Figure 2.4(c), it is observed in the complete data set since Figure 2.4(c) only includes one third of the data as described in the Methods section. At 100 keV (see Figure 2.4(d)), all three types of FP, SV and DV as well as TV, QV and penta-vacancy (PV) can be formed. The fact that FPs can only be formed at 10 and 100 keV shows that if a carbon atom does not have sufficient energy to escape the graphene surface and its maximum distance to its original site is not far, it has a very high probability to relax back. The fact that DV type 2 and 3 can only be formed at 100 keV indicates that the complicated collision cascade induced by large energy injection is required to form complicated DV structures. This can also be confirmed by examining the individual collision dynamics of the type 2 and 3 of DV defects. The proton-induced defects for 0.2, 0.5, 2, 5, 20 and 50-keV protons were also simulated and similar defect maps can be found in Figure 2.6. The defect generation probabilities as a function of the proton energy is shown in Figure 2.7. Since the simulated positions are not uniformly distributed over the graphene area, the Monte Carlo method was used to uniformly sample 10^7 positions within the area of interest where defects can be produced. The defect type of the closest simulated impact position was assigned to

the sampled positions from the Monte Carlo method. Within the area of interest, the defect generation probability was calculated by dividing the number of points corresponding to a certain type of defect by the total number of sample points. The actual defect probability was then scaled to the entire graphene area. The number of simulated points for each proton energy is shown in Figure 2.6. For a defect generation probability below $\sim 5 \times 10^{-5}$, a large statistical fluctuation is expected due to the limited sample points.

If one considers each defect type as a function of the proton energy, the SV probability first increases and then decreases with the proton energy. The initial increase is due to the fact that more energy can be transferred to the PKA to allow it to escape from the graphene surface, and the further decrease is due to the fact that shorter interaction time leads to closer impact position for the same amount of energy transferred. In other words, at the same impact position, the fraction of energy transferred from the proton decreases with the increase of the proton energy, which leads to the decrease of the defect probability at energies above 0.2 keV. These two competing factors determine the overall trend of the SV probability. It is noted that a proton energy of 100 eV is very close to the threshold proton energy that can lead to defects in graphene. Based on the displacement threshold energy of graphene using the Tersoff potential, the threshold proton energy is calculated to be ∼80 eV. The trend for TV can be explained with the same two competing factors. However, for the DV probability, there is an abrupt change at 5 keV and then a smooth decrease with the increase of proton energy. The reason for the abrupt change is that the formation of DV is dominated by a second collision with the proton if the proton energy is below 5 keV, however, if the proton energy is above 5 keV, a second collision with the PKA becomes dominant. In other words, the abrupt change is due to the change of the direction of the proton and PKA after the collision. For vacancies above TV, the statistics is not enough to draw conclusions. Based on Figure 2.7, the probability

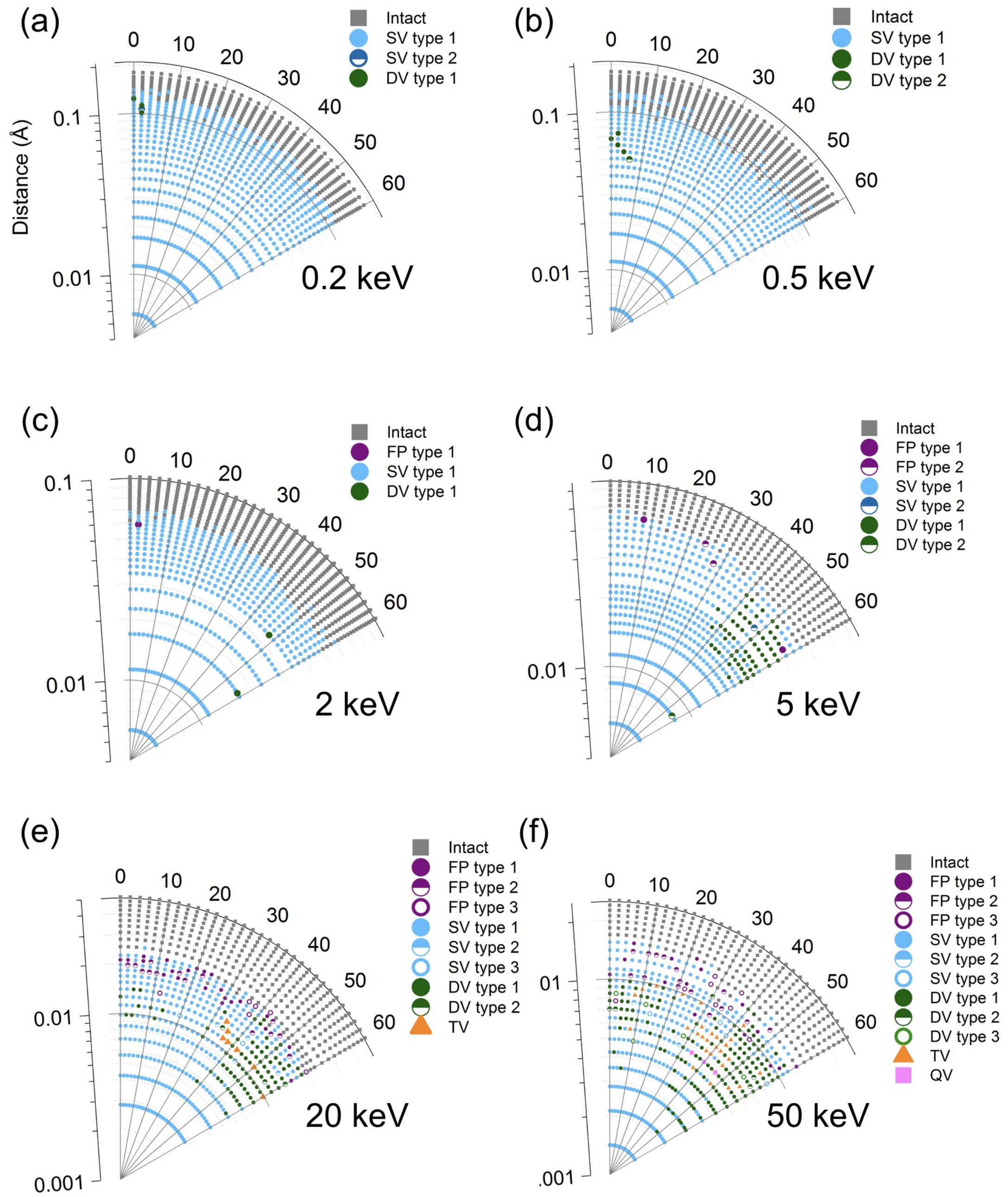

Figure 2.6: Defect types as a function of the impact position of the proton for an incident energy of (a) 0.2 keV, (b) 0.5 keV, (c) 2 keV, (d) 5 keV, (e) 20 keV, and (f) 50 keV at normal incidence simulated with the LAMMPS code. For defect configurations with no, one, two, three and four atoms being ejected out of the simulation system, they are labeled as FP (purple), SV (blue), DV (green), TV (orange), and QV (pink), respectively.

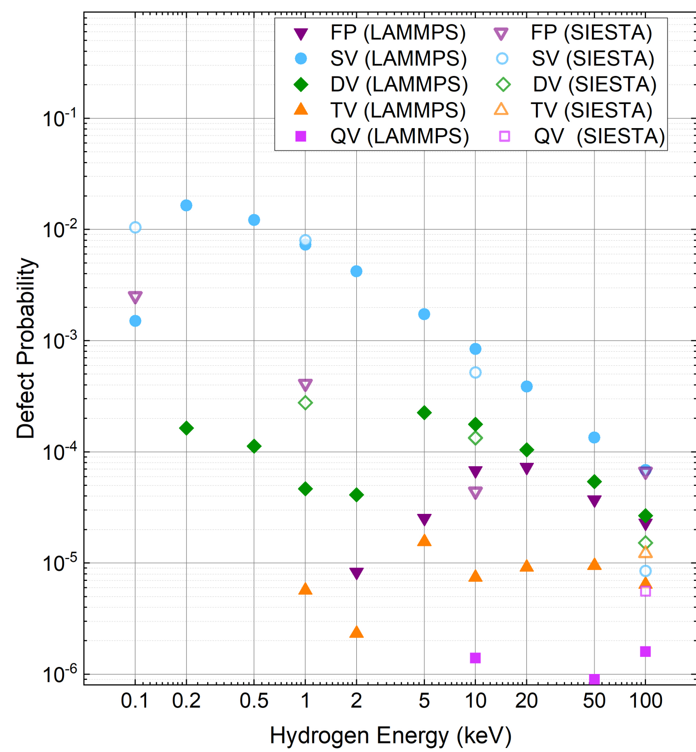

Figure 2.7: The generation probabilities of different types of defects calculated from the SIESTA and LAMMPS simulations.

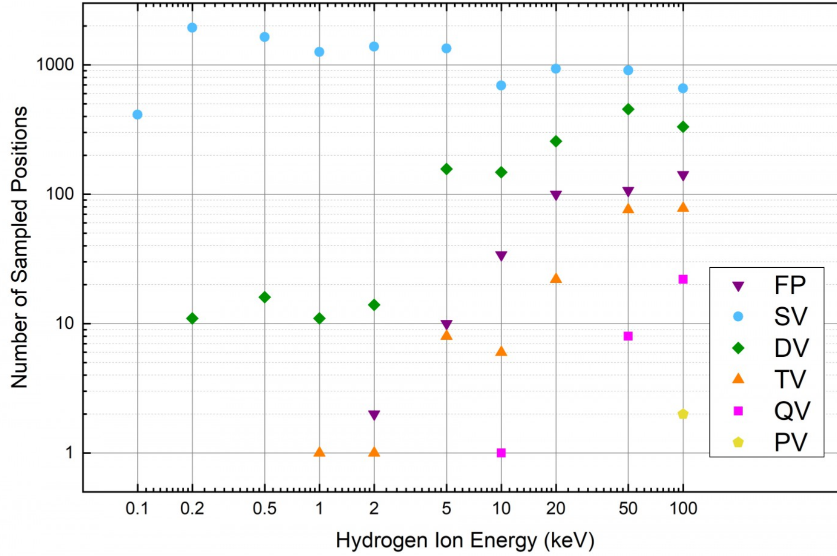

Figure 2.8: The number of sampled ion positions for different proton energies at a normal incidence angle simulated with the LAMMPS code. The defect generation probabilities presented in Figure 2.4 were determined based on the number of sampled positions shown here.

of QV does not vary significantly, although the total defect generation probability decreases with the proton energy.

Although the Tersoff potential was used here to describe the C-C interactions, AIREBO potential [108] has also shown to be an accurate potential to simulate thermal, mechanical and chemical properties of carbon systems [109, 110]. However, it was not used here due to the concern of underestimation of short-range interactions. An interesting direction for future work would be to smoothly connect AIREBO with the ZBL potential and compare the difference with the Tersoff/ZBL potential.

2.3.3 Comparison of results from *ab-initio* and classical MD simulations

By comparing Figure 2.2 and Figure 2.4 obtained from the *ab-initio* and classical MD simulations, respectively, a similarity of the defect types and their impact positions at each proton energy can be observed. For example, at 10 keV, the DVs are generated at very similar impact positions and this is because these impact positions

allow a high probability of a second collision with a neighboring carbon atom.

As shown in Figure 2.7, at 0.1 keV, the SV probability differs by a factor of 6.9. This difference can also be reflected by the difference of the SV boundary between Figure 2.2(a) and Figure 2.4(a). With the SIESTA code, among all the simulations, the minimum PKA energy to cause SV is found to be 22.4 eV, which is consistent with the published threshold displacement energies from DFT calculations of 22–23 eV [111, 112]. With the LAMMPS code, the minimum PKA energy to cause SV is ∼22.5 eV, which is close to that found from the SIESTA code and is also consistent with the reported threshold displacement energy calculated from the Tersoff/ZBL potential [113]. However, depending on the ejected direction of the PKA, the minimum energy to form a SV can vary [112]. It can be noticed that if the PKA gains a kinetic energy of 23–25 eV, it has a high probability to form an SV with the SIESTA code, but a much lower probability with the LAMMPS simulations. Although the global minimum PKA energy to form an SV is about the same between the two approaches, it differs by 1–2 eV depending on the ejected angle. Therefore, the discrepancy could be related to the accuracy of the potential used. Since the proton energy is 100 eV, the maximum energy that can be transferred to a PKA is only around 30 eV. Therefore, the SV probability is very sensitive to the energy required to form a SV at different ejection angles. When the proton energy is 1 keV, the SV generation probabilities from the two approaches become closer to each other. The difference in the displacement energy has less effect on the SV probability because the energy transferred becomes one order of magnitude larger and several electronvolts of difference in energy only corresponds to small differences in the impact position. For the DV, since its probability is extremely low (see Figure 2.2(b) and 2.4(b)), the accuracy of the DV probability is limited by the number of sample points. A finer mesh will be needed to improve the DV statistics, but might not be necessary depending on the required precision of the application. At 10 keV, a relatively good agreement is

observed for FP, SV and DV between the two approaches. The discrepancy is due to the combination of limited sample points in the *ab-initio* method and the inaccuracy of the interatomic potential defined in the simulations. However, for an application that only requires the order of magnitude of the defect generation probabilities, both methods can be considered as valid at this proton range. At 100 keV, only qualitative comparison is possible due to the limited statistics from the SIESTA code. Since complicated collision cascade and relaxation can take place, LAMMPS is a more practical approach to estimate the defect generation probabilities at this high proton energy. It is noted that the electronic energy loss is not taken into account in both the *ab-initio* and classical MD simulations. In order to determine the electronic stopping power, time-dependent DFT calculations need to be performed. However, for the proton energy range studied in this work, the electronic stopping power is small compared to the critical stopping power that can lead to structural damage induced by local heating [51].

2.3.4 Proton irradiation at oblique angles

The oblique ion incidence angles were studied with classical MD simulations. The azimuthal angle was first sampled between 0° and 90° with a proton energy of 10 keV at two polar angles: 30° and 75°. It can be observed from Figure 2.9 that the dependence of SV probability on the azimuthal angle is small. The variation of other types of defects is small at a polar angle of 30°, but can be large for some types of defects at a large polar angle (75°). Under most of the conditions, the difference in the defect generation probability is within a factor of 2–3. This is expected because the azimuthal angle of the incident ion only affects the azimuthal direction of the ejected PKA but hardly affects its polar angle. Due to the discrete positions of the graphene atoms, some extent of variation exists. For example, as shown in Figure 2.9(b), at a proton energy of 10 keV and at a polar angle of 75°, the TV generation probability

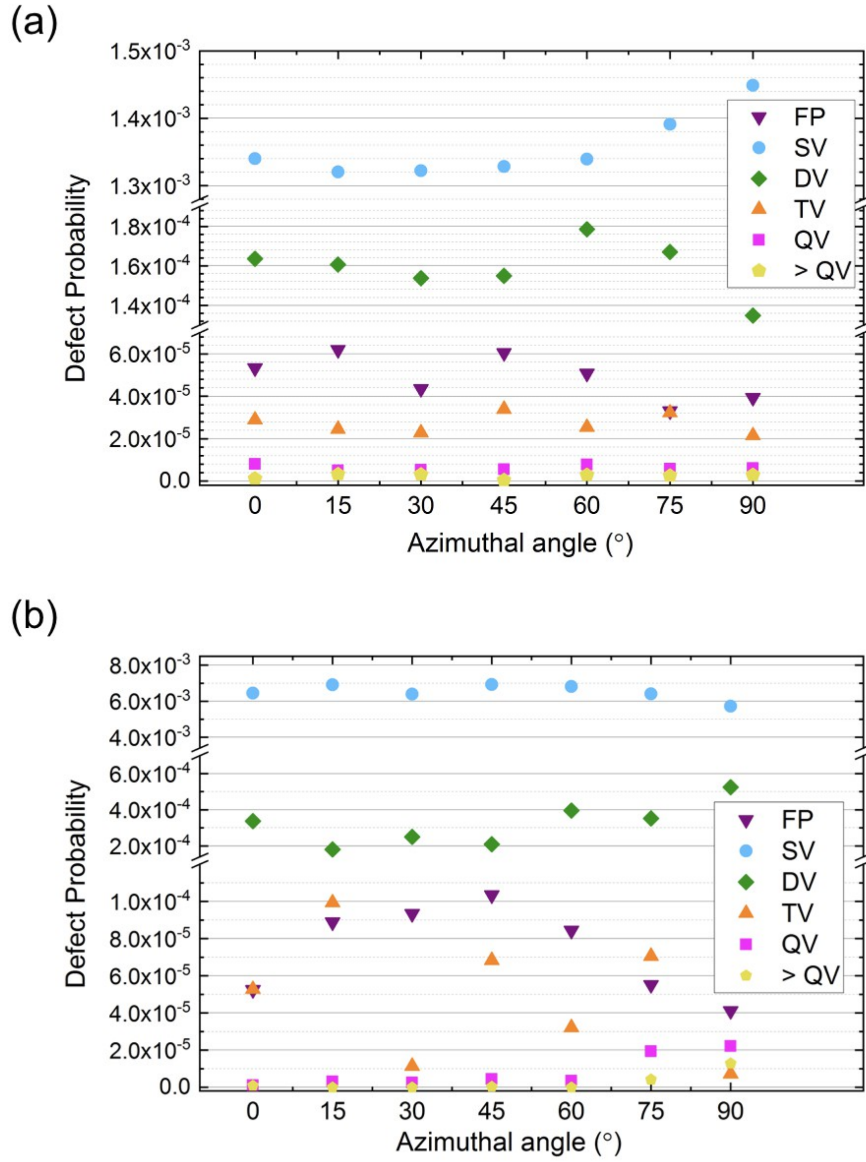

Figure 2.9: The generation probabilities of different types of defects as a function of the azimuthal angle of the incident proton at an energy of 10 keV for a polar angle of (a) 30° and (b) 75°.

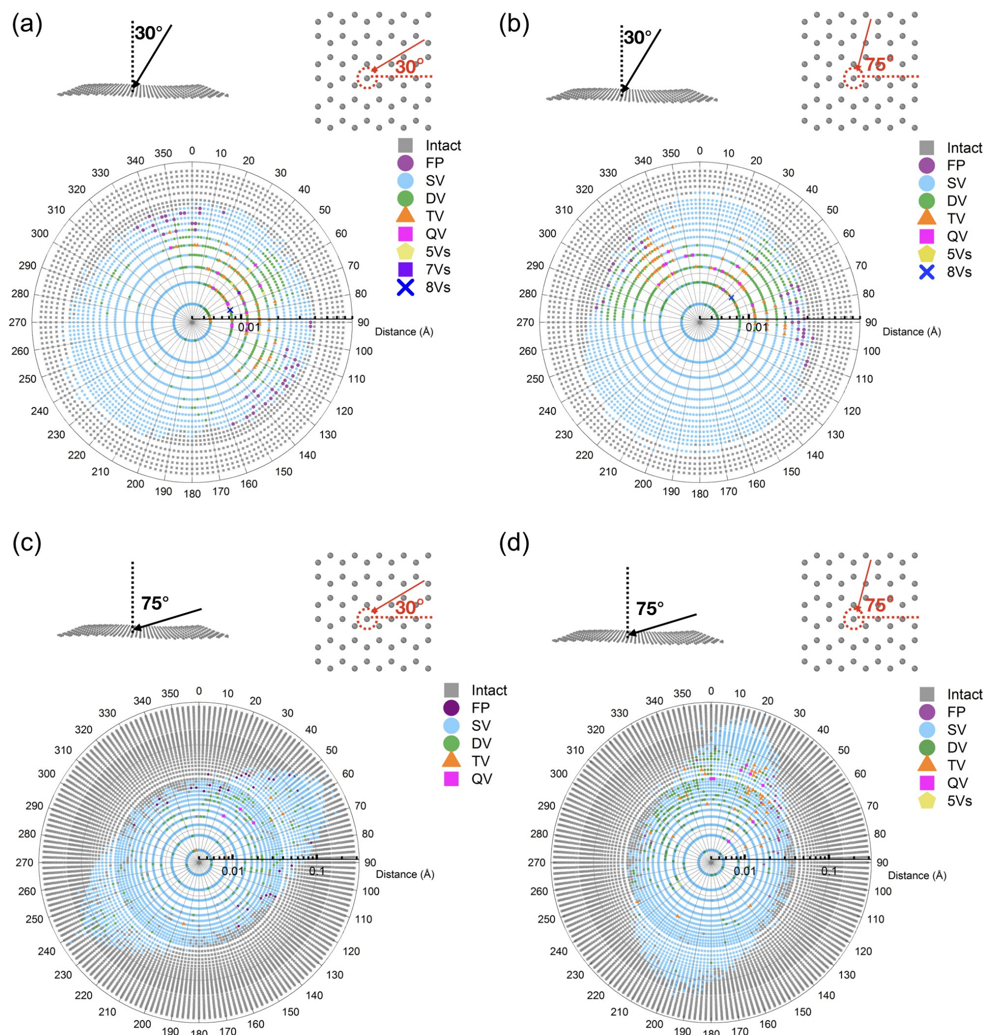

Figure 2.10: Defect types as a function of the impact position of the proton for an incident energy of 10 keV at different azimuthal incident angles. The study was performed at a polar angle of 30° and 75°. At a polar angle of 30°, the results for an azimuthal angle of (a) 30° and (b) 75° are shown here. At a polar angle of 75°, the results for an azimuthal angle of (c) 30° and (d) 75° are shown here. The relationships between the incident angle, impact position and graphene structure lead to the differences shown in this figure.

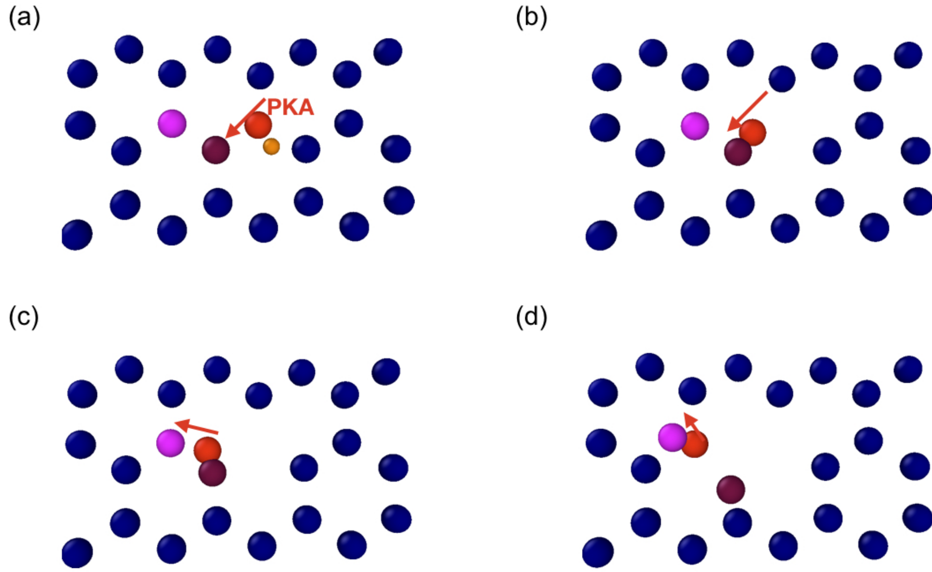

Figure 2.11: Example of TV formation dynamics. The PKA first hits the brown carbon atom and then hits the pink carbon atom. All three atoms are ejected from the graphene surface at the end. The red arrow shows the direction of the PKA.

varies greatly with the azimuthal angle. This is because the azimuthal angle of the ejected PKA is influenced by the azimuthal angle of the incident ion. The PKA direction with respect to the PKA neighboring atoms determines the defect structure that can be created. The formation of TV requires two subsequent collisions after the initial collision, and such collision sequence is more favorable at certain azimuthal angles. At an azimuthal angle of 75°, the occurrence probability of TV is higher than that at an azimuthal angle of 30°, and a cluster of TVs is seen when the ion impact position is 20°–40° relative to the PKA (see Figure. 2.10(c) and (d)). The formation dynamics of TV in this region is illustrated in Figure 2.11. The PKA first hits a neighboring carbon atom (in brown) and is then deflected by that atom, which causes it to hit a second carbon atom (in pink). At an azimuthal angle of 30°, this specific PKA ejection angle is less probable so that this collision sequence is less favorable. It can also be noted that the polar angle of the incident ion will also impact the direction

of the PKA and, consequently, the probability of the collision cascade that leads to TV. At a polar angle of 75°, the momentum from the incident ion has a direction more parallel to the graphene plane, the possible collision sequences that lead to a TV are different from those at a polar angle of 30°. The defect types at different impact positions are presented in Figure 2.10, showing the relationship between the azimuthal angle, impact position, lattice structure, and defect type. Due to the crystal lattice symmetry (see Figure 2.1(b)), the results at 0° and 15° should be close to that of 60° and 45°, respectively. This symmetry is observed for SVs and DVs but is not apparent for the other types of defects due to the stochastic nature of the collision process. The azimuthal angle was studied here because under certain experimental irradiation conditions, there is a fixed azimuthal angle relative to the crystal structure of the sample. The azimuthal angle does not appear to have a significant impact on the defect generation process. However, for a more comprehensive study, a complete survey using different ion energies and polar angles should be performed.

Next, the polar angle was studied at 15°, 30°, 45°, 60°, and 75°, and the results are shown in Figure 2.12. For this study, the azimuthal angle was randomly chosen from 30° to 90°. For SV, the probability increases with increasing polar angle at an E_H of 1, 10, and 100 keV. However, it first increases but then decreases at an E_H of 0.1 keV. The increase in the SV probability for all ion energies is due to the fact that the projected impact area at the graphene plane becomes larger at higher polar angles. For example, at a polar angle of 75°, the distance between the hydrogen and carbon atom at the graphene plane is much larger than the minimum distance between the two atoms (the impact parameter). This effect leads to the elongated impact area along the direction of the ion, as shown in Figure 2.10 and Figure 2.13. At 0.1 keV, the proton interaction time around a carbon atom is long due to its smaller velocity. Therefore, the momentum change caused by the PKA neighboring atom is sufficient to deflect the path of the proton so that it becomes difficult to approach the PKA.

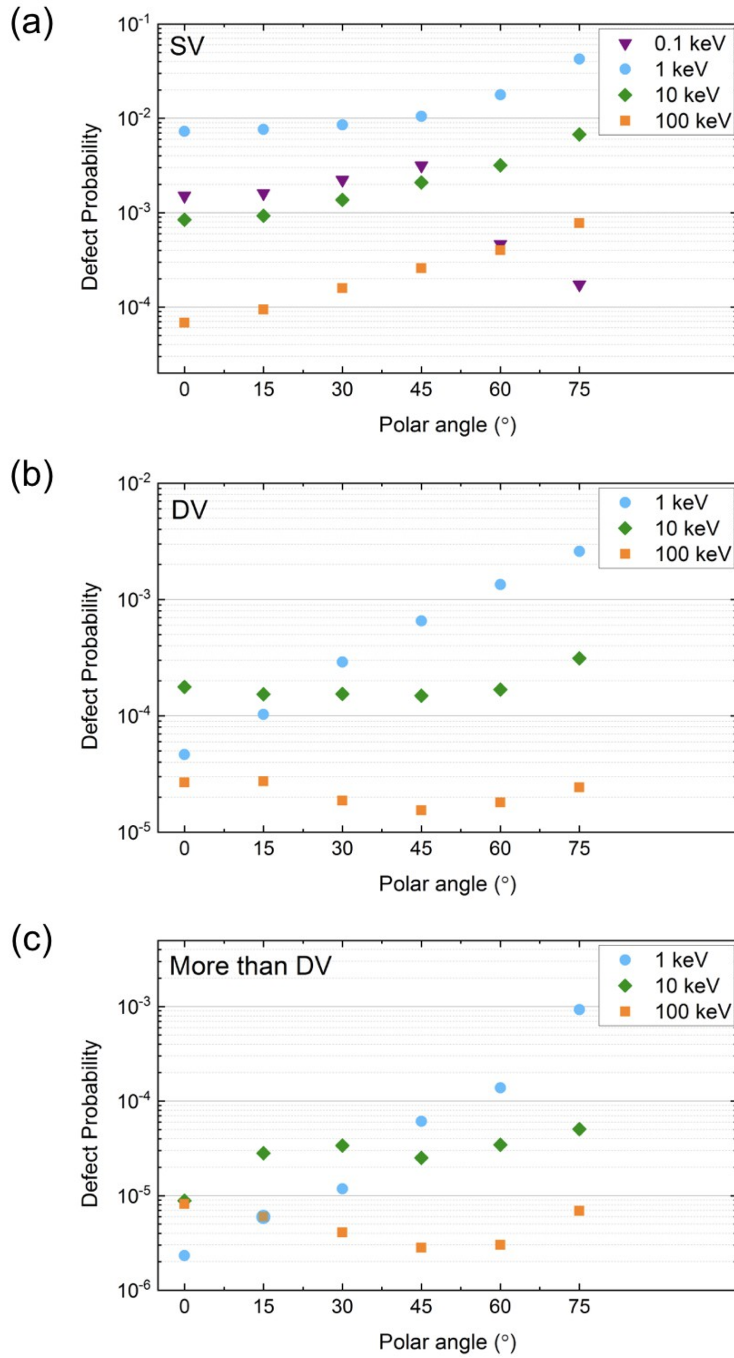

Figure 2.12: The generation probabilities of (a) SV, (b) DV, and (c) multiple vacancies (more than DV) as a function of the polar angle of the incident proton.

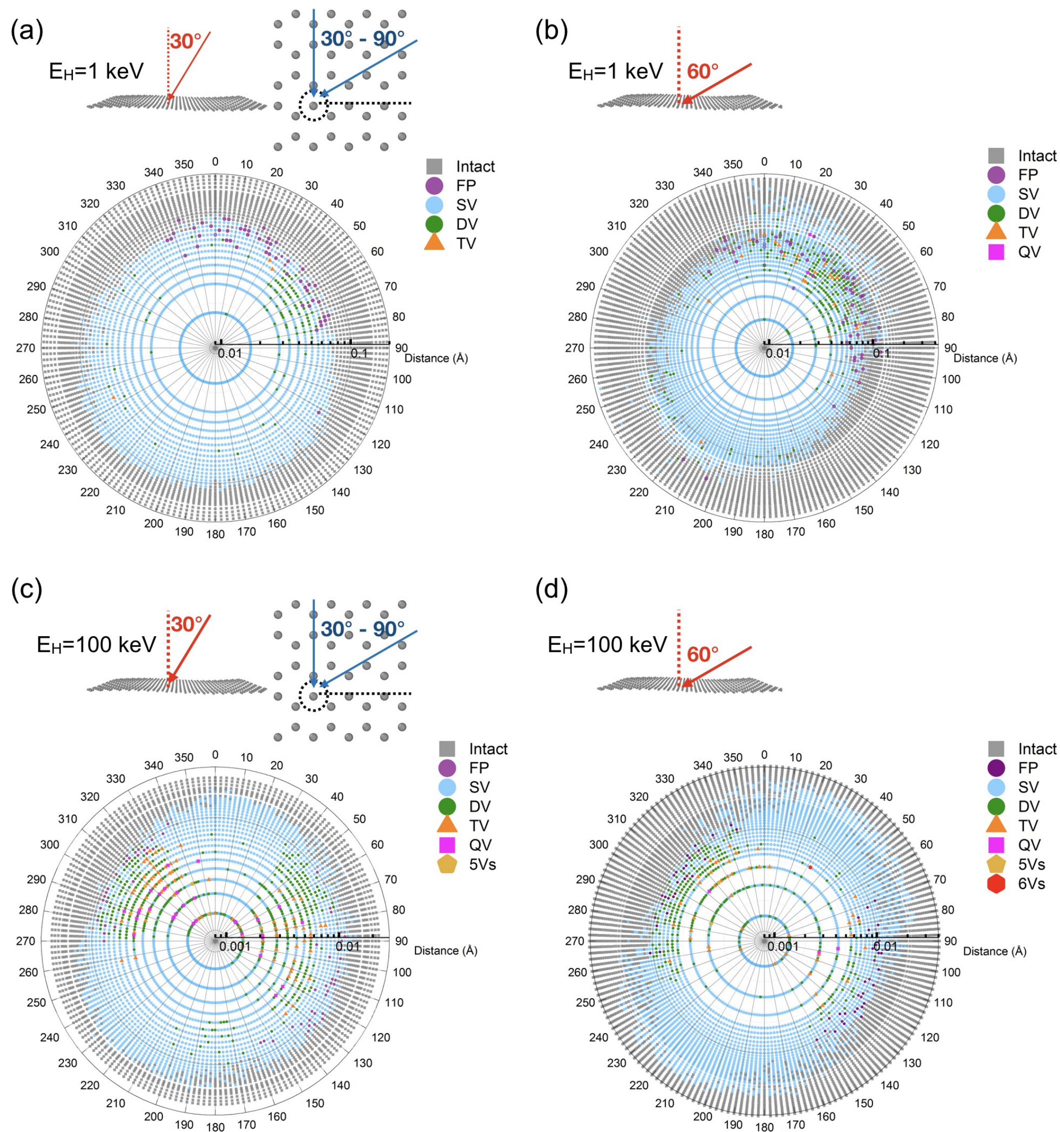

Figure 2.13: Defect types as a function of the impact position of the proton at different incident angles. At an incident energy of 1 keV, the results are shown for a polar angle of (a) 30° and (b) 60°, respectively. At an incident energy of 100 keV, the results are shown for a polar angle of (c) 30° and (d) 60°, respectively. The azimuthal angle was randomly sampled between 30° and 90° due to the crystal symmetry. The SV probability increases with the polar angle, as manifested by an elongated impact area along the proton direction. At 1 keV, a significant increase in the DV probability can be observed from (a) to (b). In comparison, there is only a moderate change at 100 keV, as shown from (c) to (d).

As a result, the SV probability decreases at large polar angles because only at large polar angles, are the neighboring atoms close enough to the path of the proton to deflect its trajectory.

The probabilities of DV and multi-vacancies increase rapidly with polar angles at 1 keV but exhibit a more moderate variation at 10 and 100 keV. In order to produce DV or multi-vacancies, the PKA needs to be ejected in a direction nearly parallel to the graphene plane and the PKA needs to have sufficient energy to knock out another atom. At 1 keV at near normal incidence, the PKA kinetic energy is not sufficient to displace another atom when such a direction is possible. By increasing the polar angle, both the direction and the energy criteria can be satisfied with a higher probability. At 10 and 100 keV, the energy criterion can be easily satisfied due to the higher ion kinetic energy. This explains why only at 1 keV do the probabilities of DV and multi-vacancies increase significantly with polar angle. Besides the aforementioned explanation, it should be noted that the variation of the defect generation probabilities is a convoluted response of the polar angle, ion energy, and impact position, as reflected from Figure 2.13.

2.3.5 Discussion

As discussed in the previous sections, depending on the proton energy and incident angle, proton irradiation can produce various types of vacancies and defect structures. These defects are created immediately after irradiation and experience further migration, agglomeration, annealing, or structural transformation over longer time scales. For example, DFT calculations showed that 5-8-5 DV has an energy 7.2–8.7 eV lower than separate SVs so that the formation of a DV from two SVs is energetically favorable [114]. A prior experiment with electron beam irradiation also showed that SV is observed less frequently compared with the DV due to its higher defect energy and mobility [115]. Similarly, TV is also more energetically favorable than a separate SV

and DV [115]. In addition, point defects can also be joined together to form extended and complex defect structures [114].

The proton-induced defect structures can alter the structural, electrical, and physical properties of graphene and this has been extensively discussed in the literature [92, 114, 116]. A small concentration of vacancies can actually increase the electronic conductivity of graphene by generation of midgap states, which creates a metallic region near vacancy sites [117]. Further increase in the vacancy concentration creates scattering centers and results in a decrease in the conductivity [117–119]. In terms of the mechanical properties, vacancies are expected to significantly decrease the Young's modulus and tensile strength only when they are present in large concentrations [120]. With respect to the chemical properties, vacancies are useful in providing reactive sites for chemisorption and intentional doping [121, 122]. Functionalization of graphene can be achieved by a two-step process: first introduce vacancies by ion irradiation and then introduce dopants into the reactive vacancy sites [67]. It is also shown that SV itself can greatly enhance the binding energy of hydrogen atoms for applications related to hydrogen storage. In order to achieve mono-dispersive SV, a low proton energy is desirable. Based on Figure 2.7, a proton energy of 0.1 keV results in a large SV yield with a low probability of creating other types of defects. Based on Figure 2.12, an incident polar angle of 45° can further increase the SV yield by a factor of 2.1 with respect to normal incidence.

Table 2.1: Graphene defect generation probabilities induced by 2-MeV protons simulated with the LAMMPS code.

Defect type	FP	SV	DV	TV
Defect probability per ion	1.42×10^{-6}	2.66×10^{-6}	1.48×10^{-6}	5.37×10^{-7}
Defect type	QV	PV	>PV	Total
Defect probability per ion	8.90×10^{-8}	4.24×10^{-8}	3.49×10^{-8}	6.27×10^{-6}

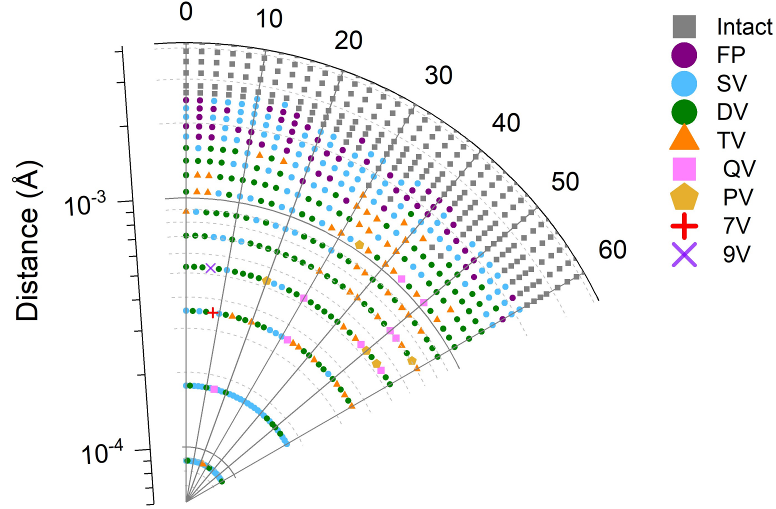

Figure 2.14: Defect types as a function of the impact position of the proton for an incident energy of 2 MeV at normal incidence simulated with the LAMMPS code. For defect configurations with no, one, two, three, four, five, seven, and nine atoms being ejected out of the simulation system, they are labeled as FP, SV, DV, TV, QV, PV, 7V, and 9V, respectively.

In order to help understand the previous experiment on proton irradiation of graphene [30], classical MD simulations were also performed with 2-MeV protons using the same approach. The probabilities of different types of defects are presented in Table 2.1 and the defect types at different impact positions are presented in Figure 2.14. With 2-MeV protons, it is shown that the most common defect structures are FP, SV, and DV. The defect probabilities decrease with the number of vacancies. Although the overall defect generation probability is low, it cannot be ignored if graphene is irradiated with a high proton fluence. It has been reported that for monolayer graphene, at a proton fluence of 10^{16} ions/cm^2, the D peak in the Raman spectrum, which is caused by disordered graphene structure, starts to become visible [30]. At this fluence level, the density of defective sites per Å^2 and the values in Table 2.1 have a one-to-one ratio. The total defect probability is 1.64×10^{-5}, corresponding to one defect site per 6.1×10^4 carbon atoms. The order of magnitude is consistent with the values determined from Ar^+ irradiation [123].

2.4 Summary

Using both *ab-initio* and classical MD simulations, the structures and generation probabilities of different types of graphene defects were determined under proton irradiation. It has been shown that in order to accurately and efficiently model the ion irradiation process, a variable timestep and an adaptive position sampling scheme are crucial. Although only a limited set of impact positions was sampled with the SIESTA code, a relatively good agreement was found between the *ab-initio* and classical MD simulation except at a low proton energy (0.1 keV), where the classical MD simulation underestimates the SV generation probability due to the sensitivity of SV probability on the accuracy of the potential at this low proton energy. Nevertheless, similar defect structures have been observed from both simulation approaches, and can also be compared to the irradiation experiments and prior simulation work. When the proton energy is high, a rich variety of defects can be produced due to the large energy injection from the incident ions. The physical reasons for the variation of the probabilities of different types of defects as a function of the proton energy and incident angle were discussed, which can also be applied to other 2D materials and ion species. It has been shown that the generation probabilities and the relative ratios of different types of defects can be effectively tuned by adjusting the proton energy and the incident angle. The obtained results will be important for defect engineering, material property tuning, as well as assessment of radiation damage for the development of radiation-tolerant materials.

CHAPTER III

Proton and Heavy Ion Irradiation of Layered WSe_2

3.1 Introduction

Layered transition metal dichalcogenides have received much attention in recent years because of their outstanding chemical [7], optical [8], and electronic properties. Tungsten diselenide (WSe_2), a layered material with a direct bandgap of 1.65 eV in the monolayer form, exhibits attractive electronic properties such as a high on/off current ratio [124] and high mobility [125], which make it a candidate for next-generation low-power electronic devices [126, 127]. Significant progress has been made in fabrication of WSe_2 by controlled growth via MOCVD [128] and molecular beam epitaxy [129]. Novel transistors [130, 131] and optoelectronic devices [132] have been constructed based upon WSe_2. However, the effects of ionizing radiation on WSe_2 have not been extensively explored, and the understanding of radiation effects is critical for assessing the potential of WSe_2-based electronics for use in high-radiation environments. Protons and heavy ions are major components of cosmic rays, and for this reason the damage induced by proton and heavy-ion bombardment in WSe_2/SiC heterostructures was studied.

Many previous irradiation studies of layered materials have focused on graphene and MoS_2. Here, the chemical and optical modification and the electronic property changes to the heterostructure consisting of layered WSe_2 and bulk silicon carbide

(6H-SiC) were studied by proton and heavy-ion irradiation using XPS and ultraviolet-visible spectroscopy (UV-Vis-NIR). Although ions can produce damage along the entire length of their tracks, the XPS surface characterization technique was used for the determination of sample damage only near the WSe_2 channel region, since a material modification near the channel region would have a significant impact on the charge carrier transport in an electronic device based on WSe_2 material, such as a transistor. Proton damage was investigated due to its significance for space applications, since cosmic radiation consists primarily of energetic protons. It has been reported for graphene that proton-induced damage depends on sample thickness and substrate interaction [133]. Thus, proton irradiation effects in WSe_2/SiC heterostructures were compared from two different fabrication methods: WSe_2/SiC heterostructures with relatively thick mechanically exfoliated WSe_2 and WSe_2/SiC heterostructures with ultrathin as-grown WSe_2 using the MOCVD growth technique. Although cosmic rays are mostly composed of protons and helium nuclei, it is also worth investigating the impact of heavier ions, which experience higher stopping power and are thus expected to produce a higher damage rate. The heavy ions account for 1% of the nuclei in cosmic rays, but the damage from a heavy ion is significantly larger than that from a proton. Furthermore, heavy ions can be used to simulate neutron radiation damage by virtue of their comparable damage mechanism and greatly reduced irradiation time [35, 134, 135].

3.2 Methods

Three types of samples were prepared: SiC with WSe_2 surface flakes, SiC with no WSe_2 surface flakes, and mm-scale bulk WSe_2 crystals. The 400 µm thick semi-insulating 6H-SiC wafers were obtained from II-VI Incorporated, while bulk WSe_2 crystals were obtained from 2D Semiconductors, Inc. For the first type of samples, WSe_2/SiC heterostructures were prepared by mechanically exfoliating WSe_2 flakes

from a bulk crystal and depositing them onto a sample of 6H-SiC (0001). The thickness of the flakes ranged from several layers to several µm. The optical images of the mechanically exfoliated WSe_2 samples used in Subsection 3.3.1 and Subsection 3.3.2 are shown in Figure A.1 and Figure A.2(a) in Appendix A, respectively. All SiC substrates were cleaned using the following procedure: sonication in acetone and isopropanol for 10 minutes each; rinsing in deionized water; wet clean in NanoStrip^{TM} for 20 minutes; rinsing; drying off using a nitrogen gun.

The MOCVD WSe_2 samples were grown in a vertical cold wall reactor on 6H-SiC substrates. Growth was conducted at 800 °C for 20 minutes with tungsten hexacarbonyl ($W(CO)_6$; purity: 99.9%) and hydrogen selenide (H_2Se; purity: 99.9%) as precursors for the respective elements. Hydrogen gas was used as the transport agent, and the ambient pressure was 700 Torr. The ratio of H_2Se to $W(CO)_6$ was ∼12,000, with ∼440 sccm of hydrogen gas flowed through the system. One subset of MOCVD samples was characterized using scanning electron microscopy (SEM), and the other subset was used for irradiation. An image of the MOCVD-grown WSe_2 taken using SEM (see Figure A.2(b) in Appendix A) shows that single-layer to few-layer crystals were grown with a density of approximately 4.5 triangles per µm^2, a domain size of hundreds of nanometers, and an estimated surface coverage of 36%. In addition, the MOCVD WSe_2 domains were aligned with respect to each other. With the small lattice mismatch between WSe_2 (a = 3.3 Å) and 6H-SiC (a = 3.1 Å), epitaxial growth was expected. However, interface states were also present and could impact the electronic properties [136]. All the WSe_2 samples were prepared by our collaborators (Roger Walker *et al.* from Prof. Joshua Robinson's group at the Pennsylvania State University). The XPS measurement was performed by Roger Walker and the analysis of the XPS data was performed by Roger Walker and Tan Shi.

Proton and heavy-ion irradiation was carried out at the Michigan Ion Beam Laboratory at University of Michigan. For exfoliated WSe_2 samples, the irradiation was

performed with 200-keV protons at fluences of 10^{16} protons/cm^2 and with 2-MeV protons at fluences of 10^{14}, 10^{15}, 10^{16}, and 10^{17} protons/cm^2. For MOCVD WSe_2 samples, the irradiation was carried out with 200-keV protons at a fluence of 10^{16} protons/cm^2 and 2-MeV protons at a fluence of 10^{15}, 10^{16}, and 10^{17} protons/cm^2. The proton fluence experienced by space electronics during their typical lifetime is within the range of fluences investigated experimentally in this work [137]. The heavy-ion experiments were performed with 2.5-MeV Fe ions, 5-MeV Fe ions, and 4-MeV Ag ions at a fluence of 10^{16} ions/cm^2. The ion beam was raster-scanned over the sample area of 6×6 mm^2 at an angle of $\sim$7° from the normal to sample surface to avoid channeling effects. The ion beam current density was kept within the range of 300–500 nA. The irradiation temperature was monitored in real time by thermal imager and kept between 50 °C and 100 °C to avoid selenium desorption due to thermal effects. The samples were stored in a vacuum chamber before and after the irradiation at a typical pressure of 0.1 Torr. The XPS was performed one day before irradiation, two to three days after irradiation, and two weeks after irradiation. XPS measurements were performed to determine the stability of the samples in air and medium-level vacuum. For the proton irradiation results presented in Subsection 3.3.1, XPS measurements were performed with a Kratos Axis Ultra spectrometer. For the proton irradiation results presented in Subsection 3.3.2 and heavy-ion irradiation results presented in Subsection 3.3.3, the XPS measurements were performed with a PHI VersaProbe II spectrometer. Both XPS tools use monochromatic aluminum K_α X-rays (1486.6 eV). All samples were charge-referenced to adventitious carbon at 284.8 eV and mixed Gaussian-Lorentzian peak fits were used. A low energy electron flood gun was used during the XPS measurement for charge compensation. The UV-Vis-NIR spectroscopy was performed using a Perkin-Elmer Lambda 950 spectrophotometer. Transmittance data was collected for wavelengths ranging from 250 nm to 2000 nm, and then converted into absorbance as a function of photon energy.

3.3 Results and discussion

3.3.1 Proton irradiation of exfoliated WSe_2

Prior to proton irradiation, the stability of exfoliated WSe_2 in vacuum and in air was evaluated. It is well-known that selenide-based TMDs can be oxidized in air at room temperature over long periods of time [138]. To determine if the oxidation is significant over the time frame of the experiment (several days), SiC samples with WSe_2 surface flakes (WSe_2/SiC) were prepared and characterized via XPS. The samples were then either left in air or stored inside a vacuum chamber under a medium vacuum (10–100 mTorr). After three days, the samples were removed and characterized again by XPS. Comparison of the spectra for the core tungsten shells (W 4f; see Figure 3.1) reveals that only two visible peaks are present in both cases, which are attributed to WSe_2 (W $4f_{5/2}$ and W $4f_{7/2}$). For the sample in air, the binding energy of the W $4f_{7/2}$ peak has an initial position of 32.31 eV that shifts upwards slightly to 32.40 eV. For the sample in vacuum, there is no significant shift of the W $4f_{7/2}$ binding energy. These values for binding energy are in good agreement with the previously reported results for WSe_2 [124, 139]. Since oxidation is known to cause a downshift of the binding energy [139, 140], it can be concluded that no significant oxidation of exfoliated WSe_2 occurs over the studied time period for either case.

After confirming that the samples do not oxidize in the experimental environmental conditions within the experimental time frame, samples of WSe_2/SiC, bulk SiC, and bulk WSe_2 were prepared and characterized by XPS. Samples were then either irradiated by 2-MeV protons or left unexposed as control samples. It is apparent from the XPS data that no oxidation (determined by the lack of appearance of tungsten oxide peaks as shown in Figure 3.2.) was induced in the exfoliated WSe_2 by proton beam irradiation. However, the observed variation in the position of W 4f peaks appears to depend on the proton fluence (Figure 3.2). No significant variation of the

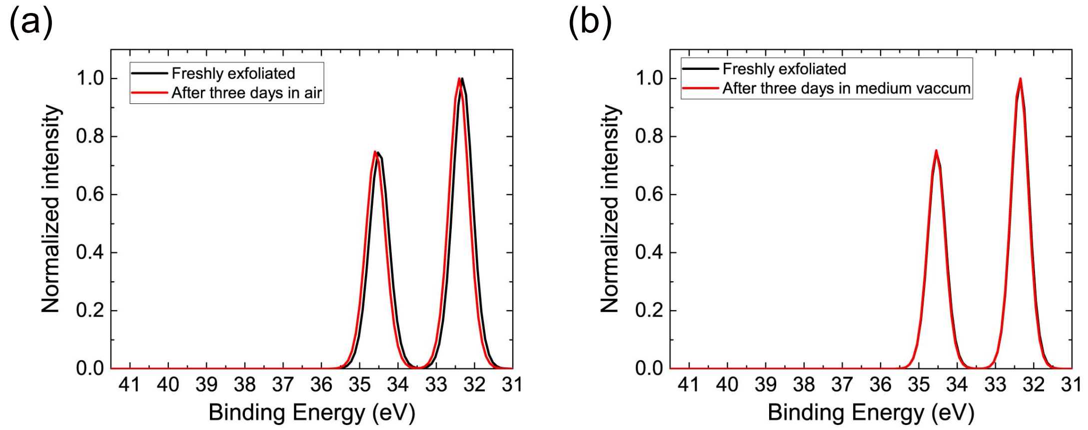

Figure 3.1: The stability of the exfoliated flakes in (a) medium vacuum and (b) air has been demonstrated via XPS. The two peaks in the W $4f_{7/2}$ window both correspond to WSe_2. No significant tungsten oxide formation was found to occur within the time frame of these measurements. The initial W $4f_{7/2}$ positions and shifts were (a) 32.35 eV, + 0.01 eV; (b) 32.31 eV, + 0.09 eV.

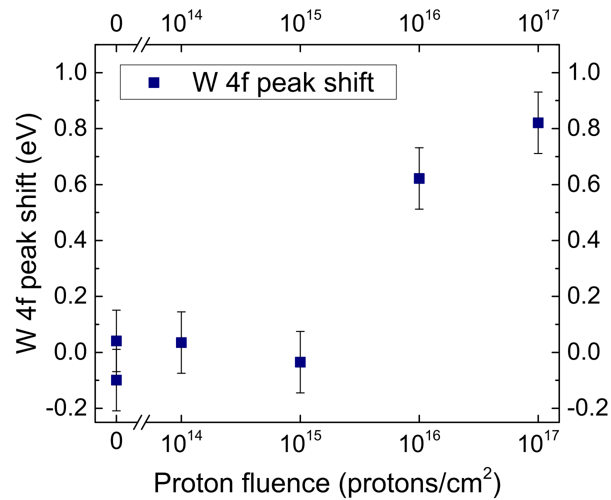

Figure 3.2: The binding energy shift of the W $4f_{7/2}$ peak position (∼35 eV) as a function of proton fluence. Data points at zero fluence correspond to control samples.

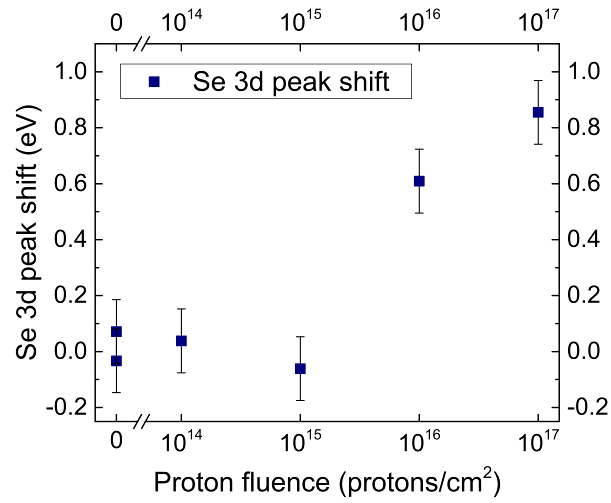

Figure 3.3: The binding energy shift of the Se 3d$_{5/2}$ peak position (∼54 eV) as a function of proton fluence.

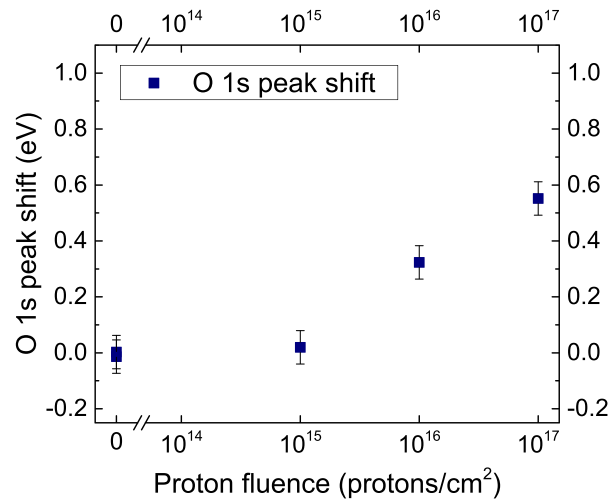

Figure 3.4: The binding energy shift of O 1s peak position (∼532 eV) from surface oxygen as a function of proton fluence.

XPS spectra was observed for the control samples or when the samples were irradiated at lower fluences (10^{14} and 10^{15} protons/cm^2). However, a measurable increases in binding energy of ~0.6 eV and ~0.8 eV were observed for the samples irradiated at 10^{16} and 10^{17} protons/cm^2, respectively. The same trend was observed for selenium (as measured via the Se 3d spectra; see Figure 3.3), and a similar trend was observed for oxygen (as measured via the O 1s spectra; see Figure 3.4(c)) where surface oxygen is attributed to the adsorption of oxygen onto the SiC substrate. However, the upshift for the O 1s peak, ~0.3 eV at 10^{16} protons/cm^2 and ~0.5 eV at 10^{17} protons/cm^2, is smaller than that of the WSe_2 XPS signature. Significant shifts in peak positions for carbon (C 1s) or silicon (Si 2p) were not observed until the irradiation fluence reached 10^{17} protons/cm^2, and they were on the order of ~0.2 eV for C 1s and ~0.3 eV for Si 2p. Since the XPS resolution is approximately 0.1 eV and there could be differential charging due to the non-uniformity of the exfoliated flakes, a shift of 0.2–0.3 eV for C 1s and Si 2p peak is not statistically significant. However, the W 4f binding energy shift of 0.6 eV and 0.8 eV are significant when compared with the equipment resolution.

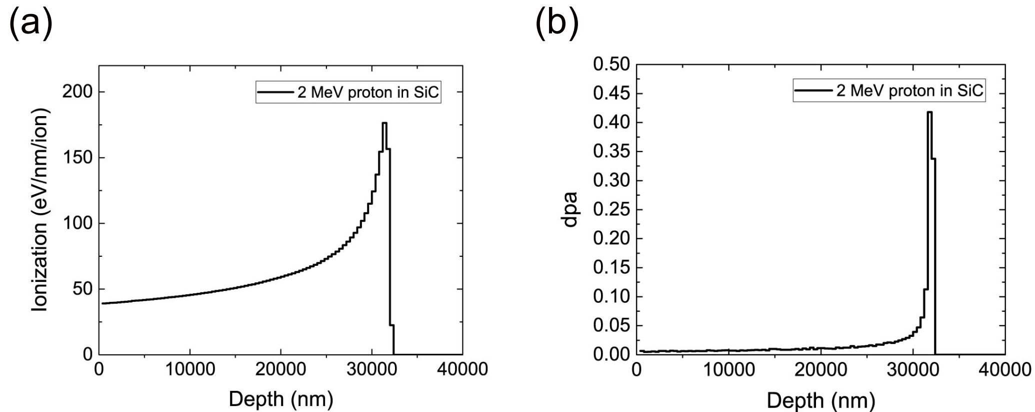

Figure 3.5: The depth profile of ionization and dpa in SiC estimated from the SRIM/TRIM simulation. (a) Ionization depth profile of 2-MeV proton in SiC; (b) dpa of 2-MeV proton in SiC at 10^{17} protons/cm^2. The monolayer collisions calculation type was used in the SRIM/TRIM simulation.

The observed peak shifts are attributed to charge buildup resulting from pro-

ton/substrate interactions. The 2-MeV protons penetrate 32 μm deep into the SiC substrate, as estimated by the SRIM/TRIM software package [1]. A proton loses energy along its track via two mechanisms: inelastic collisions with bound electrons in the medium (electronic ionization and excitation) and elastic collisions with nuclei. The electronic energy loss is dominant at short depths, where the layered WSe_2 is located, while nuclear stopping only becomes important at the end of the particle range (see Figure 3.5 for the depth profile of proton-induced ionization and displacement per atom (dpa) in 6H-SiC). Since a proton is relatively light in comparison to the nuclei that make up the irradiated sample, the probability of displacement damage to the surface material is very small (~0.007 dpa for a fluence of 10^{17} protons/cm^2 in the first 10 nm of the WSe_2 surface, as calculated by SRIM/TRIM). This is consistent with the absence of an oxidation peak, as measured by XPS after the irradiation. The ionization is mostly responsible for the charge transfer at the WSe_2/SiC interface, which causes the XPS core-level peak shift. Although a small positive shift of W 4f peak to the order of ~0.15 eV can be induced by extensive oxidation [141, 142] and there could be oxidation below the detection limit of XPS, the relatively large W 4f peak shift (~0.6 eV for a fluence of 10^{16} protons/cm^2 and ~0.8 eV for a fluence of 10^{17} protons/cm^2) can be mostly attributed to the charge transfer at the WSe_2 interface. Based on SRIM/TRIM simulations, the electronic energy loss within the WSe_2 and SiC at the sample surface is approximately 56 eV/nm and 39 eV/nm, respectively. Since the probability of direct interaction between a proton and WSe_2 is small, most of the interactions occur within the substrate. The onset of a measurable charging effect in the WSe_2 is seen at a fluence of 10^{16} protons/cm^2. This fluence corresponds to a relatively high radiation dose in comparison to doses known to induce effects on the operation of TMD transistors. For example, trapped charges in dielectrics such as silicon dioxide can degrade the device electrical characteristics of TMD transistors at a dose level that is two to three orders of magnitude lower

than used in this experiment [32], suggesting that degradation in TMD-based device architectures is not due to the TMD layer, but the surrounding materials. The XPS peak shift observed in our experiment can be interpreted as charge transfer due to a combination of direct damage to WSe_2, indirect effects from the substrate, and carrier trapping by interface states.

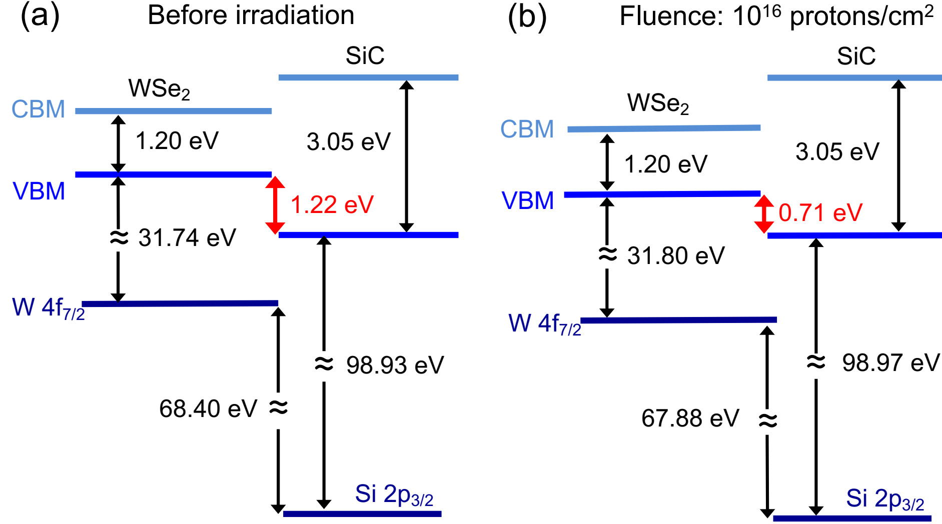

Figure 3.6: VBO between WSe_2 and SiC in the WSe_2/SiC heterostructure. The VBO was calculated using XPS spectra and was found to decrease after proton irradiation. It is assumed that the bandgap was not modified by the proton beam exposure (CBM: conduction band minimum).

Samples of bulk WSe_2 and SiC were also exposed to protons at 10^{16} protons/cm^2 in order to analyze the effect of proton damage on the band alignment between these two semiconductors. To the best of our knowledge, this is the first attempt to measure the valence band offset (VBO) between these two materials using XPS. The VBO between these materials was determined from the following equation [143–145]:

$$\Delta E_v = \Delta E_{CL}(i) + (E_{W\ 4f}^{WSe_2} - E_{VBM}^{WSe_2}) + (E_{Si\ 2p}^{6H-SiC} - E_{VBM}^{6H-SiC}). \qquad (3.1)$$

Here, $\Delta E_{CL}(i)$ is the energy difference between the two selected core shell states of the studied heterojunction (in this case, between W 4f and Si 2p states of the

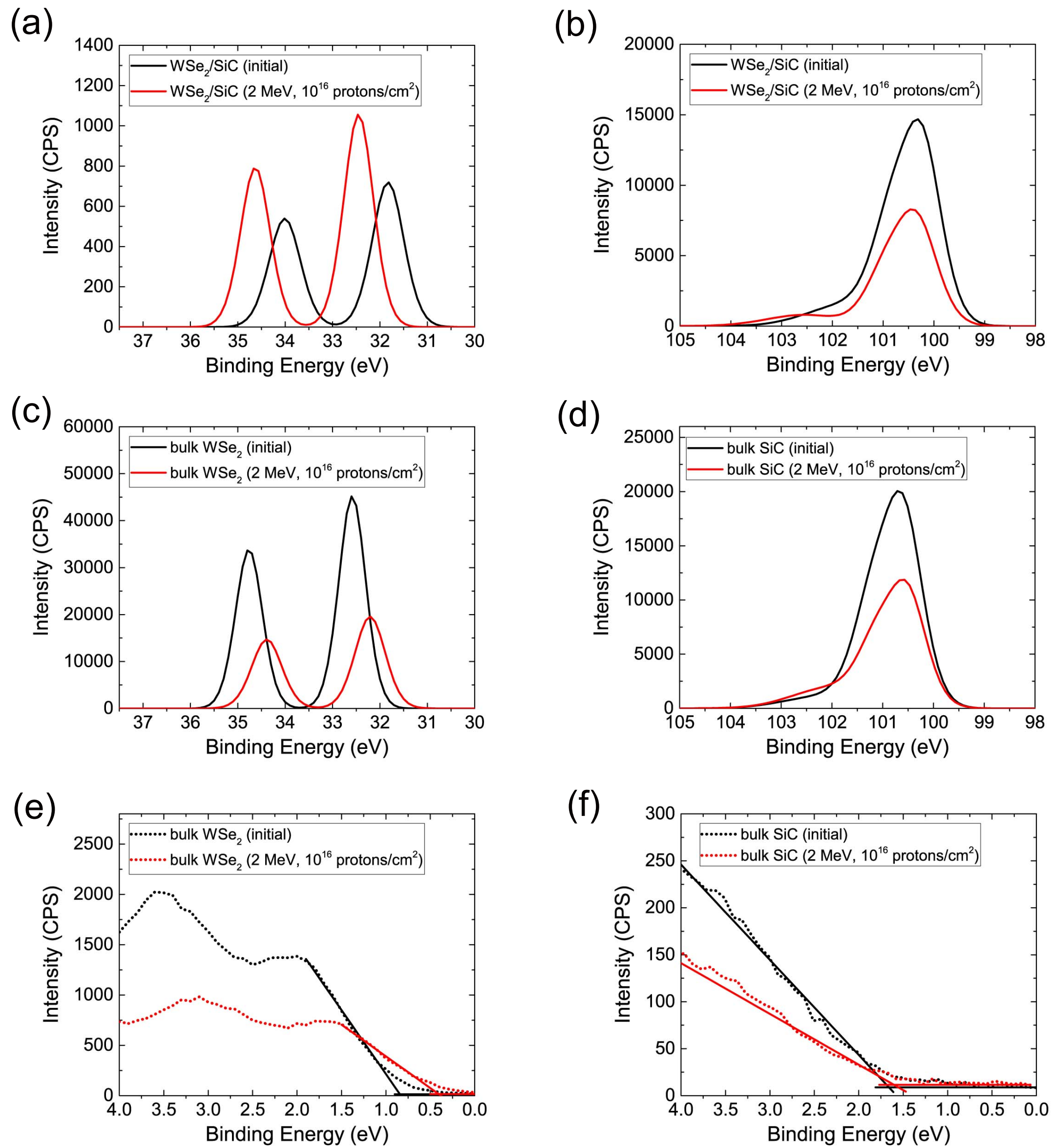

Figure 3.7: XPS spectra used in the calculation of VBO between WSe_2 and SiC upon exposure with 2-MeV protons at a fluence of 10^{16} protons/cm^2. The VBO between WSe_2 and SiC in the WSe_2/SiC heterostructure can be calculated using XPS by determining the binding energy difference between (a) W 4f and (b) Si 2p in WSe_2/SiC heterostructure, energy difference between (c) W 4f and (e) valence band edge in bulk WSe_2, and energy difference between (d) Si 2p and (f) valence band edge in bulk SiC.

WSe_2/SiC heterostructure). The band alignment before and after radiation damage is schematically shown in Figure 3.6(a) and (b). The core level separation at the interface was determined to have an initial value of 68.4 eV, decreasing to 67.9 eV upon proton beam exposure. This decrease in the core level separation originates from the charging processes described above. Interface states would not affect the VBO because they would contribute to the WSe_2 and SiC equally and their contribution to VBO would cancel out [143]. The valence band maximum (VBM) was measured by applying a linear regression to the low binding energy edge of the valence band spectrum for both the bulk WSe_2 and the bulk SiC samples. As shown in Figure 3.6, the VBO between WSe_2 and SiC decreases from 1.22 ± 0.24 eV to 0.71 ± 0.24 eV after proton beam exposure at 10^{16} protons/cm^2. Spectra used for the calculation of VBO are shown in Figure 3.7. The error bar of 0.24 eV is estimated from the error of six measurement values, where an error of 0.1 eV for each measurement is used. The proton beam exposure had a minimal effect on the separation between the core-level peak and VBM of bulk SiC or bulk WSe_2. The primary cause of the VBO change is the shift of the W 4f peak relative to the Si 2p peak in the WSe_2/SiC heterostructure.

Regarding the ion irradiation effects on the SiC substrate, the dependence of amorphization and annealing on dose and temperature, as well as other property modifications, have been previously studied [146, 147]. The conversion of the crystalline and transparent SiC to a heavily defective and either darkened (partially translucent) or black (opaque) Si_xC_y material was observed deep within the substrate for the samples exposed to 10^{16} and 10^{17} protons/cm^2, respectively (see Appendix A Figure A.3). The color change was also witnessed in a sample of exfoliated MoS_2 on SiC substrate after exposure to 10^{16} protons/cm^2 at 2 MeV. In light of this change, the light absorbance properties of a control sample and sample exposed to 10^{16} protons/cm^2 were measured in order to examine how the color change in proton-irradiated SiC correlates to optical properties. While XPS provides information on the chemical bonds

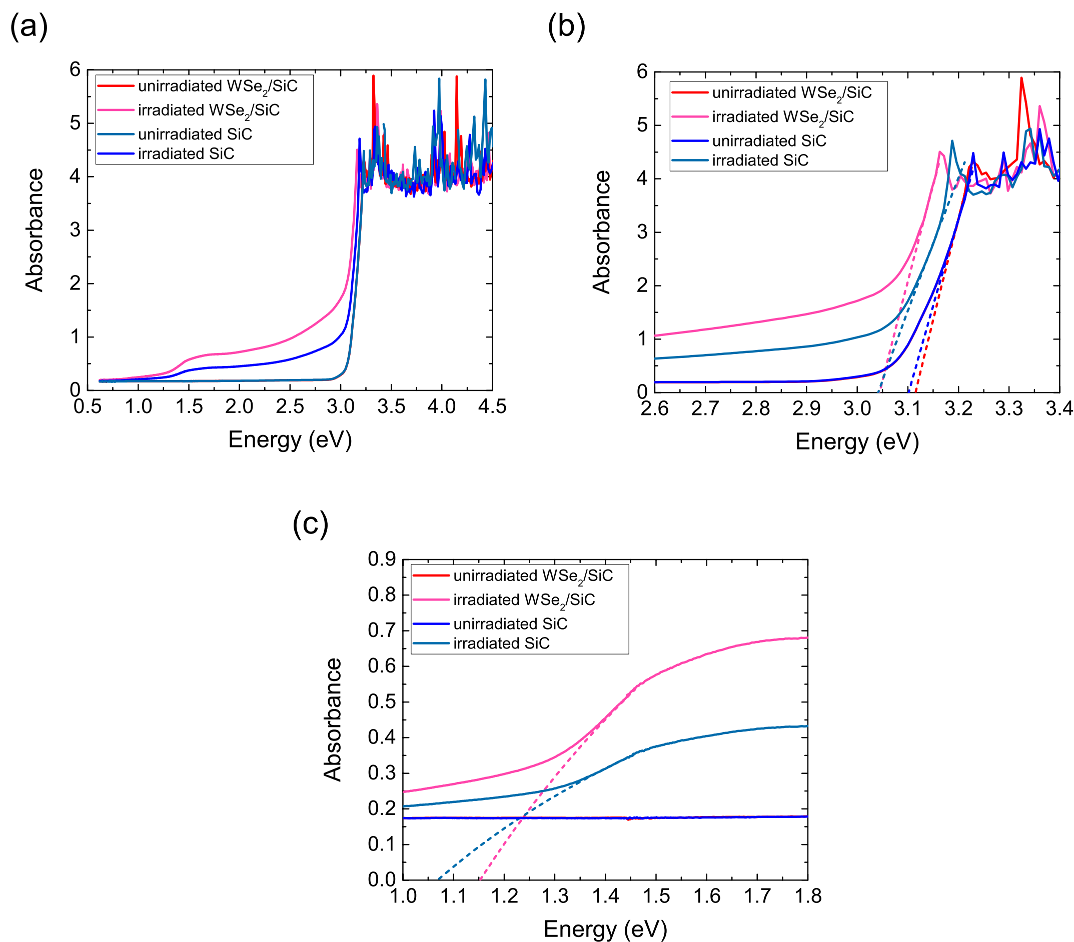

Figure 3.8: UV-Vis-NIR spectra before and after 2-MeV proton irradiation at a fluence of 10^{16} protons/cm^2. (a) The measured UV-Vis-NIR spectra reveal irradiation-induced changes in the optical properties of the SiC substrate. Magnified regions of the plot (a) depict the changes in the absorption edge corresponding to (b) the SiC bandgap and (c) the new absorption edge created around 1.1 eV due to the irradiation-induced vacancy-rich region deep in the SiC substrate.

within the first ∼10–20 nm of the surface, the UV-Vis-NIR spectroscopy provides an absorption spectrum of the entire sample in the lower energy range of the electromagnetic spectrum. The absorbance data obtained are shown in Figure 3.8. For all samples, there is a sharp increase in the light absorbance for photons with energy at or above 3 eV, corresponding to the bandgap of 6H-SiC (Figure 3.8(b)). Additionally, a new feature appears in the irradiated samples at ∼1.5 eV, with an absorption edge at ∼1.1 eV (Figure 3.8(c)). This absorbance feature appears to result in the black color of the irradiated SiC, as this energy lies in the near-infrared part of the spectrum. This is explained by the generation of a deep acceptor in the SiC bandgap near $E_c - 1.1$ eV [148, 149]. This deep acceptor results from point defects such as the silicon single vacancy, the carbon single vacancy, and carbon anti-sites [150, 151].

3.3.2 Proton irradiation of MOCVD-grown WSe_2

In this section, the proton irradiation results from MOCVD-grown WSe_2 are presented. There are two main factors that make it difficult to determine whether MOCVD-grown WSe_2 and exfoliated WSe_2 have a similar response to proton radiation. First, MOCVD growth is usually accompanied by a greater density of interface states [152]; and second, the exact chemical composition and the doping level are also different in the two techniques. The MOCVD samples used in the experiment have a consistent Se:W ratio of ∼2.1, meaning that WSe_2 is Se-rich and there is a pre-existing concentration of holes with p-type conductivity. In comparison, the exfoliated WSe_2 samples have an ideal Se:W ratio of 2 although they are also p-type doped due to the intrinsic W vacancy defects [153]. These differences may lead to different charging behavior induced by proton irradiation. Therefore, comparisons between the MOCVD and exfoliated samples were made with the goal of determining the extent to which the irradiation effects are influenced by the material fabrication method.

Table 3.1: Initial binding energies of core level peaks for WSe_2 and SiC in a heterostructure.

Core level peak	Binding energy for exfoliated WSe_2 on SiC heterostructure (eV)	Binding energy for MOCVD WSe_2 on SiC heterostructure (eV)	Binding energy difference (eV)
W $4f_{7/2}$	31.94	32.72	0.78
Se $3d_{5/2}$	54.19	54.96	0.77
Si $2p_{3/2}$	100.39	101.39	1.00
C 1s	282.66	283.64	0.98

Besides the experimental results shown in Subsection 3.3.1, irradiation of additional exfoliated WSe_2 samples was also performed for comparison with the MOCVD samples. The initial XPS spectra before the proton irradiation show that the only detectable sources of contamination common to exfoliated and MOCVD WSe_2 are surface oxygen and adventitious carbon (see Appendix A Figure A.4 and Figure A.5). Exfoliated WSe_2 on SiC exhibits a weak Na 1s peak, indicating a small amount of sodium contamination, likely a byproduct of the exfoliation process. Analysis of the core level peaks reveals that there is no oxidation of the WSe_2 or SiC surface detectable by XPS.

After charge calibration to the XPS peaks, it is shown that the initial binding energies vary with the heterostructure fabrication method. This difference is presented in Table 3.1, where the core-level W and Se peaks for MOCVD WSe_2 have higher binding energies than those of exfoliated WSe_2. The binding energies of core-level Si and C peaks are also higher in MOCVD samples. This is partially due to the fact that MOCVD WSe_2 has a larger bandgap since its thickness is close to monolayer. In addition, there is a greater density of interface states produced during the MOCVD growth, which is known to influence the measured binding energies in XPS spectra at the WSe_2 and SiC interface [143, 154].

Shown in Figure 3.9 is the binding energy shift induced in the MOCVD WSe_2 and exfoliated WSe_2 by exposure to 2-MeV protons at various fluences. In Figure 3.9, part of the exfoliated data have been presented in Subsection 3.3.1, and are labeled

as "prior work" here to distinguish from the new results reported in this subsection. Shifts from both the W 4f and Se 3d spectra are shown, and there is good agreement in shifts between spectra from the same material. This is also observed for the SiC data discussed later. It was determined from Subsection 3.3.1 that a fluence of 10^{16} protons/cm^2 is needed to induce a significant positive binding energy shift (and thus a positive charge) in the exfoliated WSe_2. Given the fluence rates in space [137], this corresponds to lifetime of years to decades. The results presented here suggest that a fluence of 10^{16} protons/cm^2 is needed to induce binding energy shifts in the MOCVD WSe_2 as well.

There are two key differences observed between samples fabricated by the two methods. One is that the binding energy decreases for the MOCVD-generated heterostructure, rather than increasing as in the heterostructure generated by mechanical exfoliation. This result is unexpected based on our previous results, and it is likely due to the trapped charges in the interface states generated by the MOCVD growth. The charging effect originates from a combination of charging directly in the TMD and charge transfer from the substrate. The pre-existing trapped positive charge at the interface appears to have influenced the proton-induced charging process. Negative peak shift indicates a p-type doping effect in the WSe_2. This means that the there is either an increase of traps for positive charges or a decrease in the electron traps. Either case would have the same effect on the XPS spectra, and analysis using electrical measurements would be needed to uniquely identify the prevailing mechanism. Based on the MD simulation of 2-MeV proton irradiation of monolayer graphene and MoS_2 presented in Chapters I and IV, the density of defect sites and the sputtering ratio at a fluence of 10^{16} protons/cm^2 are about one order of magnitude below the XPS detection limit ($\sim 0.1\%$). Thus, the interactions with existing defects and interface states should be the dominant reason for the shift of the core-level peaks.

The second difference is that the extent of charging induced in the MOCVD

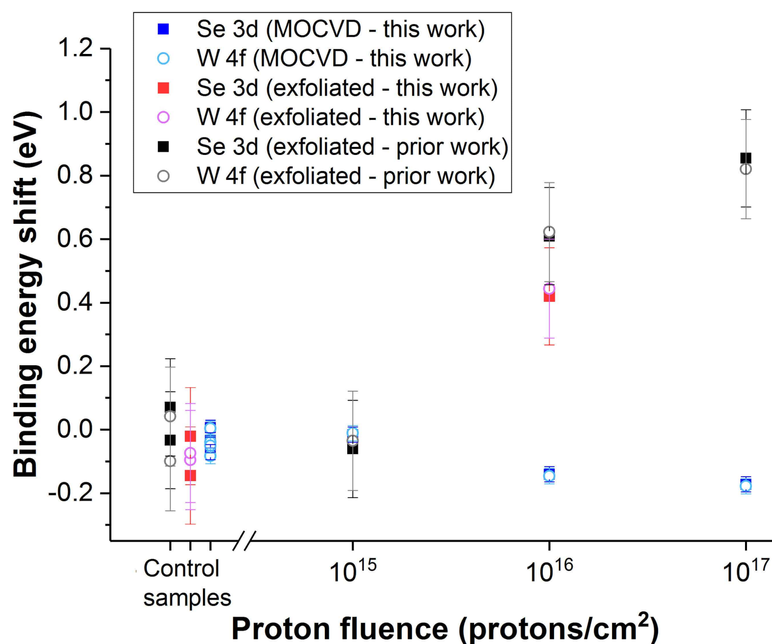

Figure 3.9: Binding energy shifts induced in the Se 3d and W 4f peaks of the exfoliated and MOCVD WSe_2 samples by exposure to 2-MeV protons at various fluence levels.

WSe_2 (peak shift of W 4f and Se 3d peaks: -0.2 eV) is small when compared with the extent of charging in the exfoliated WSe_2 (+0.4 eV to +0.7 eV). It has been shown before that an increase in the coupling strength between two-dimensional materials and the substrate can reduce the damage done by X-rays [155, 156]. In addition to the intralayer sp^2 bonds for layered WSe_2, the bonding between WSe_2 and the substrate increases the overall bonding strength and may reduce the extent of charging effect. The coupling originates from substrate interactions that occur during growth to stabilize the 2D layers so that thin film growth may occur [128, 156]. As such, the protective effect from that strong coupling is expected and was observed.

Corresponding data for the SiC substrate is shown in Figure 3.10. Here, the surface chemistry and surface charging within the penetration depth of XPS (down to ~20 nm) were analyzed. Based on the core-level peak shift in XPS, the SiC charged to a similar extent as the WSe_2 in the case of MOCVD-grown material, but charged up significantly less than the exfoliated WSe_2 in the case of exfoliated material. The

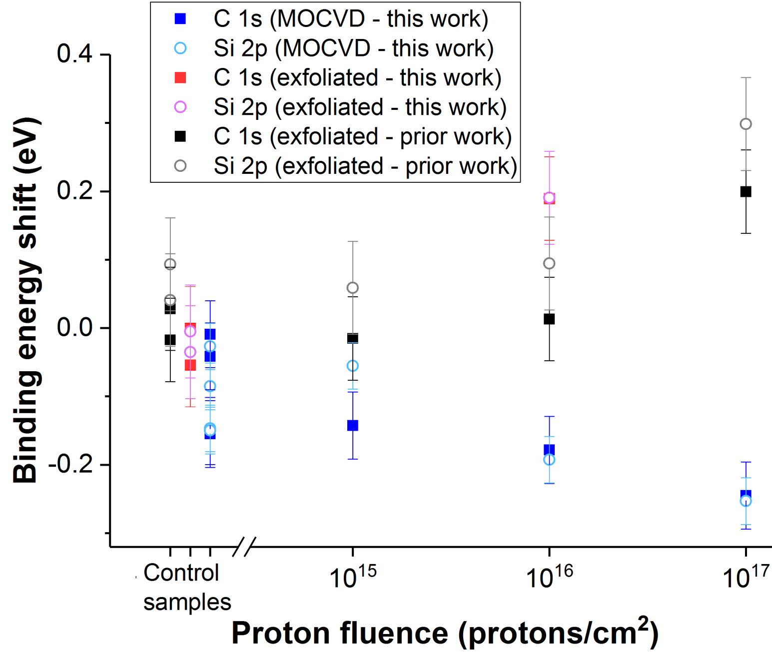

Figure 3.10: Binding energy shifts induced in the C 1s and Si 2p peaks of the SiC substrates by exposure to 2-MeV protons at various fluence levels.

charge build-up in the case of MOCVD growth appears to occur mostly at the interface between the two materials, which would lead to similar observed shifts [143]. At a region near the interface, the interface states (or surface stats) will lead to the same potential shift on both sides of the interface [143]. Several factors may contribute to the similar shift of core-level peaks of WSe_2 and SiC. First, the ultra-thin nature of the MOCVD WSe_2 limits the amount of charge it can store far away from the interface. In the limit of ultra-thin films, as discussed in this work, such charging may not be possible. Second, any charge in the SiC very far away from the surface will not be detected by XPS and thus not observed. Third, although 100% coverage was not achieved, the 36% coverage and high domain density present here means that charging at the WSe_2 and SiC interface can have a strong influence on the XPS spectra. It appears that this coverage level is sufficient to have the interface be dominant in influencing the peak shifts when the WSe_2 is only one to a few layers thick. On the other hand, significant difference in charging means that more charging

occurs on one side of the interface than the other. Here, the exfoliated WSe_2 charges more than the substrate. This is attributed to a mix of charging directly in the thick exfoliated WSe_2, charge transfer between WSe_2 and SiC, and charging at the interface that affects them both equally. Based on these results, the charging in the exfoliated WSe_2 is dominated by charges that are generated directly in the thick WSe_2 film, far from the substrate interface. This may change in the case of ultra-thin exfoliated films, where the interface becomes more important.

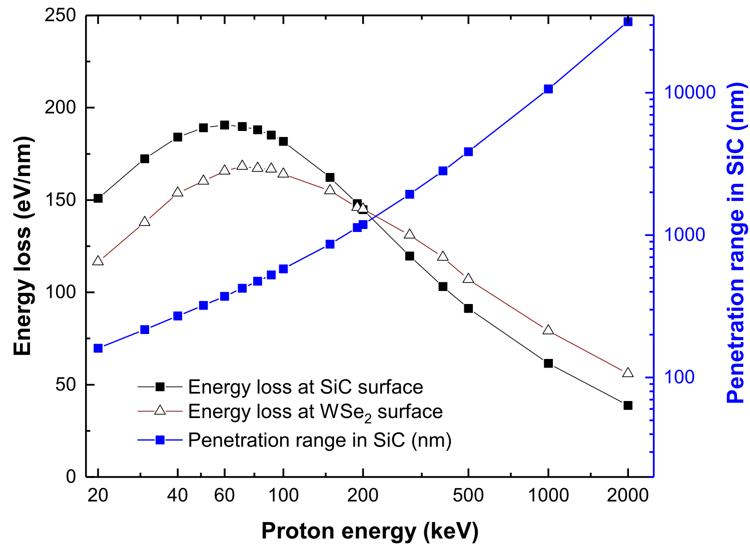

Figure 3.11: Energy loss of protons as a function of proton energy at the WSe_2 and SiC surface and penetration depth of protons within SiC substrate estimated with SRIM/TRIM simulation [1]. 200-keV and 2-MeV protons were used in our experiment. 200-keV protons have a shorter range in the substrate but have a higher stopping power compared with 2-MeV protons.

The energy that a proton can transfer to the surface of a material is expected to depend on its kinetic energy, as shown in Figure 3.11. As such, both exfoliated and MOCVD samples were exposed to 200-keV protons at a fluence of 10^{16} protons/cm^2, and the results are shown in Figure 3.12. Lower energy protons are expected to more effectively transfer energy at the sample surface; therefore, there should be greater extent of charging in both sample types. However, the charging induced in

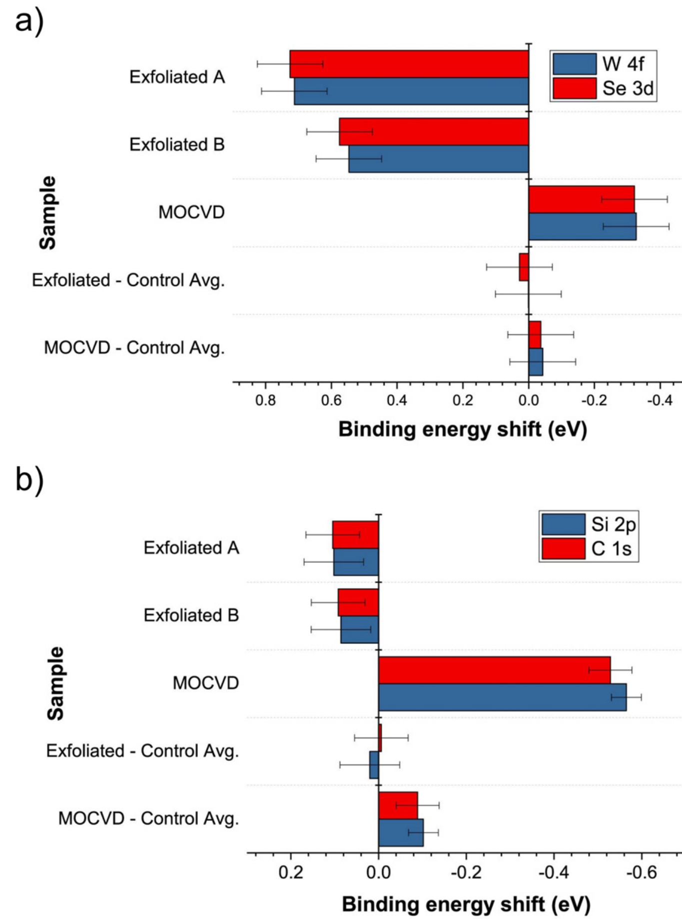

Figure 3.12: (a) Binding energy shifts induced in the Se 3d and W 4f peaks of the exfoliated and MOCVD WSe_2 by exposure to 200-keV protons at a fluence of 10^{16} protons/cm^2. (b) Binding energy shifts induced in the C 1s and Si 2p peaks of the SiC substrates by exposure to 200-keV protons at a fluence of 10^{16} protons/cm^2. Data from control samples is provided for comparison in both plots. Two exfoliated samples and one MOCVD sample were irradiated. Data from control samples is provided for comparison in both plots. Four exfoliated control samples and four MOCVD control samples were used.

the exfoliated WSe_2 after exposure to 200-keV protons is found to be comparable to the charging induced with exposure to 2-MeV protons. Based on the peak shift variation of different samples under the same irradiation conditions, the difference between samples irradiated with 200-keV and 2-MeV protons cannot be reflected by the extent of the peak shift although the energy loss per length differs by a factor of three. For MOCVD samples, the charging induced in the WSe_2 layer is different by approximately 0.1 eV, which is also a statistically insignificant change. Thus, it is hypothesized that the sample initial conditions (pre-existing defects, interface states, WSe_2 thickness, initial charging, *etc.*) play an important role in determining charging effects. For the SiC, the samples with exfoliated material behaved like the samples exposed to 2-MeV protons, while the sample with MOCVD-grown material charged more than the SiC with WSe_2 flakes. Although consistent negative charging of SiC was observed in MOCVD samples irradiated by protons with energies between 200 keV and 2 MeV, it is not clear why the charging in SiC was more significant at 200 keV. Future studies and more measurements will be needed to address this question.

To correlate these charging effects with changes in the electronic properties, the VBOs for WSe_2 on SiC were extracted and the changes induced by proton exposure were measured. The initial as-measured VBO and schematic band alignments are shown in Figure 3.13 for exfoliated WSe_2/SiC (Figure 3.13(a)) and for MOCVD-grown WSe_2/SiC (Figure 3.13(b)). The initial VBO is shown to depend on the heterostructure preparation method due to interface states. Bulk WSe_2 with a bandgap of 1.2 eV achieves Type I band alignment with SiC, while single layer WSe_2 with a bandgap of 2.2 eV achieves Type II band alignment with SiC. The electron affinities for bulk WSe_2 and for 6H-SiC have been previously reported at ∼4 eV [157] and ∼3.3 eV [158], respectively, leading to an expected 0.7 eV conduction band offset (CBO). This is close to the value extracted here for the exfoliated WSe_2 on SiC (0.5 eV), indicating

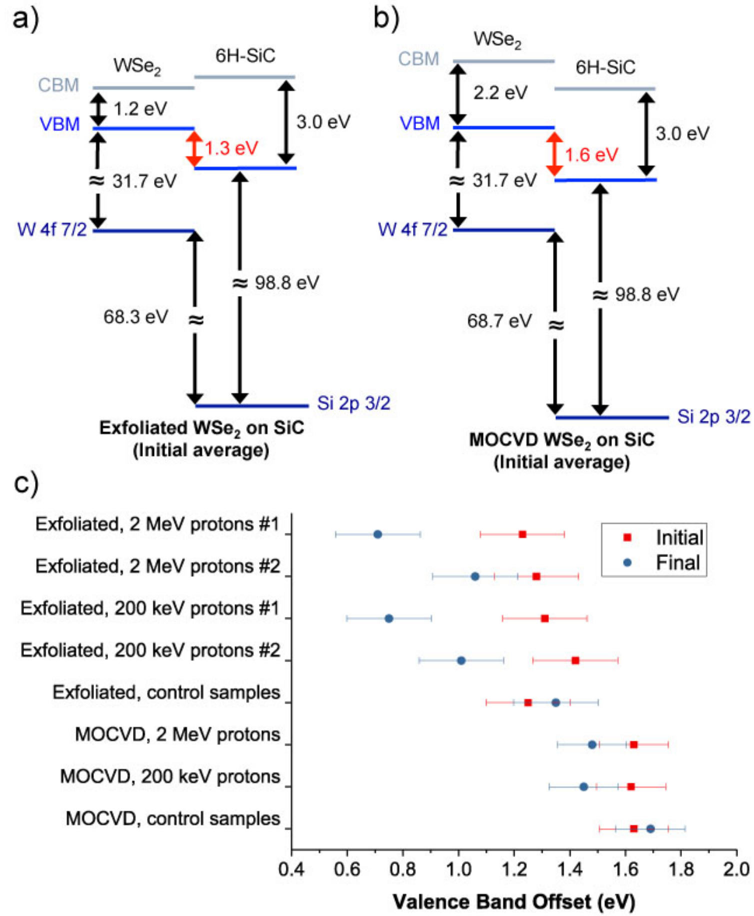

Figure 3.13: (a) Schematic band alignment between exfoliated WSe_2 and SiC. The bulk bandgap of WSe_2 is used due to the thick nature of the exfoliated flakes. (b) Schematic band alignment between MOCVD WSe_2 and SiC. The single layer bandgap value of WSe_2 is used due to the ultra-thin nature of MOCVD grown material. (c) Shifts in the valence band offset between WSe_2 and SiC induced by exposure to protons at a fluence of 10^{16} protons/cm^2. Several control samples were also analyzed and averaged together.

that interface states do not have a large impact. On the other hand, the extracted electron affinity for single layers of WSe_2 has been reported as ~3.3 eV [159, 160], indicating that the CBO between ultra-thin MOCVD WSe_2 and SiC would be zero and the VBO would be ~0.8 eV in the case of an ideal interface. The fact that this does not occur is a clear indication that significant populations of interface states affect the electronic properties of this heterostructure, having been induced by TMD-substrate interactions during the MOCVD growth process.

In general, as shown in Figure 3.13(c), the VBO is reduced by 200-keV and 2-MeV proton exposure and remains stable with no proton exposure. When the VBO is modified, the change comes mostly from differential charging at the interface – i.e. a larger core level peak shift in the WSe_2 than in the SiC in samples where the WSe_2/SiC interface can be analyzed, which changes $\Delta E_{CL}(WSe_2/SiC)$ defined in Equation(3.1). Again, the variation of the VBO for exfoliated samples under the same conditions indicates that the sample initial condition has a strong impact on the VBO shift. Notably, the modification of the VBO is much more significant for heterostructures generated via exfoliation than for those generated via MOCVD growth. This is expected based on the effects of greater substrate coupling and reduced thickness obtained by MOCVD growth. As such, the choice of heterostructure fabrication technique determines both the initial electronic quality of the interface and how it responds to stressors such as high-energy particles. Furthermore, maintaining the advantages of the MOCVD growth of WSe_2 while growing it on a more insulating, yet still radiation tolerant substrate would allow for atomically thin WSe_2 to form a basis for future space-based electronics scaled to reduced thicknesses. Such substrates include insulators such as diamond [161], and dielectrics such as silicon nitride [162, 163] and various high-κ oxides [164] (e.g. Al_2O_3, HfO_2, *etc.*).

3.3.3 Heavy-ion irradiation of exfoliated WSe_2

When a heavy ion interacts with matter, electronic energy transfer from excitations and ionization leads to local heating around the ion track. If the energy deposition is sufficiently high, structural damage can take place. On the other hand, collision cascades induced by the nuclear energy loss can also cause material damage. Table 3.2 shows the results of SRIM/TRIM simulations of the three irradiation conditions investigated in this work. Bulk material parameters for WSe_2 were used in the simulation since exfoliated WSe_2 has a relatively large average thickness (see Appendix A Figure A.3). The displacement threshold energy was set to 25 eV for W and Se for the calculation of dpa. For monolayer WSe_2, the displacement threshold energy is known to be lower. According to atomisitic calculations, the displacement threshold for Se atoms is ∼6.4 eV, assuming a 5×5 supercell of WSe_2 monolayer [46]. When there are fewer layers present, the displacement threshold tends to be lower, which results in a higher damage rate [133]. In addition, the coupling with the substrate will also affect the displacement threshold [133]. The penetration depth of the heavy ions used in the experiment is in the range of 1–2 µm. The nuclear stopping power of 2.5-MeV Fe ions is higher than that of 5-MeV Fe ions at the sample surface while the opposite is true for electronic stopping power. The dpa of 4-MeV Ag ions is approximately 2–3 times higher than that of Fe ions and is therefore expected to result in greater structural damage if the damage is not saturated.

While MeV-energy proton beam exposure leads to charging effects in the WSe_2 without significant chemical modification, exposure to heavy-ion beams at MeV energies leads to a partial transformation of WSe_2 into tungsten oxide (see Figure 3.15), as well as a partial transformation of SiC into SiO_2 and heavily defective SiC mixture (see Figure 3.16). Compared with protons, the probability of elastic collisions and the average energy transferred to the primary knock-on atom are much higher for heavy ions, which leads to larger collision cascades. Due to the higher nuclear

Table 3.2: Summary of the results from the SRIM/TRIM simulation. The dpa was calculated with a fluence of 10^{16} ions/cm^2 at the top 10 nm of the material, corresponding to the detection depth of XPS measurement. The monolayer collisions calculation type was used in the SRIM/TRIM simulation. The depth profiles of ionization and dpa in the SiC substrate induced by heavy ions are shown in Figure 3.14.

	Projected range in bulk WSe_2 (µm)	$(dE/dx)_{nucl.}$ at WSe_2 surface (MeV cm^2/mg)	$(dE/dx)_{elec.}$ at WSe_2 surface (MeV cm^2/mg)	dpa in WSe_2
2.5-MeV Fe^{2+} ion	1.00	0.47	2.04	3.7
5-MeV Fe^{4+} ion	1.73	0.30	3.58	2.3
4-MeV Ag^{4+} ion	0.93	1.51	1.98	8.7
	Projected range in bulk SiC (µm)	$(dE/dx)_{nucl.}$ at SiC surface (MeV cm^2/mg)	$(dE/dx)_{elec.}$ at SiC surface (MeV cm^2/mg)	*dpa* in SiC
2.5-MeV Fe^{2+} ion	1.24	0.90	7.16	0.74
5-MeV Fe^{4+} ion	1.98	0.55	12.1	0.47
4-MeV Ag^{4+} ion	1.23	6.99	2.76	1.6

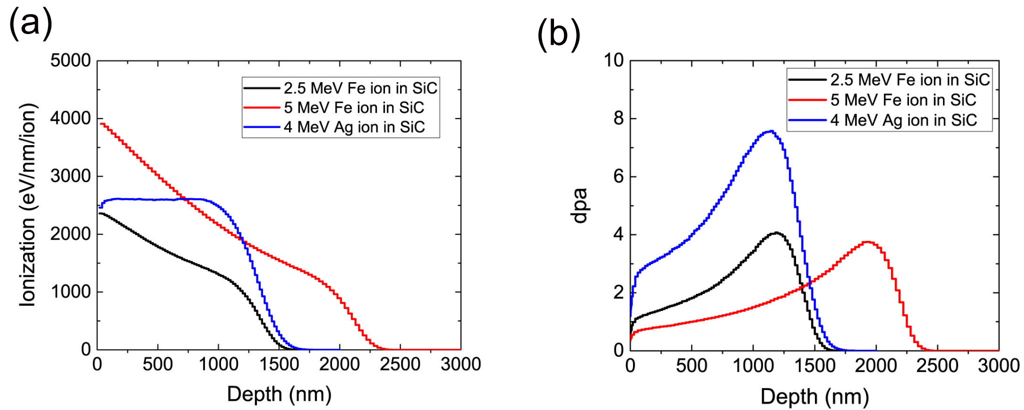

Figure 3.14: The depth profile of ionization and dpa in SiC estimated from the SRIM/TRIM simulation. (a) Ionization depth profile of heavy ions in SiC; (b) dpa of heavy ions at a fluence of 10^{16} protons/cm^2. The monolayer collisions calculation type was used in the SRIM/TRIM simulation.

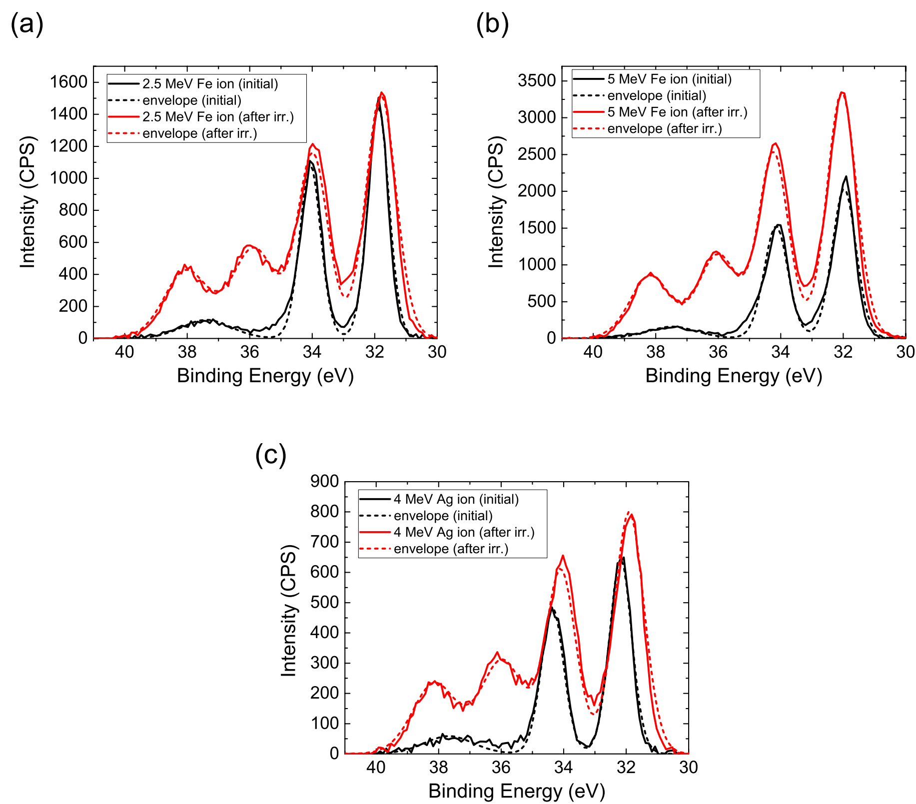

Figure 3.15: The change of XPS W 4f spectrum after heavy-ion irradiation with (a) 2.5-MeV Fe, (b) 5-MeV Fe, and (c) 4-MeV Ag ions at a fluence level of 10^{16} ions/cm^2. The XPS spectrum intensity is expressed in the units of counts per second (CPS). The appearance of two additional peaks at $\sim$36 eV and $\sim$38 eV after irradiation indicates the oxidation of tungsten.

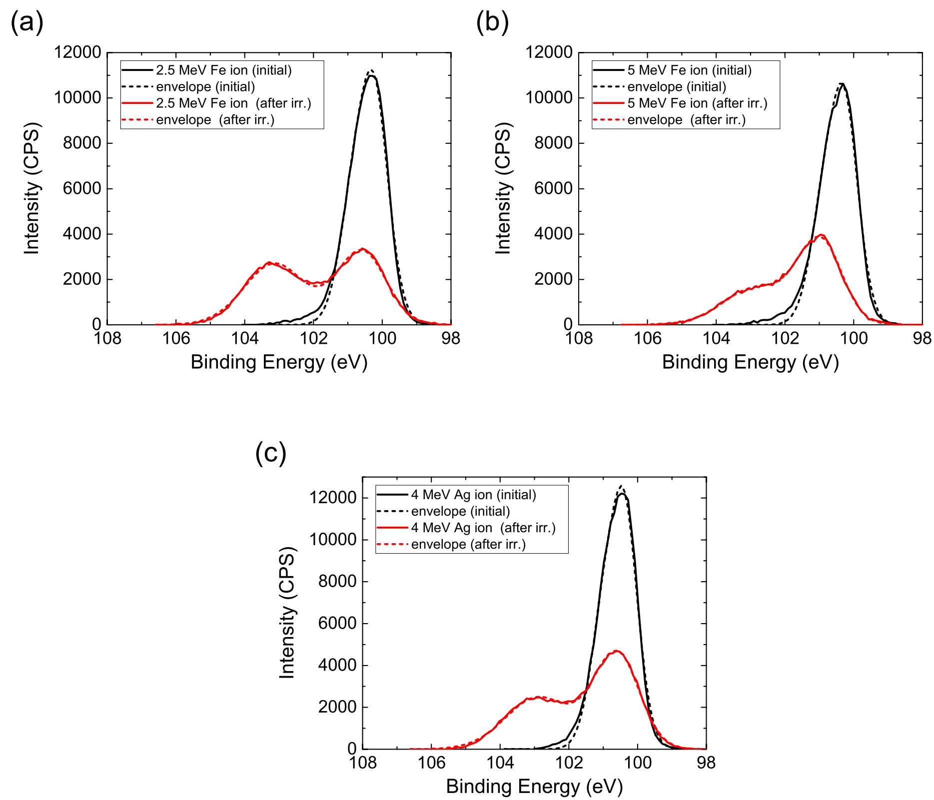

Figure 3.16: The change of XPS Si $2p_{3/2}$ spectrum after heavy-ion irradiation with (a) 5-MeV Fe, (b) 2.5-MeV Fe, and (c) 4-MeV Ag ions at a fluence of 10^{16} ions/cm^2. The appearance of new peak indicates the oxidation of silicon.

stopping power as reflected by the dpa values, the effects of sputtering, recoil mixing, and cascade mixing are more pronounced [35], which causes significant structural transformation at the sample surface. The ion beam exposure was carried out under high vacuum conditions ($< 10^{-8}$ Torr), and therefore the oxidation occurred due to the exposure to atmosphere during ex-situ XPS analysis. Initial XPS reveals that tungsten and selenium are only bonded to each other, corresponding to WSe_2. After heavy-ion irradiation, a second set of peaks emerges in the tungsten spectra that correspond to tungsten oxide based on peak positions of ~36.0 eV and ~38.2 eV [139] and the changes in the oxygen spectra that appear to indicate the formation of a metal oxide (see Appendix A Figure A.6). At the same time, there is a drastic reduction in the amount of selenium relative to the amount of tungsten. The initial Se:W ratio for these three samples is 1.96 ± 0.05 and is reduced to 0.68 ± 0.05 following heavy-ion bombardment (see Figure 3.17). This can be explained by the higher volatility of selenium compared with tungsten. It is estimated from XPS that the ratio of tungsten-oxygen bonding to tungsten-selenium bonding is 0.51 ± 0.05 after the beam exposure, and increases slightly after two weeks in storage due to continued oxidation. The Se:W ratio was also observed to decrease from a measurement made two weeks following the experiment, confirming the continued desorption of selenium from the sample. Although the dpa value of 4-MeV Ag is the highest among the three experiments and the dpa of 2.5-MeV Fe is the lowest, the magnitude of damage estimated on the basis of Se:W and WO_x:WSe_2 ratio is very similar in all three experiments and does not exhibit a clear trend. At the total ionizing dose levels used in this experiment, the amount of damage caused by the three ions to the WSe_2 may be similar enough that the different samples oxidize by roughly the same amount when exposed to air. Comparisons between samples exposed to varying dose levels will be needed to confirm if a correlation between dpa and oxidation exists. This correlation was studied for several other materials [165, 166] and the same methodology could be

applied to study the oxidation of layered materials. Other characterization techniques such Rutherford backscattering spectrometry and transmission electron microscopy could be used to study the induced damage at greater depths in the substrate.

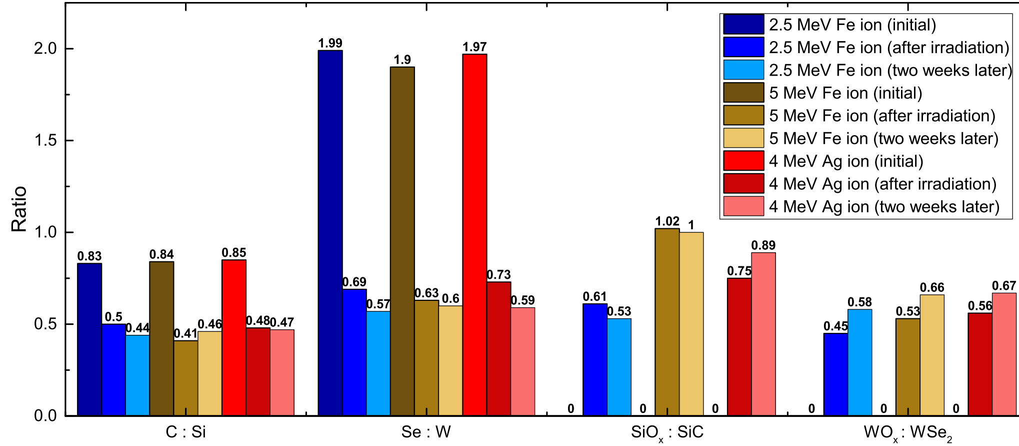

Figure 3.17: Compositional analysis of WSe_2/SiC heterostructure from XPS studies. The compositional ratio of C:Si, Se:W, SiO_x:SiC and WO_x:WSe_2 of WSe_2/SiC heterostructure before and after heavy-ion irradiation. No oxidation of silicon and tungsten has been detected before irradiation.

A change of composition was also observed for SiC, where the C:Si ratio drops from 0.84 ± 0.01 to 0.47 ± 0.05 (Figure 3.17) post irradiation. The initial spectrum for SiC has only one chemical state: a peak doublet corresponding to silicon carbide. After irradiation, another doublet centered around ~103 eV was created that is attributed to a silicon-oxygen compound [167], with silicon in a Si^{2+} or Si^{3+} state (Figure 3.16). Carbon was initially present in three states: carbon-silicon bonds; carbon-carbon sp^3 bonds; and carbon-oxygen bonds. Carbon-carbon and carbon-oxygen bonds are both attributed to adventitious surface carbon. These same states were observed after irradiation, but in different proportions — more of the carbon signal can be attributed to the two surface carbon states rather than to the SiC. Additionally, the binding energy of carbon determined from the carbon peak corresponding to SiC increases from 282.6 eV to 283.4 eV. The carbon binding energy for SiC in the range from 282.9 eV to

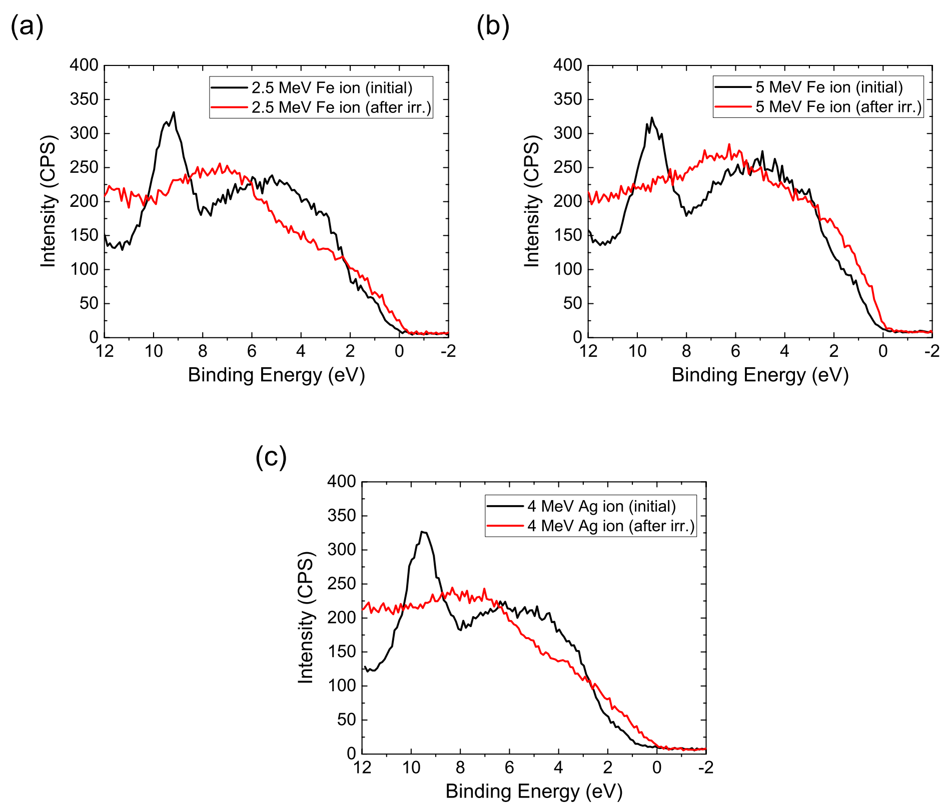

Figure 3.18: The change of XPS spectrum near the valence band region after heavy-ion irradiation with (a) 2.5-MeV Fe, (b) 5-MeV Fe, and (c) 4-MeV Ag ions at a fluence of 10^{16} ions/cm^2.

283.5 eV has been previously reported for SiC whiskers [168] and amorphous SiC [169]. It can be concluded that this shift corresponds to a transformation of the SiC from crystalline to amorphous. Complete amorphization of 6H-SiC corresponds to a damage level of ∼0.5–10 dpa, depending on the ion energy and species [147], and is thus expected.

A significant modification of the valence band structure was also observed via XPS (Figure 3.18). The initial spectrum consists of a single peak that is attributed to the SiC, as well as a broader feature at a lower energy that is a convolution of the SiC and WSe_2 valence orbitals. The VBM of the semi-insulating SiC substrate is typically located at ∼1.5 eV. Measurement of the VBM using a linear fit to the valence band edge reveals an average value of 0.36 eV due to the initial p-type doping of the exfoliated WSe_2. After irradiation, all samples show a shape change in the valence band spectra and lead to a VBM at or below the Fermi level using the linear fit approach, which indicates a loss of the semiconducting properties of the heterostructure. Additionally, the single peak has also vanished from the spectra due to the heavy-ion damage. The increases in the signal intensity around ∼8 eV and ∼2 eV are attributed to tungsten oxide [170] and silicon oxide [171] contributions to the valence band.

3.4 Summary

The effects of 2-MeV proton and heavy-ion bombardment on the WSe_2 and SiC heterostructure have been studied with XPS and UV-Vis-NIR spectroscopy. It was found that a proton fluence of $\sim 10^{16}$ protons/cm^2 is needed to influence the surface chemistry, band offset, and absorbance properties. No detectable new surface states were generated by proton exposure, but a charging effect was observed that is mostly attributed to the proton-induced ionization and excitation within both the WSe_2 and the SiC substrate. The difference in charging between WSe_2 and SiC leads to a change in the valence band offset, as measured by XPS. The buildup of point vacancies, such

as the silicon single vacancy, carbon single vacancy, and carbon anti-site also result in the modification of light absorbance properties within the SiC substrate. These two different effects would both have consequences for device performance based on this heterostructure, which should be evaluated in future work. Mechanical exfoliation of thick WSe_2 onto SiC leads to an interface that is relatively free of interface states and more vulnerable to proton-induced charging. MOCVD growth of WSe_2 onto SiC leads to the epitaxial growth of single-layer crystals with an interface that is strongly impacted by interface states and less impacted by high-energy proton exposure. In conclusion, due to the absence of chemical modifications of WSe_2 via XPS and the observation of charging effects only at very high proton fluence levels, the radiation resilience of TMD-based transistors is expected to be limited by the dielectric insulator and the substrate, which would degrade at a much lower proton fluence level [32, 172]. The bombardment of WSe_2/SiC heterostructure with heavy ions at high dpa levels leads to significant physical damage. Collisions between heavy ions and WSe_2 lead to structural disorder and the preferential ejection of selenium; therefore, the sample is oxidized once exposed to an oxygen-bearing environment. Collisions between heavy ions and SiC lead to the sputtering of both elements, but carbon is preferentially removed. These combined changes lead to heavy alteration of the band structure, which can be monitored by changes in the valence band spectra in XPS. It is expected that at this total ionizing radiation dose level, a device based on this heterostructure would be damaged beyond repair due to heavy damage to the WSe_2 channel. Further experiments to determine the threshold dose level for heavy ions, the dependence of ion-induced damage on the number of WSe_2 layers and growth techniques, as well as experiments tracking damage to devices such as diodes and transistors, would aid in developing a more complete understanding of the radiation hardness of WSe_2/SiC heterostructures and help to develop radiation-hardened systems based upon those materials.

CHAPTER IV

Ion Irradiation of MoS_2 Field-Effect Transistors

4.1 Introduction

Two-dimensional TMDs such as MoS_2 exhibit interesting semiconducting properties including bandgap tunability [173–175], good mobility [125], as well as high on/off current ratio [176]. Because of the advances in theoretical modeling [177], material synthesis [178], and device fabrication [8], high performance MoS_2 FETs [25, 179] and more complex digital components such as NAND gates and static random access memory [27] have been demonstrated. As the feature size of the state-of-the-art CMOS is approaching its fundamental limit due to the increase of the leakage current [180], layered TMD materials offer new device concepts [21] and provide new possibilities for transistor downsizing. This is particularly desirable for space applications where a reduced device weight and a lower energy consumption are sought. However, due to the atomically thin nature of the TMD channel layer, it is not fully understood how radiation would impact TMD-based FETs. The contribution from various damage mechanisms is unclear: while positive oxide charges are created by charge trapping in the dielectric, the direct damage to the TMD layer and the generation of interface states are intrinsically related to the properties of TMD materials, which differ from those of silicon CMOS technology.

Radiation effects on TMD FETs have been studied in several prior works. Fox *et*

al. [54] and Stanford *et al.* [53] studied He ion damage to MoS_2 and WSe_2, respectively, through Raman spectroscopy and electric measurements. Kim *et al.* [32] studied the evolution of MoS_2 FET I-V characteristics after the samples were irradiated with 10-MeV protons with a fluence in the range of 10^{12} to 10^{14} cm^{-2}. The degradation of the electric performance was explained by a combined effect of oxide-charge traps in SiO_2 and interface states, which is similar to the total ionizing effect of traditional silicon MOSFET [181]. In the work of Dhakras *et al.* [182], a reconfigurable WSe_2 FET was fabricated with three buried gates to tune the channel polarity in order to suppress the impact of Schottky barriers on the subthreshold characteristics. With proton fluence from 10^{11} to 10^{14} cm^{-2}, it was found that the creation of charges in oxide is the most relevant phenomenon, which leads to significant degradation of the subthreshold slope (SS). In the work of Lu *et al.* [183], MoS_2 FETs were irradiated by 30-keV low-energy electrons. A transition from negative to positive voltage shift with increasing aging time was observed and explained by the dominance of oxide charges immediately after the irradiation and the dominance of interface traps at high aging time. Besides protons and electrons, total ionizing effects induced by 10-keV X-rays and detrimental effects induced by energetic heavy swift ions have also been reported [58, 184]. In addition to TMD heterostructures, ionizing radiation effects on FETs based on 2D heterostructures and other low-dimensional materials, such as MoS_2/graphene [185], graphene [34], and carbon nanotubes [186, 187], have also been investigated in prior research.

Since radiation effects depend on the dielectric thickness [28], number of 2D layers [133], growth methods [76], processing techniques [28], and irradiation conditions, a range of effects was observed in different studies. Due to the effects from both the 2D channeling material and the dielectric material, it is sometimes difficult to isolate the damage to the standalone 2D material from the I-V measurement. First, ionization can create electron-hole pairs in the dielectric. Since holes have a low mobility,

a fraction of the radiation-induced holes can be trapped at defect sites and affect the FET bias. Second, charge carriers can be trapped at the interface between the channel material and the dielectric. These interface states can degrade the device mobility and shift the transistor threshold voltage. Third, structural damage can also take place within the TMD layer and degrade the device performance. For the interface states, if they are located in the lower half of the bandgap, they are more likely to become donor states, and if they are located in the upper half of the bandgap, they tend to become acceptor states [188]. When a donor state is above the Fermi level, the donor state releases an electron and becomes positively charged. When a donor state is below the Fermi level, the donor state becomes charge neutral. The acceptor states follow the same principle: when an acceptor state is below the Fermi level, the acceptor state accepts an electron and becomes negatively charged. For n-type channel material such as MoS_2, the interface traps are usually below the Fermi level and are negatively charged. This leads to a positive shift of the transistor transfer curve. In contrast, positive charges produced within the dielectric can cause a negative shift of the I-V curve. These two mechanisms lead to compensating effects, which make it difficult to decouple their contributions to performance degradation.

Besides the traditional methods of annealing tests such as current and capacitance measurement [189], a new experimental approach was used here to separate the effects of interface states and oxide charges so that the damage of MoS_2 can be accessed from proton and He ion irradiation. It was found that the MoS_2 nanosheets can withstand 2-MeV proton and 390-keV He fluences as high as $\sim10^{16}$ and $\sim10^{15}$ ions/cm^2, respectively, with a high on-and-off current ratio. In order to understand the physical structural damage induced by proton and He ions, MD simulations were performed to study the defect generation and sputtering process in monolayer MoS_2 at a range of proton and He ion energies up to 2 MeV. The defect generation probability, defect size distribution, and sputtering yield (SY) were obtained for 2-MeV protons and

390-keV He ions.

4.2 Methods

4.2.1 Experimental procedure

The irradiation and device fabrication procedure is illustrated in Figure 4.1. In the traditional approach the entire FET device is irradiated, including the substrate, channel layer (MoS_2 flakes), and source/drain contacts (see Figure 4.1(a)). The advantage is that one can compare the pre-irradiation and post-irradiation electrical characteristics of the same device. However, as explained in Section 4.1, the response can result from the simultaneous radiation damage of multiple device components. In the new approach, different components were irradiated separately. As shown in Figure 4.1(b)-(d), both the SiO_2 substrate and MoS_2 flakes, only the MoS_2, and only the SiO_2 substrate were irradiated. When only the flakes were irradiated, they were transferred to an unirradiated SiO_2 substrate using the wet transfer process (see Figure 4.1(e)). In all cases, the source/drain contacts were fabricated after the irradiation. They were first defined using electron beam lithography and then fabricated by depositing 40 nm of Ni and 30 nm of Au via electron beam evaporation. The device channel length was kept at 500 nm for all devices. The SiO_2 substrates were heavily doped with Si and were used as the back-gate of the FET devices. Electrical measurements were performed using a Keysight B1500A parameter analyzer after samples were irradiated and complete devices were fabricated. The samples were placed in a Lakeshore CRX-VF probe station and placed under vacuum. They were allowed to stay in vacuum overnight to remove any hysteresis effects or threshold voltage shifts caused by exposure of the MoS_2 to air. The device fabrication and electrical measurement were performed by collaborators (Andrew J. Arnold from Prof. Saptarshi Das' group at the Pennsylvania State University). More details on the device fabrication

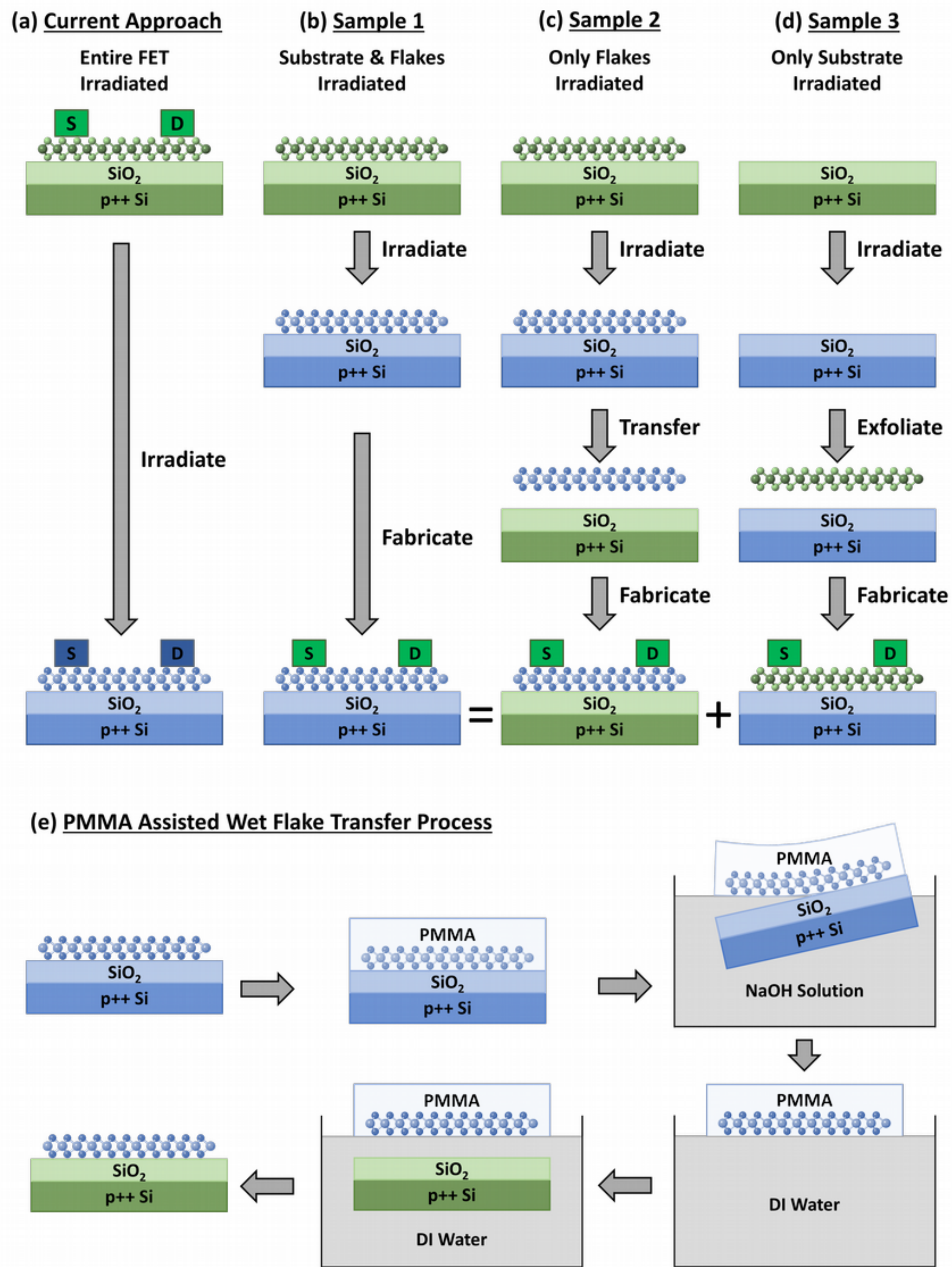

Figure 4.1: Schematic of the device fabrication and irradiation procedure. The irradiated and unirradiated components are painted in blue and green, respectively. (a) In the standard approach the entire FET device is irradiated. (b) The substrate and MoS_2 flakes are irradiated. The contacts are fabricated after the irradiation. (c) The MoS_2 flakes are irradiated and then transferred to a new substrate for device fabrication. (d) The substrate is irradiated and new MoS_2 flakes are exfoliated onto the irradiated substrate for device fabrication. (e) PMMA-assisted wet flake transfer process. The flakes are first coated with PMMA and then removed from the substrate in a NaOH bath. Next, the PMMA and flakes are rinsed in deionized water and transferred to a new substrate. The PMMA is then removed by acetone, leaving the irradiated MoS_2 flakes on the new substrate.

procedure are described in Appendix B.

The irradiation experiment was performed at the Michigan Ion Beam Laboratory, University of Michigan. Protons and He ions were used because they are major components of cosmic radiation and cannot be effectively shielded in space applications. Samples were irradiated by 390-keV singly charged He ions at fluences of 10^{14}, 10^{15}, and 10^{16} ions/cm^2 and 2-MeV protons at a fluence of 1.26×10^{16} ions/cm^2. The 390-keV He ions were produced by a 400-kV ion implanter, and the 2-MeV protons were produced by a 3-MV tandem Pelletron accelerator. The selected ion energies are high enough to penetrate through the MoS_2 FET structure. Although one specific ion energy was used, the total dose can be determined based on the ion stopping power and fluence, and then scaled to the dose in a more complex radiation environment. The samples were uniformly raster-scanned and the current was controlled to keep the sample surface temperature to be less than 75 °C. The control samples (CS) were prepared and fabricated with the same procedure as the irradiated samples and went through the same transport process between the fabrication lab and the irradiation facility. Around 10 control devices were made for each type of sample. At a 390-keV He^+ fluence of 10^{14}, 10^{15}, and 10^{16} ions/cm^2, for all three types of samples (see Figure 4.1(b)-(d)), in total 20, 68, and 50 FET devices were prepared, respectively. At a 2-MeV proton fluence of 1.26×10^{16} ions/cm^2, in total 60 devices were prepared.

4.2.2 Simulation methodology

The classical MD simulations were performed with the LAMMPS code [93] to study the defect structures in monolayer MoS_2 induced by protons and He ions. As shown in Figure 4.2(a), one layer of MoS_2 with 1512 atoms was created in LAMMPS with periodic boundary conditions in the x and y directions and a fixed boundary condition in the z direction. MoS_2 has a hexagonal structure with one layer of Mo atoms sandwiched between two layers of S atoms (see the side view in Figure 4.2(a)).

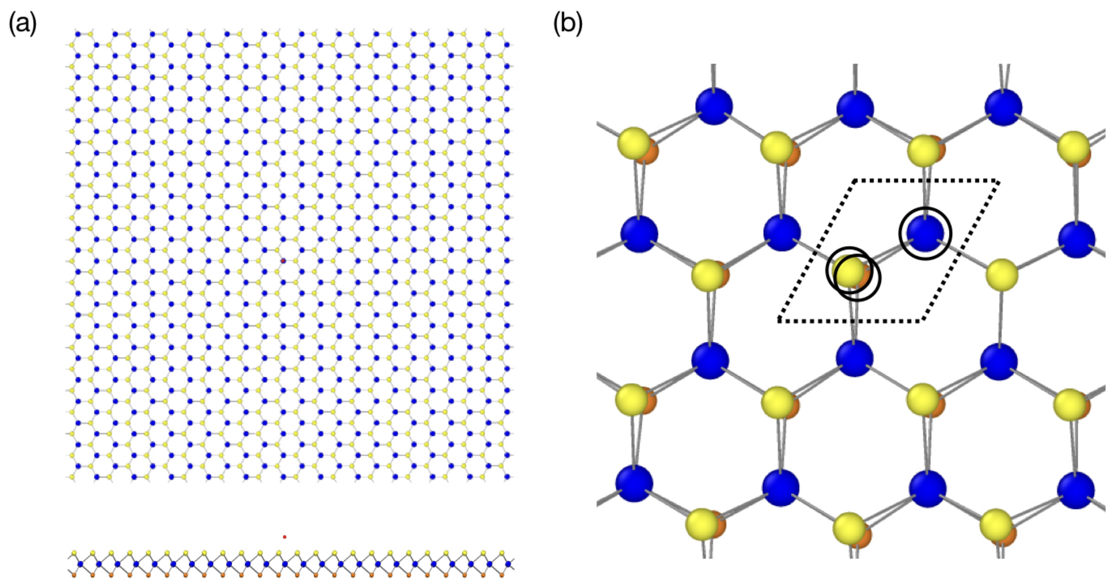

Figure 4.2: (a) Top and side view of the simulated system in the LAMMPS code. The system consists of 1512 MoS_2 atoms and one incident ion (in red). The S atoms in the top and bottom layer are distinguished by yellow and orange color, respectively. The Mo atoms (in blue) are located in the middle layer in the side view. (b) Two ion position sampling schemes were used based on the critical ion impact radius. When the ion energy is low, ion impact positions were uniformly sampled in a MoS_2 unit cell (area contoured by the dashed line). When the ion energy is high, impact positions were uniformly sampled within a circle around the Mo atom and two overlapped circles around the S atoms (areas contoured by the solid line).

The incident atom was initially placed 4.5 nm above the top layer S atoms. The ZBL potential [96] was used to describe the interactions between the incident ion and MoS_2 atoms. Here, only the nuclear repulsive force was considered. There are two main reasons for not considering chemical interactions between the ion and MoS_2 atoms. First, such chemical potential has not been developed and is therefore not available. Second, for high-energy ions, the energy transfer from long-range interactions is small, and it is highly unlikely for the incident ion to stay within MoS_2 to form any chemical bonding due to its high velocity. Thus, for high-energy ions, the chemical interactions have little effect on the collision dynamics and the relaxed structure. For low-energy ions, the total energy transferred could be slightly underestimated without a chemical potential. However, the energy transfer is mostly determined by the nuclear repulsive force described by the ZBL potential and it is a common practice to only use ZBL potential to describe interactions between an incident ion and a 2D material [4, 89, 190]. Although the irradiation experiments were performed with high-energy ions, the evolution of defect generation probability as a function of ion energy is also worth investigating. The simulation results at low ion energies are still useful for understanding the possible collision cascades and their dependence on ion energy.

The reactive empirical bond order (REBO) potential was used to describe the interactions among MoS_2 atoms. The REBO potential uses an empirical formalism based on the bond order between atoms and is able to describe the complex chemistry of a material system [191]. Here, the REBO parameterization developed by Liang *et al.* [192] and Stewart *et al.* [193] was used in which the Lennard-Jones (LJ) potential is also included to describe the van der Waals interactions [192]. It is found that the distance between neighboring Mo atoms or S atoms (the a value of a hexagonal structure) is 0.317 nm, which is close to the experimental result of 0.315 nm [194]. The height between MoS_2 layers (the c value) is found to be 1.297 nm, which is also close to the experimental value of 1.229 nm [194]. High-energy ions can create

cascade collisions within MoS_2, displacing Mo and S atoms far from their equilibrium positions. Since REBO potential is designed for chemical reactions during which the interatomic distance is close to the equilibrium position, the accuracy of short-range interactions cannot be guaranteed. Therefore, the ZBL potential was combined with the REBO potential by a Fermi-like function so that the short interatomic distance is dominated by the ZBL potential and the long interatomic distance is dominated by the REBO potential:

$$
\begin{aligned}
V_{ij} &= (1 - f_F(r_{ij}))V_{ij}^{ZBL} + f_F(r_{ij})V_{ij}^{REBO} + V_{ij}^{LJ}, \\
f_F(r_{ij}) &= \frac{1}{1 + \exp\left[-A_F\left(r_{ij} - r_C\right)\right]}.
\end{aligned}
\tag{4.1}
$$

Here, r_{ij} is the distance between atom i and j. V_{ij}, V_{ij}^{ZBL}, V_{ij}^{REBO}, and V_{ij}^{LJ} are the total, ZBL, REBO and LJ potential, respectively, f_F is a Fermi-like function used to connect the ZBL and REBO potential, and r_C and A_F are parameters used to define the shape of f_F. When r_{ij} is equal to r_C, f_F is equal to 0.5, which means that V_{ij}^{ZBL} and V_{ij}^{REBO} have the same weight of 0.5. Thus, r_C defines the transition distance between the two potentials. A_F describes the sharpness of the transition around the transition point r_C. The A_F and r_C were set to 14 $Å^{-1}$ and 1.2 Å, respectively. An A_F value of 14 $Å^{-1}$ was also used in a prior work when graphene was described by the Tersoff/ZBL potential [69]. A r_C value of 1.2 Å was chosen based on the lattice constant of MoS_2. The connection of the two potentials was achieved by modifications of the LAMMPS potential file. In addition to the change of potential, the interatomic forces were also reformulated due to the incorporation of the Fermi-like function. In order to show the differences between the ZBL, REBO, and combined potential, the energy transfer between an incident Mo/S atom and an immobile Mo/S PKA was simulated at different impact positions with different kinetic energies. The results are shown in Figure 4.3 and Figure C.1 of Appendix C. The REBO potential significantly underestimates the short-range energy transfer, and the

underestimation becomes more pronounced at higher ion energies. When the impact position is smaller than than 1.2 Å, the energy transfer from the combined potential is very close to that of ZBL. When the impact position becomes larger than 1.2 Å, the combined potential starts to approach the REBO potential as expected.

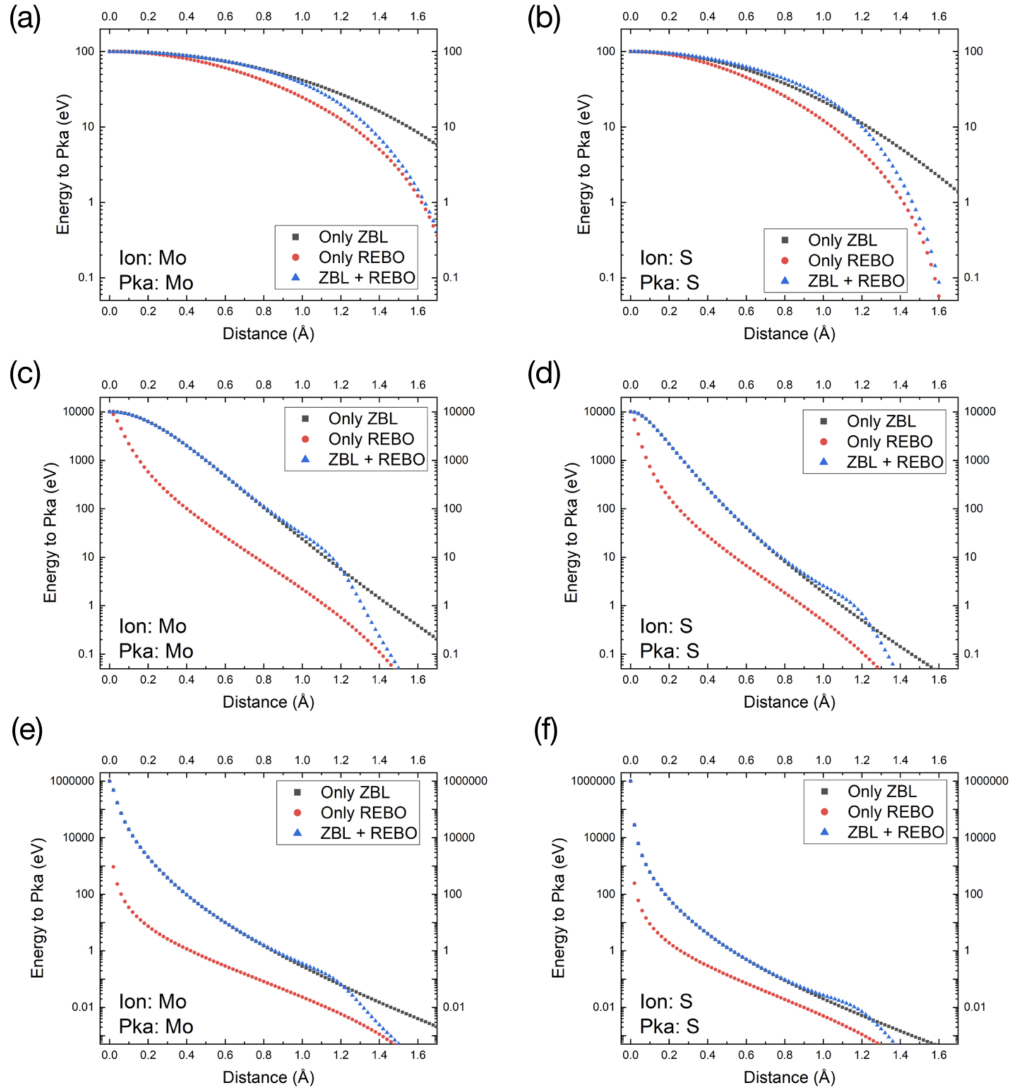

Figure 4.3: Energy transfer between Mo and S atoms as a function of the ion impact position with the ZBL, REBO, and combined ZBL/REBO potential. For a Mo ion incident on a Mo PKA, the energy transfer is shown for an ion kinetic energy of (a) 0.1 keV, (c) 10 keV, and (e) 1000 keV. For a S ion incident on a S PKA, the energy transfer is shown for an ion kinetic energy of (b) 0.1 keV, (d) 10 keV, and (f) 1000 keV.

In order to have an accurate estimation of the defect generation probability, the

formation energies of different types of defects need to be accurate. The defect formation energies from the REBO potential were calculated by the following relationship:

$$E_f = E_{defect} - E_{perfect} \pm \sum_i n_i \mu_i. \tag{4.2}$$

Here, E_f is the defect formation energy, E_{defect} is the system energy with defect, and $E_{perfect}$ is the perfect system energy. n_i and μ_i are the number and chemical potential of the added/removed atom species i, respectively. For an added or removed atom, the chemical potential is subtracted or added, respectively. For a compound material like MoS_2, it is difficult to determine the exact chemical potential with a simulation method that uses empirical potentials. It is only possible to determine a range for chemical potentials and, accordingly, a range for the defect formation energy. For Mo-rich MoS_2, the chemical potential of Mo atoms was determined by the system energy of bulk Mo with body-centered cubic structure. In this case, the chemical potential of S atoms was calculated by:

$$\mu_{S,Mo-rich} = \frac{1}{2}(E_{MoS_2} - \mu_{Mo,Mo-rich}), \tag{4.3}$$

where E_{MoS_2} is the energy of one MoS_2 molecule. For S-rich MoS_2, the chemical potential of S atoms was determined by the system energy of bulk α-S, and the chemical potential of Mo atoms was calculated by:

$$\mu_{Mo,S-rich} = E_{MoS_2} - 2\mu_{S,S-rich}. \tag{4.4}$$

Based on Figure 4.4, it is shown that the formation energies of most of the defect structures show good agreement with the results of first-principles calculations except for V_{MoS3} vacancy and $S2_{Mo}$ antisite, where REBO overestimates the formation energies. The most common defects from the simulations are sulfur SV (V_S), sulfur DV

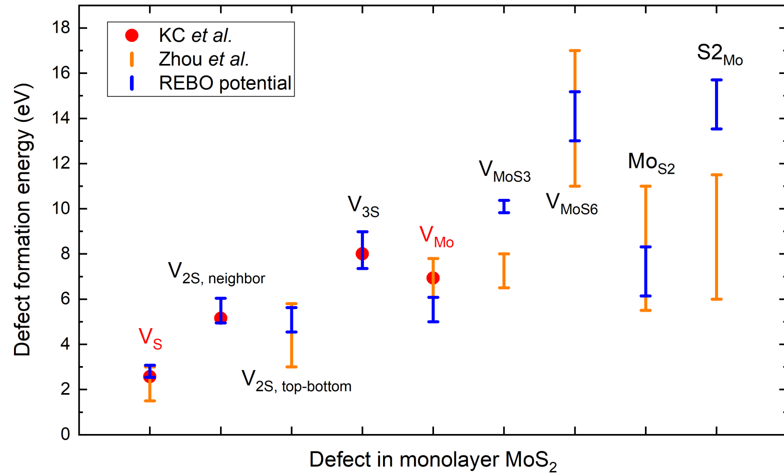

Figure 4.4: MoS_2 defect formation energies with the REBO potential. V_S and V_{Mo} represent single S and Mo vacancy, respectively. $V_{2S,\ neighbor}$ corresponds to two missing neighbor S atoms at the same layer. $V_{2S,\ top\text{-}bottom}$ corresponds to a S vacancy at the bottom of another top S vacancy. V_{3S} corresponds to three S vacancies at the same layer next to the same Mo atom. V_{MoS3} is a V_{3S} plus a Mo vacancy in the center. V_{MoS6} is a vacancy cluster with one Mo atom and six neighboring S atoms. Mo_{S2} corresponds to a Mo antisite occupying a $V_{2S,\ top\text{-}bottom}$ site. $S2_{Mo}$ corresponds to two S atoms occupying a Mo site. The defect formation energies based on first-principles calculations from KC *et al.* [2] and Zhou *et al.* [3] are also shown.

($V_{2S, neighbor}$ and $V_{2S, top-bottom}$), and molybdenum SV (V_{Mo}). The formation energies of these defects are close to the reported values. According to the REBO potential, the V_S formation energy is within a range of 2.5 eV to 3.1 eV and the V_{Mo} formation energy is within a range of 5.0 eV to 6.1 eV. This is consistent with the result from previous studies showing that it is easier to form S vacancy than Mo vacancy [4, 46]. The good agreement on the defect formation energies validates the use of REBO potential for studying ion damage of MoS_2.

After the geometry and potentials were defined, the energy of the simulated system was minimized and the system was relaxed for 2.5 ps with a timestep of 1.0 fs at 300 K with NVT ensemble. After the relaxation, the next step was to simulate ion irradiation at normal incidence from different ion impact positions. The impact position of the incident ion relative to the PKA is defined as its projected position in the MoS_2 PKA plane following the direction of its initial velocity. Before the irradiation process, the *x*- and *y*-coordinate of the incident atom (hydrogen or He atom) were re-positioned according to the position sampling scheme used. When the ion energy is low, the ion initial position was uniformly sampled within a unit cell area (see Figure 4.2(b)). When the ion energy is high, the defect cross section is small and it becomes inefficient to sample the entire unit cell area. Therefore, only a small area around the PKA atom was sampled. For a Mo PKA, ion impact positions were uniformly sampled within a radius that is a constant at a fixed ion energy. For a S PKA, since there are two S atoms along the direction of the ion, ion positions were sampled within two overlapped circles centered at each S atom (see Figure 4.2(b)). These two circles do not completely coincide due to the thermal motion of atoms at 300 K. Impact positions cannot be simply sampled within a radius around the top S atom because this will ignore ion positions that can lead to ejections of the bottom S atoms and create bias to the defect generation probability. In order to uniformly sample positions within two overlapped circles, a Monte Carlo rejection scheme was

used. For both proton and He ions, for a kinetic energy lower than 1 keV, the first sampling scheme was used in which the entire unit cell area was sampled. At this low energy, defects can be generated at a large impact position and therefore, impact positions cannot be confined to a small area around the PKA atoms. For a kinetic energy equal to or larger than 1 keV, the second sampling scheme was used in which the sampling area was confined to a small area and was adjusted for each ion species and ion energy.

Next, the ion was given an initial velocity and the irradiation process was simulated with the NVE ensemble with an adaptive timestep until no more collision could take place and sputtered atoms all left the simulation box. For all the atoms in the simulation box, the energy loss per step was set to be less than 2 eV, and the displacement per step was set to be less than 0.01 Å. The minimum and maximum timestep were set to 2×10^{-7} fs and 10^{-1} fs, respectively. For example, if the timestep for an energy loss of 2 eV is less than the minimum timestep, the simulation will use the minimum timestep of 2×10^{-7} fs. All the parameters used in the adaptive timestep scheme were extensively tested to ensure that the energy transfer process is accurate, especially during the collision process.

After the ion irradiation, the system was relaxed with NVT ensemble at 300 K for 8 ps with a timestep of 0.5 fs. In order to identify the structural change, the system energy was minimized again and Voronoi tessellation was computed in LAMMPS to identify the interstitials and vacancies. The number of sputtered S and Mo atoms were also obtained from the LAMMPS output. For proton irradiation, the ion energy was simulated from 0.05 keV to 2000 keV. For He ion irradiation, the ion energy was simulated from 0.01 keV to 2000 keV, including the experimental condition of 390 keV. For an ion energy equal to or larger than 1 keV, at least 1000 instances of defects were obtained. For an ion energy less than 1 keV, at least 10,000 impact positions were sampled. In total 300,000 simulations were performed.

4.3 Results and discussion

4.3.1 Helium ion irradiation of MoS_2 field-effect transistors

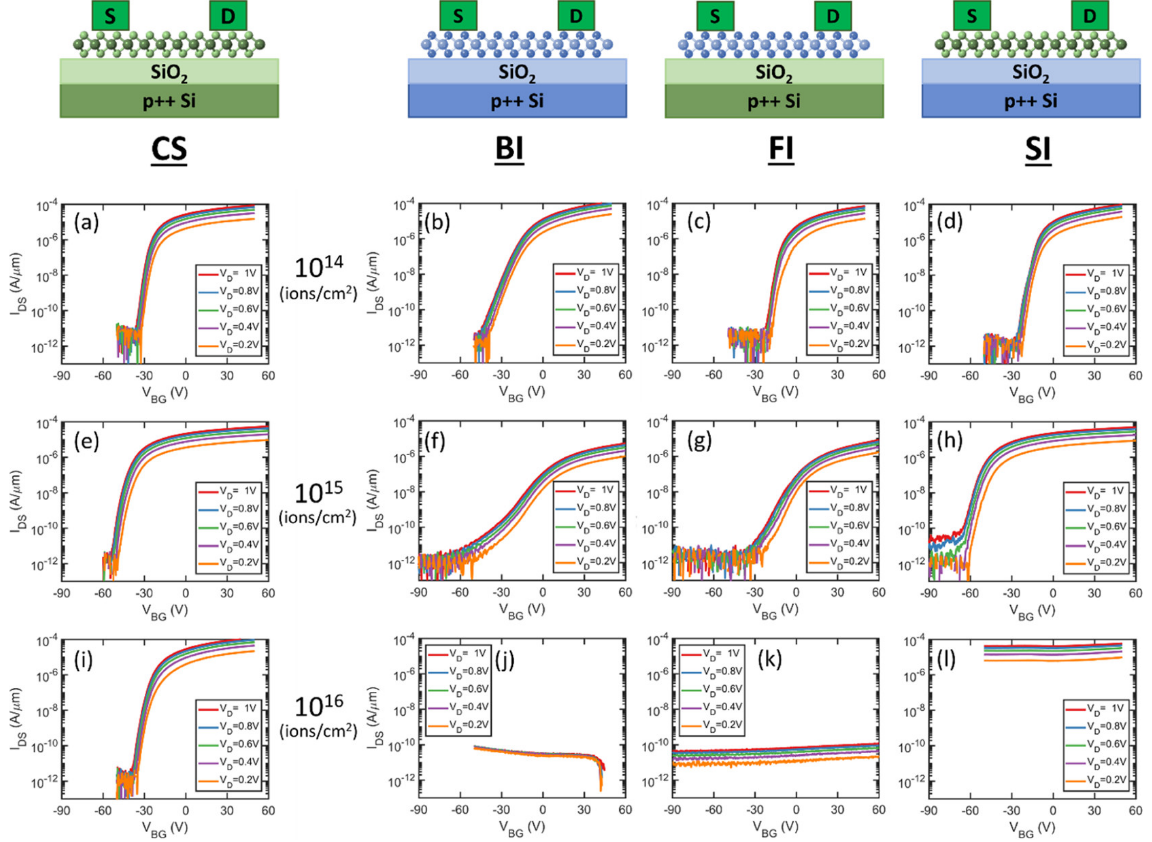

Figure 4.5: Radiation damage due to He^+ exposure. Representative transfer characteristics of MoS_2 FETs from an unirradiated control sample with neither the flakes nor the substrate being irradiated, and post radiation samples with both the flake and the substrate irradiated (BI), only the flake irradiated (FI), and only the substrate irradiated (SI). 390-keV He^+ ions were used at a total fluence of (a)-(d) 10^{14} ions/cm^2, (e)-(h) 10^{15} ions/cm^2, and (i)-(l) 10^{16} ions/cm^2.

Figure 4.5(a)–(d) shows the representative transfer curves for CS, samples with both the MoS_2 flakes and substrate irradiated (BI), samples with only the MoS_2 flakes irradiated (FI), and samples with only the SiO_2 substrate irradiated (SI) for different source and drain voltages (V_{DS}) at a He^+ fluence of 10^{14} ions/cm^2. A transfer curve shows the evolution of the current between source and drain (I_{DS}) at a fixed V_{DS} as a function of the back-gate voltage between gate and source (V_{GS}). For an ideal

transistor, low off-state current, high on-state current, and fast transition between on and off state are expected. In addition, the threshold voltage (V_T) needs to be stable, where V_T is defined as the minimum voltage between source and gate to create a conducting path between source and drain. The capability to turn on/off a transistor efficiently can be described by the SS, which is defined as $SS = \partial V_{GS}/\partial \log I_{DS}$. At a fluence of 10^{14} ions/cm^2, minimum degradation of transfer curves was observed for FI and SI devices. For BI devices, although there is also a minimal change to the on-state current and V_T, a lower current slope (a larger SS) was observed between the on and off region, indicating a higher extent of damage, which can be attributed to the generation of structural defects and interfaces states. However, the change of SS is relatively small and due to the sample-to-sample variation, it is hard to draw convincing conclusions based on this small change. At a He^+ fluence of 10^{15} ions/cm^2, the transfer characteristics for CS, BI, FI, and SI samples are shown in Figure 4.5(e)–(h). A negative shift of V_T was observed in SI samples. For FI and BI samples, there is a significant degradation of SS and on-state current, and a large positive shift in V_T. The increase of SS in FI and BI samples originates from the creation of structural defects within MoS_2 and creation of interface states at the MoS_2/SiO_2 interface. At a He^+ fluence of 10^{16} ions/cm^2, as shown in Figure 4.5(i)–(l), a complete failure of FET operation was observed in all samples. BI and FI devices show extremely low source-drain currents (below 10^{-10} A/µm) over the entire V_{GS} sweep range. The current level is comparable to the leakage current, indicating that the devices cannot conduct any current between the source and drain. For SI devices, since the MoS_2 flakes were not irradiated, the MoS_2 could still conduct current, but the devices lost the gate control due to the significant damage to the oxide. There are two possible reasons for the loss of gate control: Either the oxide is damaged to a point that it cannot change the electric field across the channel layer, or there is a significant amount of positive charge accumulation so that the off-state voltage is outside the

V_{GS} sweep range. In summary, based on the representative transfer curves shown in Figure 4.5, at a fluence of 10^{14} ions/cm^2, 10^{15} ions/cm^2, and 10^{16} ions/cm^2, the degradation induced by 390-keV He$^+$ ions is minimal, intermediate, and catastrophic, respectively. At 10^{16} ions/cm^2, the devices can no longer function properly for all three types of samples.

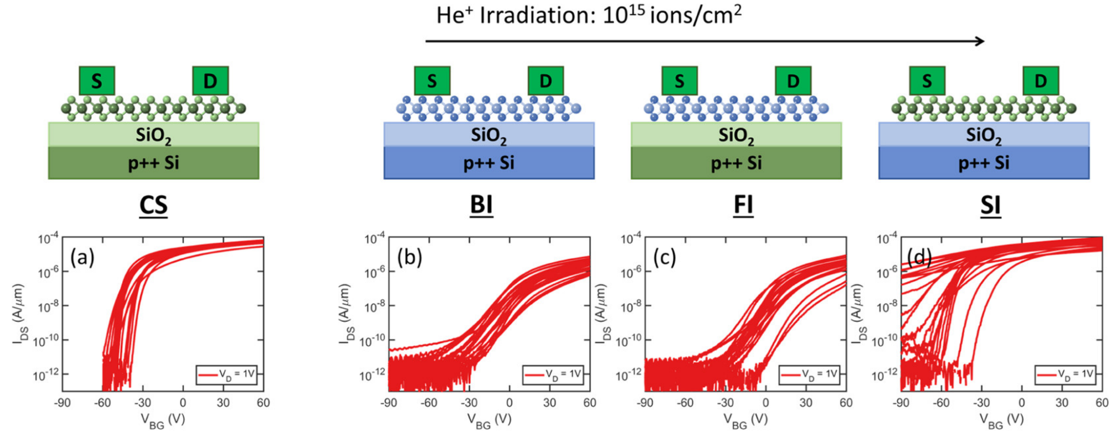

(e) Statistical analysis of irradiation effect on critical device parameters

Sample Configuration	Subthreshold Slope (mV/dec)		Threshold Voltage (V_T)		Mobility (cm^2/V-s)	
	Mean	Std. Dev.	Mean	Std. Dev.	Mean	Std. Dev.
CS: Control Sample	1810	790	-41	4	22.7	3.3
BI: Both Irradiated	10299	1770	12	10	2.4	1.2
FI: Flake Irradiated	8897	1840	16	9	2.2	1.3
SI: Substrate Irradiated	4627	1486	-65	23	19.5	6.2

Figure 4.6: Statistical analysis of He$^+$ irradiation at a fluence of 10^{15} ions/cm^2. Overlaid transfer characteristics of all MoS_2 FETs correspond to (a) control samples (CS), (b) samples with both flakes and substrate irradiated (BI), (c) samples with flakes irradiated (FI), and (d) samples with substrate irradiated (SI) at a fluence of 10^{15} He$^+$ ions/cm^2. (e) Mean and standard deviation of subthreshold slope, threshold voltage, and field effect electron mobility for all four sample configurations.

The electrical characteristics of the fabricated FET devices experienced a certain level of device-to-device variation due to the variation in MoS_2 flake size and thickness. Therefore, in order to obtain statistically significant conclusions, more than 20 devices were fabricated for each type of sample (BI, FI, or SI) at a fluence of 10^{15} ions/cm^2. Figure 4.6(a)–(d) shows the transfer curves of all the devices under each irradiation procedure. Figure 4.6(e) shows the statistical analysis of SS, V_T, and mobility where the charge carrier mobility is determined by the peak transconductance in the transfer

curve. For FET devices, The V_T is influenced by both the positive oxide charges and the interface states, while the SS is only influenced by the interface states [77, 188, 195]. In BI devices, the SS has the highest increase, changing from 1.81 V/dec to 10.3 V/dec. FI devices also have a large SS increase, changing from 1.81 V/dec to 8.9 V/dec. Due to the irradiation of MoS_2, a significant amount of interface states has been created. Based on the relationship between the SS and the density of interface states (D_{IT}), D_{IT} increases by a factor of ∼5 in BI devices [77, 195]. What may at first seem counterintuitive is that the SS also increases from 1.81 V/dec to 4.6 V/dec in SI devices where the MoS_2 was not irradiated. This is actually due to the generation and migration of oxide charges to near-interfacial locations. These near-interfacial oxide charges can form defects known as border traps, which have similar electric behavior to interface traps and therefore lead to the SS increase [196].

With respect to the V_T shift, there is a positive shift from −41 V to 16 V in FI devices due to the generation of negative interface states from n-type doped MoS_2. There is a negative shift from −41 V to −65 V in SI devices due to the generation of positive oxide charges. Although all of these effects are expected, there is a large variation of the transfer curves in SI devices. The fact that similar large variation is also seen for proton-irradiated SI samples (see Figure 4.7(d)) indicates that this is not due to an human error in sample preparation. However, this large variation is not seen in BI devices where the substrate was also irradiated. If this is due to the sample heating during the lithography process, the same behavior is also expected in BI samples. The atomic force microscope measurement on flake thickness shows that the magnitude of the V_T shift depends weakly on the number of MoS_2 layers. In addition, ion beam was defocused and raster-scanned over the entire substrate, and therefore, any spatial non-uniformity of the radiation dose is not expected. This is also supported by the fact that the spatial distribution of devices with extreme low V_T on the substrate surface is random. All these facts make it difficult to explain the

large statistical variation of transfer curves and further investigation is required. A comprehensive discussion of this issue can be found in our publication [77]. For BI samples, the V_T shift is a combined effect from positive oxide charges and negative interface states. Since V_T experiences a positive shift from -41 V to 12 V, the density of negative interface states dominates over the positive oxide charges.

The mobility drops from 22.7 $cm^2/V{\cdot}s$ to 2.4 $cm^2/V{\cdot}s$ and 2.2 $cm^2/V{\cdot}s$ for BI and FI devices, respectively. The decrease in mobility by an order of magnitude is induced by the formation of scattering sites at the channeling layer. The scattering sites are mainly caused by structural defects from elastic collisions between He ions and MoS_2 atoms. Elastic collisions can create vacancies, FPs, and more complicated structural disorder [74]. Sulfur vacancies are the most probable defects due to its lower displacement energy according to prior simulation results [4], which is also confirmed by our simulations, as discussed later in this chapter. Although ionization usually does not lead to structural defects in semiconductor materials, it was also reported that ionization can break the interplanar bonds in the 2D material and form defects [156]. Nevertheless, at such a high fluence, the FET devices still exhibit good high-state current and high on/off ratio (above 10^6), showing the good radiation resilience of MoS_2 FETs. For SI devices, the decrease in mobility is statistically insignificant. This shows that the degradation of mobility is not due to damage of the oxide, but the damage of MoS_2. In the studies of traditional MOSFETs, it has been shown that hydrogen ions (protons) can be released from SiO_2 and act as holes [181]. These holes hop through the oxide and get trapped at trapping centers [181], which originate from oxygen vacancies at the interface [172]. Although interface states can be generated from the oxide side, they have minimal contribution to the decrease in mobility.

4.3.2 Proton irradiation of MoS_2 field-effect transistors

Samples were irradiated with 2-MeV protons at a fluence of 1.26×10^{16} ions/cm^2. This proton fluence was chosen to match the same dose (total energy absorbed per mass) of 390-keV He ions at a fluence of 10^{15} ions/cm^2. Since the ratios of stopping powers in MoS_2, SiO_2, and Si are approximately the same for each irradiation condition, the dose in each material (MoS_2, SiO_2, and Si) is also about the same between the two irradiation conditions. However, the fraction of energy channeled into nuclear stopping power is lower for protons, and they also have a longer penetration depth. The ion stopping powers and the ion range in Si are shown in Table 4.1. The overlaid transfer curves are shown in Figure 4.7(a)–(d) with the statistical analysis of V_T, SS, and mobility presented in Figure 4.7(e).

Table 4.1: Stopping powers and ranges of protons and He ions in the irradiated materials estimated from SRIM/TRIM [1]. A displacement threshold energy of 31.7 eV and 5.0 eV were used for Mo and S atoms, respectively [4].

	$(dE/dx)_{elec.}$ in MoS_2 (eV/Å)	$(dE/dx)_{nucl.}$ in MoS_2 (eV/Å)	$(dE/dx)_{elec.}$ in SiO_2 (eV/Å)	$(dE/dx)_{nucl.}$ in SiO_2 (eV/Å)	Range in Si (µm)
390 keV He^+ ion	53.9	3.37×10^{-2}	38.7	2.09×10^{-2}	1.66
2 MeV proton	4.30	5.45×10^{-4}	3.29	3.86×10^{-4}	47.7

For BI and FI devices, the SS increases from 1.81 V/dec to 6.0 V/dec and 4.7 V/dec, respectively. Compared with a SS of 10.3 V/dec and 8.9 V/dec in BI and FI devices under He^+ irradiation of the same dose, the extent of SS increase in proton-irradiated devices is lower. This difference is due to the fact that protons have a lower ratio of nuclear stopping power to electronic stopping power. Lower probability of elastic collisions with sample atoms leads to a lower D_{IT}, which explains the lower increase in the SS. For SI devices, the SS increases from 1.81 V/dec to 5.6 V/dec. As with the devices exposed to He^+ irradiation, there is a large variation

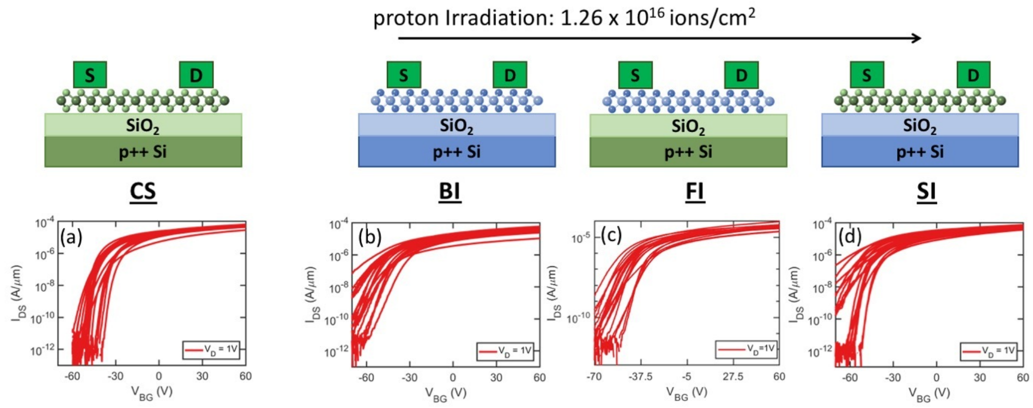

(e) Statistical analysis of irradiation effect on critical device parameters

Sample Configuration	Subthreshold Slope (mV/dec)		Threshold Voltage (V_T)		Mobility (cm^2/V-s)	
	Mean	Std. Dev.	Mean	Std. Dev.	Mean	Std. Dev.
CS: Control Sample	1810	790	-41	4	22.7	3.3
BI: Both Irradiated	6017	2410	-51	8	18.3	3.1
FI: Flake Irradiated	4667	1025	-46	7	19.2	6.4
SI: Substrate Irradiated	5638	4087	-52	7	22.1	3.8

Figure 4.7: Statistical analysis of proton irradiation. Overlaid transfer characteristics of all MoS_2 FETs correspond to (a) control samples (CS), (b) samples with both flakes and substrate irradiated (BI), (c) samples with flakes irradiated (FI), and (d) samples with substrate irradiated (SI) at a fluence of 1.26×10^{16} protons/cm^2. (e) Mean and standard deviation of subthreshold slope, threshold voltage, and field effect electron mobility for all four sample configurations.

in transfer curves, where approximately half of the devices exhibit very low SS and large negative V_T shift. The V_T shifts from -41 V in CS to -51 V, -46 V, and -52 V in BI, FI, and SI devices, respectively. The extent of V_T shift in FI samples is statistically insignificant, showing that the D_{IT} is much lower than that produced by He^+ ions, which is also confirmed by the lower SS increase. However, the SS increase is statistically significant whereas the shift of V_T is not. It could be due to the different dependence of SS and V_T on the nature of interface states. The shift of V_T depends on the net charge of the interface states while the SS increase depends on the impact of interface states on the transport properties of charge carriers. For BI devices, the negative shift of V_T can be explained by the dominance of positive oxide charges over the interface states. It is noted that although the dose is about the same between proton and He^+ irradiation, 2-MeV protons have a higher charge yield (the fraction of electron-hole pairs that escape the initial recombination) than 390-keV He^+ ions, leading to a greater number of holes generated in the oxide layer [197]. Due to the higher density of oxide charges and smaller D_{IT}, a negative V_T shift is expected in BI devices. As the charge yield is higher for protons, a more negative shift of V_T is expected in SI devices compared with that of He^+ irradiation. It is not seen here due to the large variation of the transfer curves. For V_T that is lower than -90 V (beyond the sweep range), a V_T of -90 V was used. This could also lead to a bias to the actual V_T value.

The change of mobility of SI devices is minimal because the MoS_2 flakes were not irradiated. For BI and FI devices, the mobility changes from 22.7 $cm^2/V{\cdot}s$ to 18.3 $cm^2/V{\cdot}s$ and 19.2 $cm^2/V{\cdot}s$ for BI and FI devices, respectively. The changes are much smaller than those observed in He^+ irradiation. This is also due to the smaller D_{IT} and structural defects produced from protons. By comparing the two experiments of the same dose but different nuclear stopping, it is shown that mobility is largely related to the physical defects produced within the MoS_2. The larger

decrease in mobility along with the larger increase in the SS in He-irradiated devices indicates that structural defects have a significant contribution to the generation of interface states. The relative extent of V_T shift also follows the expected behavior. Although the interface charge density and oxide charge density cannot be precisely determined from our electric measurements, the effects from these two factors can be decoupled from different sets of samples. Again, further investigation is required to fully understand the large variation of transfer curves in SI devices.

4.3.3 Defect structures and generation probabilities from classical MD simulations

4.3.3.1 Defect generation from helium ion irradiation

SYs of Mo atoms, S atoms, top layer S atoms, and bottom layer S atoms as a function of the He ion energy are shown in Figure 4.8(a). Since it is possible to eject multiple atoms from the same ion and SY does not take into account the defects without atom being sputtered, the probability of defective sites per incident ion is also shown in Figure 4.8(b). The lowest He energies for the sputtering of Mo and S atoms are 0.8 keV and 0.1 keV, respectively. The actual onset of sputtering could be slightly lower due to the discrete ion energies used. S atoms have an atomic mass of 32.1 amu, which is lower than that of Mo atoms (96.0 amu), and therefore, the energy transferred to a S atom is higher than that of Mo atom at the same impact position. For example, for a head-on collision, the maximum fractions of energy transferred to Mo and S atoms are approximately 15.4 % and 39.4 %, respectively. In addition, S vacancy has a lower formation energy and, accordingly, a lower threshold displacement energy. Due to these two reasons, sputtering of S atoms initiates at a lower energy. The SY of Mo atoms first increases with ion energy and then decreases smoothly from 1 keV to 2000 keV. Below 1 keV, the increase in the ion energy is the dominant reason for the increase in the SY. Above 1 keV, the decrease of the SY

with the ion energy is due to the fact that the energy transferred to the PKA from the same impact position becomes lower due to the shorter interaction time between the ion and the PKA atom. The same trend was observed for proton irradiation of graphene as well, as shown in Chapter II. Compared with Mo atoms, the SY of S atoms does not exhibit a smooth increase below 0.5 keV. First, this is not due to statistical fluctuations because an increase in the number of sample points within this energy range does not change the shape of the trend. When the SYs of the top and the bottom layer S atoms are examined individually, it is shown that the trend in each S layer does not exhibit a smooth evolution either for a He ion energy below 0.5 keV. For example, there is a plateau between 0.05 keV and 0.5 keV for top S atoms and there is a dip at 0.167 keV for bottom S atoms. In addition, the ratio of the SYs from the two layers varies with the ion energy. The SY of bottom S atoms is higher than that of top S atoms between 0.1 keV and 1 keV, and the opposite is the case between 10 keV and 100 keV. At an energy higher than 100 keV, the SYs from the two S layers start to converge. These results show that although one layer of MoS_2 is studied here, the possible collision sequences from the three layers of atoms and their occurrence probabilities depend heavily on the ion energy. The ion energy combined with the impact position determines the possible scattering angles for both the PKA and the incident ion, which further determine the possible defects that could be formed. Different collision sequences have different dependence on the ion energy. Therefore, a smooth evolution of the SY is actually not expected. When the magnitudes of the SY between Mo and S atoms are compared, the SY of S atoms is about one order of magnitude higher than that of Mo atoms. This indicates that after He ion irradiation, there are more S vacancies than Mo vacancies and the irradiated MoS_2 becomes deficient in S atoms.

To better understand the evolution of SYs, SYs are decoupled to two components: sputtering induced by a first collision with a Mo atom and sputtering induced by a

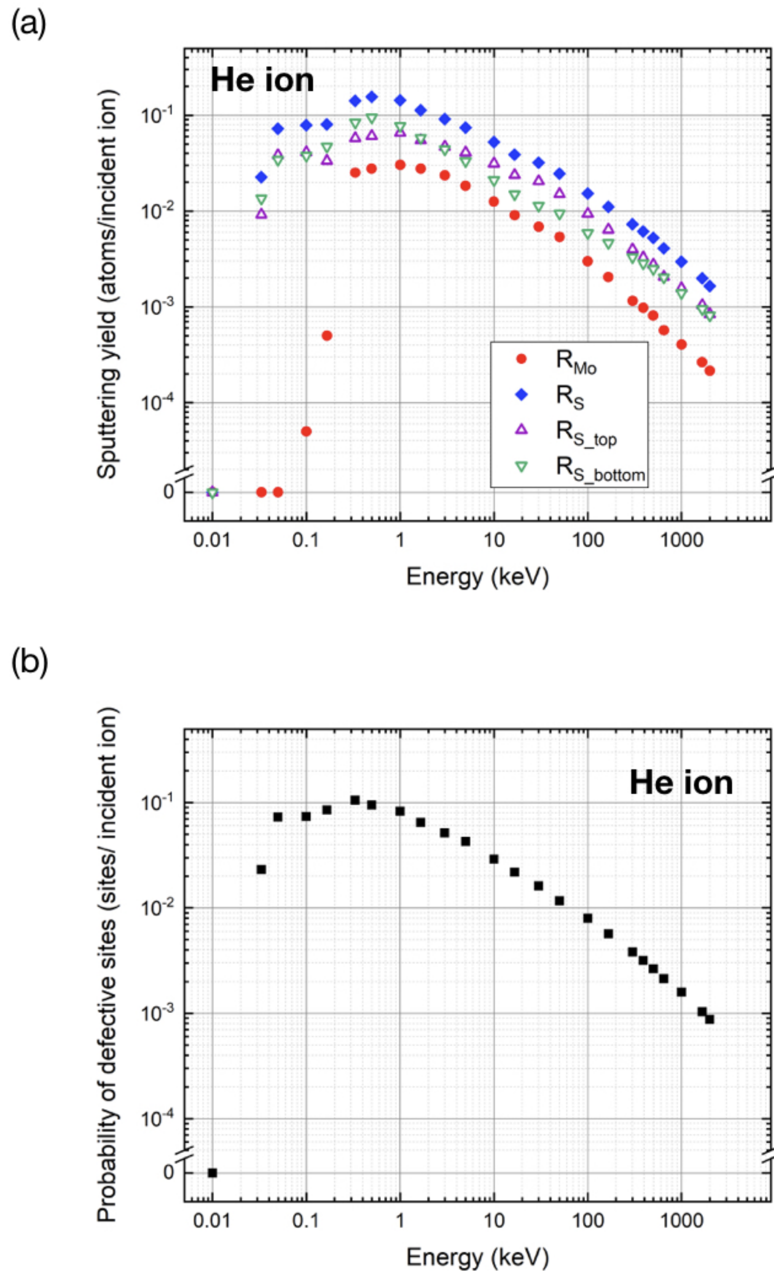

Figure 4.8: (a) Sputtering yields of Mo and S atoms per incident He ion as a function of the He ion energy. The sputtering yields of S atoms in the top and bottom layer of a monolayer MoS_2 are labeled with R_{S_top} and R_{S_bottom}, respectively. (b) Probability of defective sites per incident He ion as a function of the He ion energy.

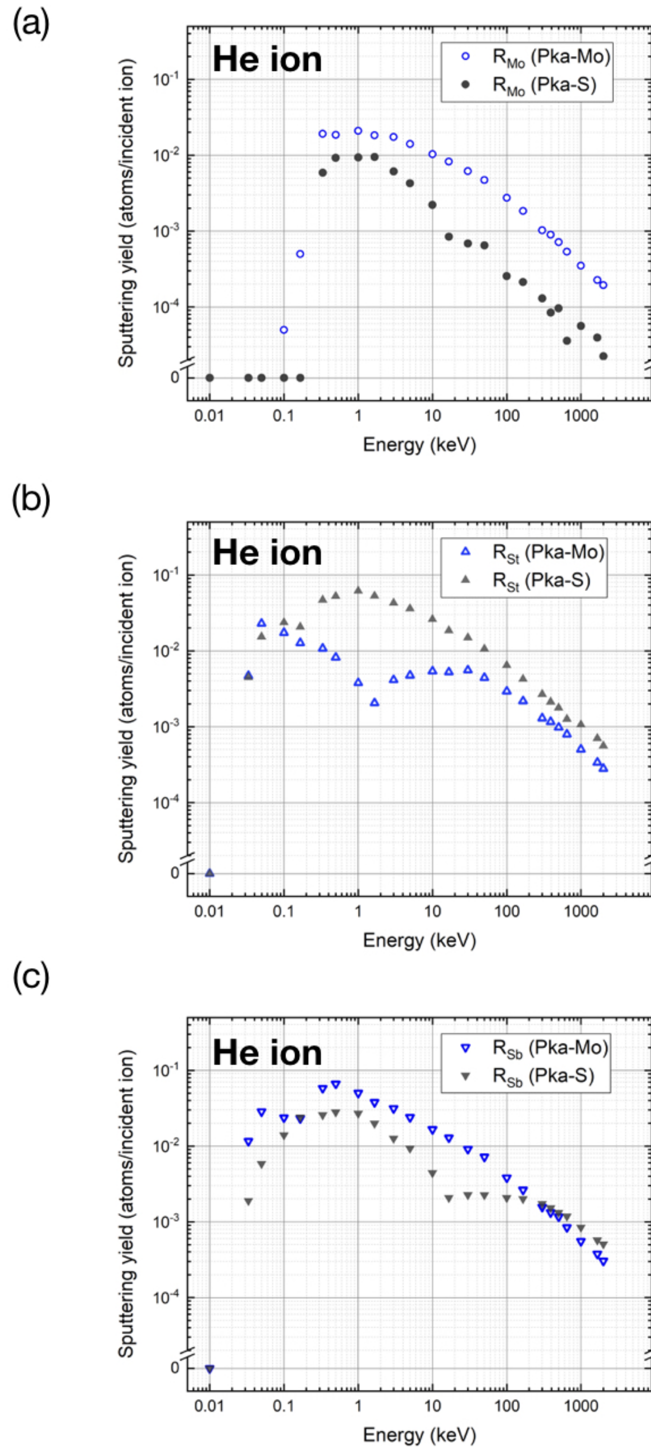

Figure 4.9: Sputtering yields of (a) Mo atoms, (b) top layer S atoms, and (c) bottom layer S atoms are classified by the atom species of the PKA.

first collision with a S atom. SYs of Mo atoms, top S atoms and bottom S atoms induced by a Mo PKA and S PKA are shown in Figure 4.9. For Mo sputtering, the SY is dominated by a first collision with a Mo atom because the ejection of Mo PKA is the dominant sputtering mechanism. It is possible to have Mo ejections from cascade collisions following the ejection of a S PKA, but it has a lower probability. Regarding the sputtering of S atoms, it is shown that the S SY induced by a Mo PKA can have a comparable probability to that induced by a S PKA. There are two reasons for this behavior. First, S atoms have a lower displacement energy and can be easily displaced by an ejected Mo atom. Second, Mo atoms are located in the middle layer of this tri-layer system. Therefore, during the ejection of a Mo atom, it can easily collide with S atoms along its path. In Figure 4.9(b) and (c), the SY curves all have a double-peak structure, indicating that various types of collision cascades have different dependence on the ion energy. This explains the evolution of the aggregated SY curves shown in Figure 4.8(a) and the probability of defective sites shown in Figure 4.8(b).

Figure 4.10 shows the two-dimensional color map of defect size as a function of the number of sputtered Mo and S atoms of each defect at different He ion energies. The distributions of defect size at other He energies can be found in Figure C.2 in Appendix C. With increasing ion energy, it is shown that a wider range of defect sizes can be produced with the possibility of producing defects with larger size. However, the defect structures are still dominated by small point defects. The defect generation probability decreases with the size of the defects. Single-S vacancy is the most probable defect structure at all simulated energies. Local disorder without sputtering and double-S vacancies also have a high generation probability. Within an energy range of 0.33 keV to 10 keV, defect structures with one Mo vacancy along with one to three S vacancies are also quite probable. It is also shown that it is more likely to form defects with the ratio of sputtered S atoms to sputtered Mo atoms to be larger

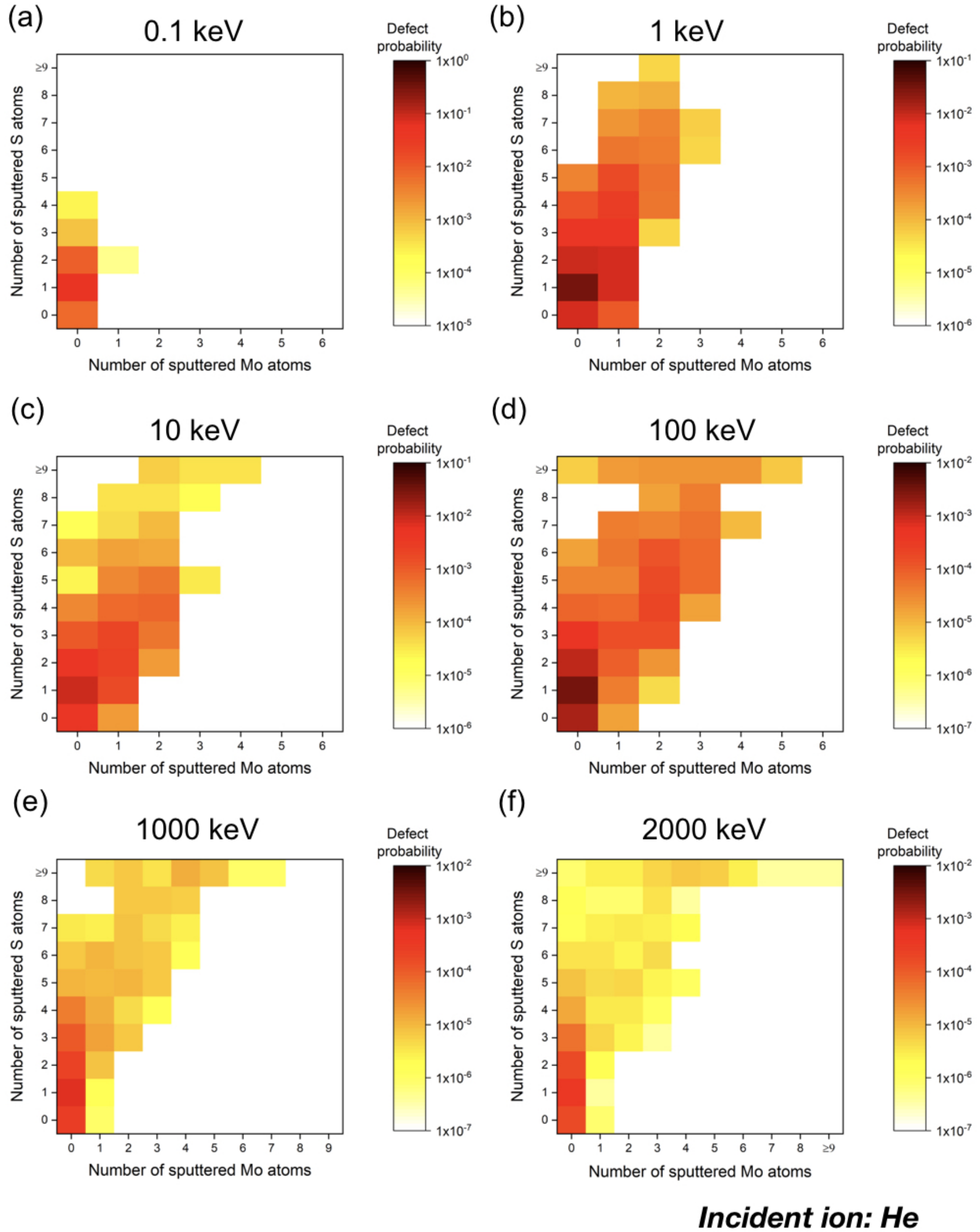

Figure 4.10: Probability of defect size as a function of the number of sputtered Mo (X-axis) and S atoms (Y-axis) for a He energy of (a) 0.1 keV, (b) 1 keV, (c) 10 keV, (d) 100 keV, (e) 1000 keV, and (f) 2000 keV. The probability of zero sputtered Mo and S atom corresponds to the probability of structural disorder without atom being ejected. The scale for the color map is 1×10^{-5} to 1 in (a), 1×10^{-6} to 1×10^{-1} in (b) and (c), and 1×10^{-7} to 1×10^{-2} in (d)–(f).

than 2:1, indicating that defects tend to be S-deficient. This is also consistent with prior experimental results with 30-keV He ions [54].

In the experiment with 390-keV He ions, the SYs for Mo and S atoms are found to be 9.8×10^{-4} and 6.1×10^{-3}, respectively. For a fluence of 10^{15} ions/cm^2, the sputtering fractions of Mo and S atoms are 8.4×10^{-4} and 2.6×10^{-3}, respectively. The density of defective sites is 2.7×10^{-3} per MoS_2 (per one Mo and two S atoms). The magnitude of defect occurrence probability and the distribution of defect structures at different ion energies and fluence levels can be determined from the simulations in a similar manner, which is useful for understanding the physical damage occurring within the MoS_2. An interesting future direction is to study the effect of the number of MoS_2 layers on the defect generation probability since the MoS_2 flakes used in the FETs range from monolayer to several layers. In addition, it would be interesting to study how these defects could impact the transport of charge carriers within MoS_2.

4.3.3.2 Defect generation from proton irradiation

For proton irradiation, the SYs and probability of defective sites are shown in Figure 4.11. The onset of Mo sputtering is between 0.5 keV and 0.8 keV, and the onset of S sputtering is between 0.05 keV and 0.1 keV. As with the SY of He ions, the trend of SY of S atoms at low energy is not smooth. There is a plateau between 0.2 keV and 0.5 keV and a dip at 3 keV. More sampling positions at these energies were chosen, but there is little change in SY values, which indicates that it is not due to the insufficient sampling points. The SYs of top layer and bottom layer S atoms also exhibit complicated evolution with proton energy and the ratio of top layer S atoms to bottom layer S atoms depends greatly on the proton energy. For the SY of Mo atoms, there is a plateau region between 1 keV and 5 keV followed by a smooth decrease after 5 keV. Regarding the probability of defective sties, there is a sharp increase from 0.05 keV to 0.2 keV, a plateau between 0.2 keV to 0.8 keV, another

increase from 0.8 keV to 3 keV, and a gradual decrease from 3 keV to 2000 keV. The SY for each type of atoms is also classified by the PKA atom species, as shown in Figure 4.12. The trends are also convoluted, indicating that different types of collision sequences can take place and have different dependence on the proton energy.

Figure 4.13 shows the color map of defect size as a function of the number of sputtered Mo and S atoms at different proton energies (see Appendix C, Figure C.3 for results at other proton energies). Compared with He ions at the same energy, the defect size tends to be smaller. With the increase of proton energy, more defect structures can be generated with the possibility of ejecting more atoms. As with He ions, the most probable defect still corresponds to defect structures with one sputtered S atom. It is noted that in the simulations, the defect accumulation is not considered and only independent ion irradiation of perfect MoS_2 structure is studied. At our experimental condition of 2000 keV, for a fluence of 1.26×10^{16} ions/cm^2, the sputtering fractions of Mo and S atoms are 1.4×10^{-4} and 5.5×10^{-4}, respectively. The density of defective sites is 6.8×10^{-4} per MoS_2 (per one Mo and two S atoms). Since the sputtering ratio of S to M atom is 4.1, the irradiated MoS_2 becomes S-deficient. The sputtered Mo and S atoms are 16% and 21% of that of 390-keV He ions at 10^{15} ions/cm^2. The density of defective sites is 25% of that of He ions at 10^{15} ions/cm^2. This is consistent with the FET irradiation results that less structural damage occurred within proton-irradiated MoS_2.

4.4 Summary

By irradiating individual MoS_2 FET components, the effects of irradiation on SiO_2 substrate and MoS_2 flakes were decoupled. The impact of oxide charges and interface states on the SS increase, mobility decrease and threshold shift was clearly illustrated with the new experimental approach. By irradiating FETs with He ions and protons of the same dose, it was shown that nuclear stopping power plays an important role

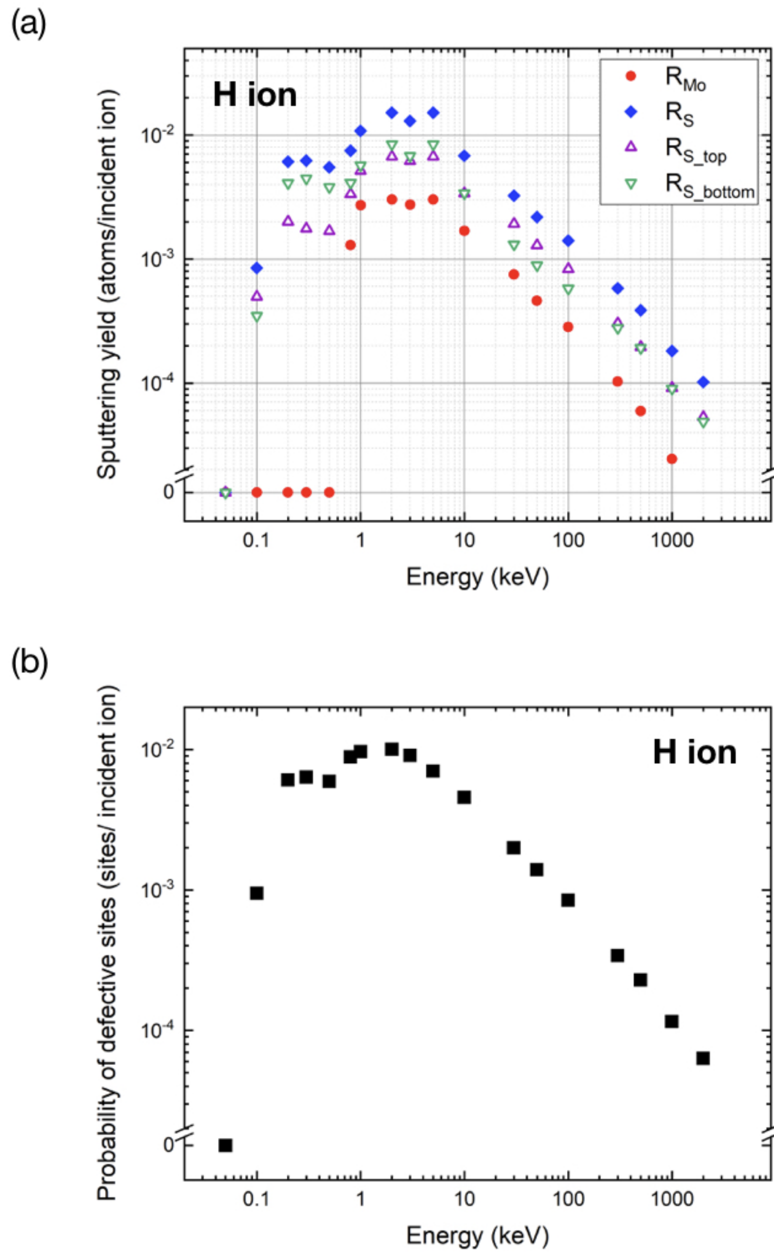

Figure 4.11: (a) Sputtering yields of Mo and S atoms per incident proton as a function of the proton energy. The sputtering yields of S atoms in the top and bottom layer of a monolayer MoS_2 are labeled with R_{S_top} and R_{S_bottom}, respectively. (b) Probability of defective sites per incident proton as a function of the proton energy.

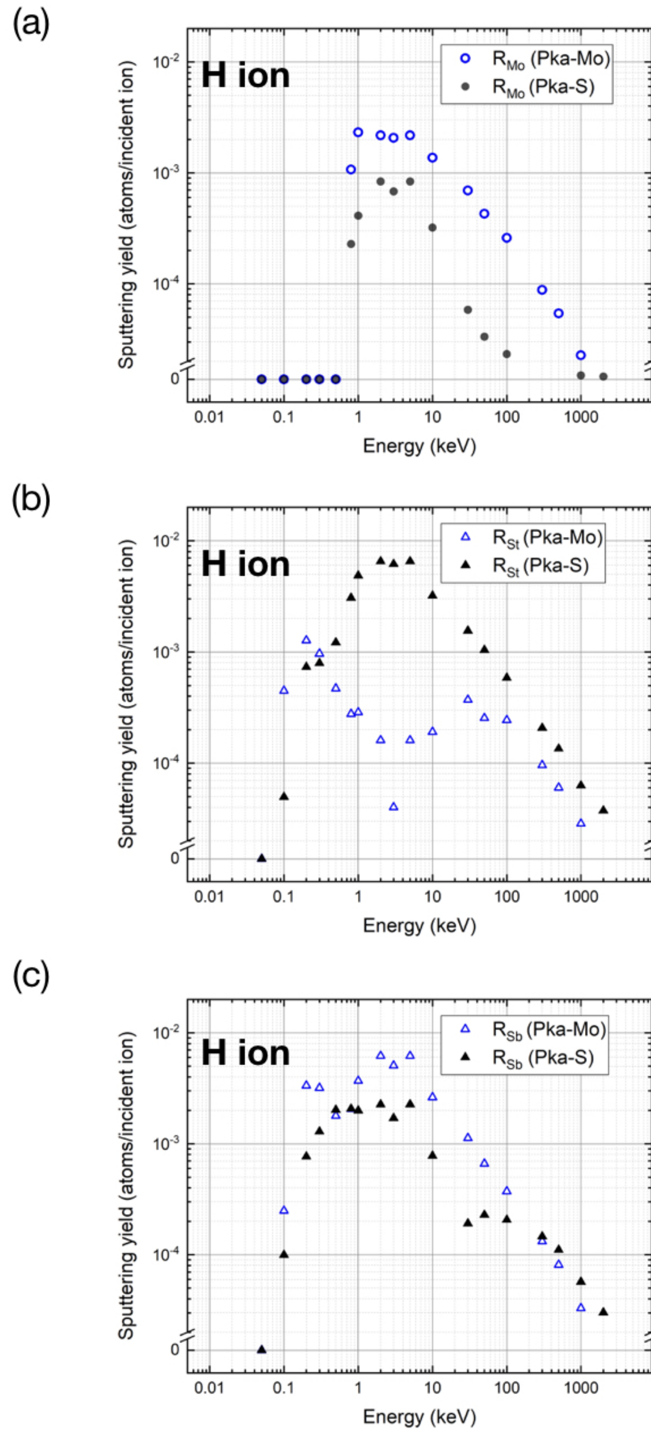

Figure 4.12: Sputtering yields of (a) Mo atoms, (b) top layer S atoms, and (c) bottom layer S atoms are classified by the atom species of the PKA.

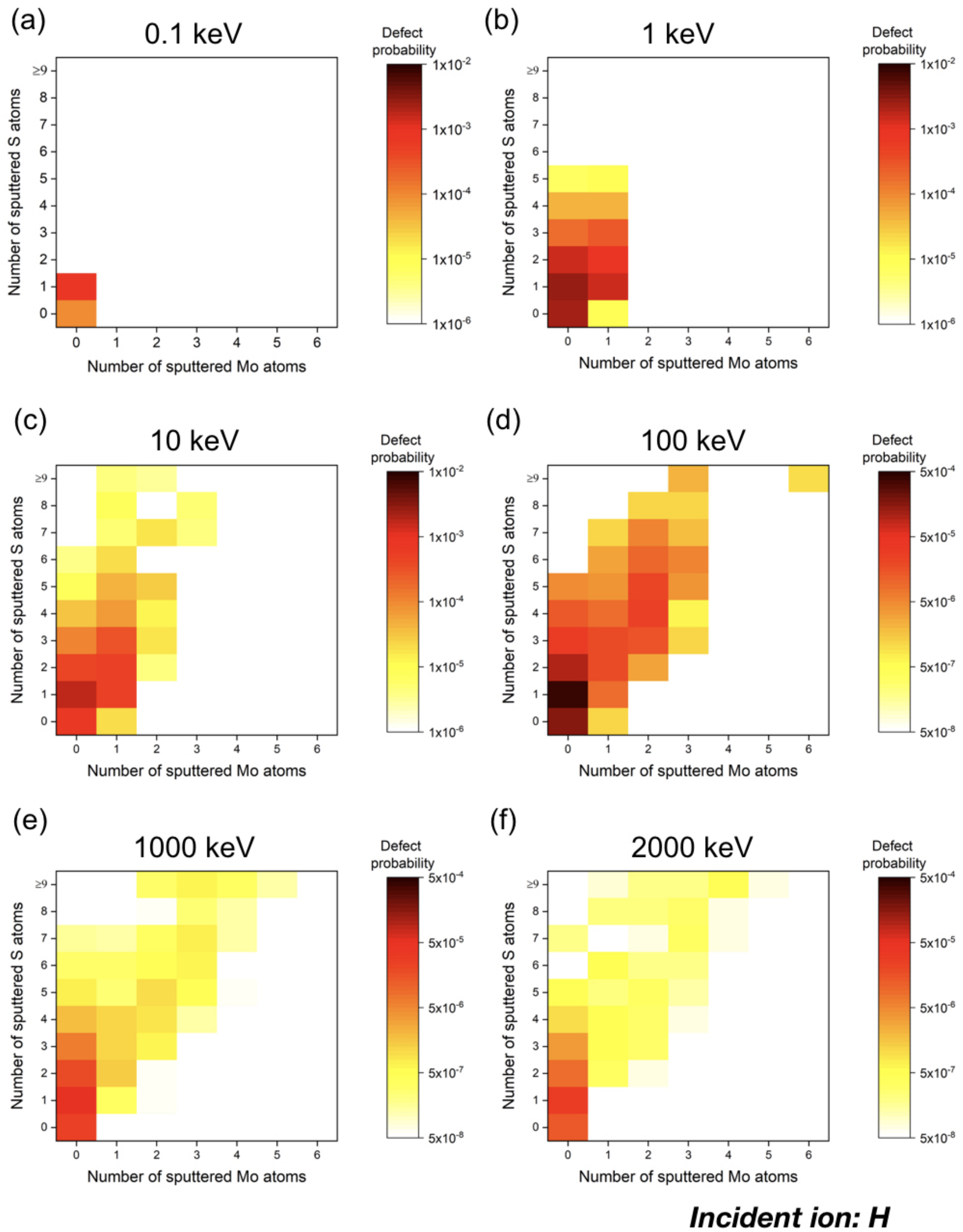

Figure 4.13: Probability of defect size as a function of the number of sputtered Mo (X-axis) and S atoms (Y-axis) for a proton energy of (a) 0.1 keV, (b) 1 keV, (c) 10 keV, (d) 100 keV, (e) 1000 keV, and (f) 2000 keV. The probability of zero sputtered Mo and S atom corresponds to the probability of structural disorder without atom being ejected. The scale for the color map is 1×10^{-6} to 1×10^{-2} in (a)–(c) and 5×10^{-8} to 5×10^{-4} in (d)–(f).

in the generation of physical defects and interface states, resulting in the degradation of SS and mobility. The damage to MoS_2 was minimal, intermediate, and catastrophic at a 390-keV He^+ fluence of 10^{14} ions/cm^2, 10^{15} ions/cm^2, and 10^{16} ions/cm^2, respectively. When exposed to a 390-keV He^+ fluence of 10^{15} ions/cm^2 and a 2-MeV proton fluence of 1.26×10^{16} ions/cm^2, although the V_T shift and SS degradation were observed, the back-gated MoS_2 FETs still maintain good performance with high on-state current and high on/off current ratio. This fluence level is higher than the lifetime doses encountered by most satellites in even the most radiation-prone orbits and corresponds to hundreds or thousands of years of proton and alpha particle irradiation in space with minimal shielding [198]. The structural damage of MoS_2 from proton and He ion irradiation was also studied by MD simulations. With more than 300,000 simulations, the SYs of S and Mo atoms and probabilities of different types of defects were obtained for a wide range of ion energies up to 2000 keV. It was found that single-S vacancy is the most probable defect even for high energy ions. The possible defect size increases with the ion energy, but small point defects are the dominant defect structures. The quantitative estimation from the simulations provides useful insight into the physical defects induced by ion irradiation. Simulations of multi-layer MoS_2 and transport properties of defected MoS_2 will further help understand the radiation effects observed from the experiments.

CHAPTER V

Conclusions and Future Work

5.1 Summary and conclusions

Understanding the ion irradiation effects on 2D materials is important for using controlled radiation to achieve material functionalization and assessing radiation resilience of 2D materials and electronics for applications in radiation-harsh environments. In this work, the impact of ion irradiation on material structure, surface chemistry, and electronic properties has been studied for three different 2D materials (graphene, WSe_2, and MoS_2) through MD simulations and ion irradiation experiments.

First, a comprehensive study of graphene defects induced by proton irradiation was performed using both classical and *ab-initio* MD simulations. This includes a novel approach to systematically treat the dynamics of proton-graphene interactions via *ab-initio* simulation, which provides useful insight into the accuracy of the commonly used classical MD approach. It has been shown that relatively good agreement on defect generation probabilities can be reached between the two simulation approaches at a proton energy of 1 and 10 keV. However, at 0.1 keV, the SV generation probabilities diverge significantly due to reduced accuracy in the empirical potential used by the classical MD approach. At low energy, the defect probability is sensitive to the angle-dependent threshold displacement energy and, therefore, a

small difference in the threshold displacement energy can lead to a large difference in the defect generation probability. Next, the defect structures and defect generation probabilities were examined as a function of proton energy at normal incidence. As the proton energy increases from 0.1 keV to 100 keV, defect structures transition from simple SVs and FPs to a rich variety of topological defects. With high-energy protons, defect structures with large formation energies can be produced due to the large energy injection from the incident ion. The SV defect probability first increases with proton energy due to the increasing energy from the incident ion and then decreases with proton energy due to the shorter interaction time between the PKA and the ion. The generation probabilities of DV and other defect structures have a more complicated dependence on proton energy due to the possibility of different types of collision sequences. The impact of proton incident angle on the defect generation was also investigated using classical MD simulations. The azimuthal angle of the incident ion has a relatively small impact on the defect probabilities. However, the polar angle can greatly impact the defect probabilities. By establishing correlations between the proton impact position, proton energy, incidence direction, and graphene crystal structure, the evolution of the defect structures and defect occurrence probabilities as a function of the irradiation parameters can be clearly explained by various competing mechanisms. The simulation results show that it is possible to tune proton energy and angle to change the relative probabilities of creating different types of defects to achieve graphene functionalization.

In order to evaluate the potential of WSe_2-based electronics for use in high-radiation environments, proton and heavy-ion irradiation at MeV-level energies were performed on layered WSe_2 and SiC heterostructures. XPS was used to study the impact of ion irradiation on WSe_2 chemical and electronic properties. For 2-MeV incident protons, there was no detectable oxidation even at a high fluence level of 10^{17} protons/cm^2. At a fluence of 10^{16} protons/cm^2, charge transfer between WSe_2

and SiC substrate was observed due to a combination of radiation-induced defects and charge trapping in pre-existing defects. Below this threshold, no significant charging effect was found in either material. The method for fabricating WSe_2 also influences the charging behaviour and the extent of VBO shift between WSe_2 and SiC substrate. This is explained by the difference in the number of WSe_2 layers and the difference in initial sample conditions. In contrast with mechanically exfoliated samples, MOCVD-grown WSe_2 exhibits a reduced number of layers and a larger density of pre-existing interface states, which lead to a more significant impact on the charging behavior from the interface. Heavy-ion irradiation (Fe and Ag ions) at a fluence of 10^{16} ions/cm^2 was found to cause significant structural damage to both WSe_2 and SiC. The WSe_2 lost its semiconducting properties after the heavy-ion irradiation and subsequent oxidation. A reduced heavy-ion fluence is needed to accurately determine the onset of radiation damage. Based on these results, from the material perspective, WSe_2 can withstand 2-MeV proton irradiation up to 10^{16} ions/cm^2. The radiation resilience of WSe_2-based FET is not expected to be constrained by WSe_2 itself, but rather by the radiation hardness of other components that are less radiation-tolerant, such as the dielectric.

After studying the material-level ion irradiation effects, the degradation of MoS_2 FET electrical performance was investigated with high-energy protons and helium ions. In contrast with previous methods, the MoS_2 and SiO_2 substrate were irradiated individually before fabricating the FET device. Such an experimental approach is able to decouple the radiation damage of 2D materials from that of the underlying dielectric substrate. For 390-keV He ions, degradation of transfer characteristics became statistically significant at a fluence of 10^{15} ions/cm^2. When only MoS_2 was irradiated, an increase in the subthreshold slope and a decrease in the mobility were observed, along with a positive shift in threshold voltage. These changes can be attributed to the generation of structural defects and interface states within MoS_2.

When only SiO_2 was irradiated, an increase in the subthreshold slope was also observed because trapped oxide charges can migrate to the MoS_2/SiO_2 interface and behave similarly to interface states. However, a negative shift in the threshold voltage occurred due to the creation of positive oxide charges. The decrease in mobility was not significant since there was no damage in the channel material. The contribution of nuclear energy loss to the degradation of mobility and subthreshold slope was also shown from the proton and helium irradiation experiments at the same dose. To estimate the order of magnitude of physical defects induced by protons and helium ions, MD simulations were performed to study the defect generation in monolayer MoS_2. The REBO and ZBL potentials were smoothly connected to describe the cascade collisions within MoS_2. The sputtering yields of Mo and S atoms and the probability of defect sites were determined for a range of ion energies up to 2 MeV. The sputtering ratio and defect density under each irradiation condition (390-keV He ions and 2-MeV protons) were also determined. Based on the distribution of defect size at each energy, it was shown that for the studied ion energy range, the most probable defect structure is single-S vacancy. Other defects with high generation probability include structural disorder without sputtering, double-S vacancies, and defect structures with one Mo vacancy and one to three S vacancies. With increasing ion energy, the possible defect size can be larger, but point defects such as single-S vacancy are still the dominant defect structures.

The simulation results from this work provide a quantitative estimation of the occurrence probabilities of different types of defect structures for a wide range of ion energies and angles. These results are useful for interpreting previous ion irradiation experiments, designing future experiments for material functionalization, as well as estimating aggregated ion damage effects in a space environment. The onset dose for the material-level and transistor-level degradation of 2D materials is also determined experimentally, which is useful for evaluating the resilience of 2D materials in

a radiation-harsh environment.

5.2 Future work

In order to model the ion interaction process accurately, the interatomic potentials used in the classical MD simulation need to provide accurate defect formation energies and displacement energies, as well as an accurate description of the chemical bonds so that the relaxed defect structure can be trusted. For graphene, the Tersoff/ZBL potential was used, but it would be interesting to compare our results with the AIREBO potential [108], which is also widely used for studying graphene structural and chemical properties [109, 110]. As with the REBO potential for MoS_2, the AIREBO potential will need to be smoothly connected with the ZBL potential so that cascade collisions can be accurately computed. For WSe_2, a potential with accurate defect formation energies and interatomic forces is not available to date. If such potential can be developed, the defect probabilities can also be simulated, which could help estimate the density of structural defects produced from high-energy protons under experimental irradiation conditions. In order to quantitatively validate the simulation results, it is possible to perform measurements using scanning transmission electron microscopy and calculate the density of ion-induced defects in a monolayer sample. It is worth noting, however, that the simulated defect structures are initial defects created immediately at the time of irradiation and can experience further migration and structural transformation over longer time scales. In any case, such validation with experiment is still useful and can provide important insight into the defect formation and migration process.

With MD simulations, standalone monolayer graphene and MoS_2 were studied. For many applications, the use of 2D materials is not limited to a single layer, and usually, there is a substrate beneath the material. For example, in the MoS_2 FET experiments, the number of MoS_2 layers ranged from a monolayer to several layers,

and MoS_2 flakes were positioned on top of the SiO_2 substrate. As such, it would be interesting to simulate the response of 2D materials in a configuration that is closer to that studied by experiment. It has been shown in simulations that for multilayer graphene, ion irradiation can break the planar sp^2 bonds and lead to interlayer cross-linking [83, 87]. Also, for a monolayer material, once atoms are ejected from the surface, they cannot lead to further damage, whereas for a multilayer system, ejected atoms can lead to cascade collisions in other layers [83]. This is evident in the simulation results for monolayer MoS_2, which show a much more convoluted evolution of defect probability than graphene, since MoS_2 consists of three layers of atoms. For multilayer 2D materials, it is yet unclear how defects are produced and how defect probability changes as a function of the layer number and the total number of layers. Therefore, further simulations are needed to study the dependence of defect generation on the thickness of 2D materials. In order to simulate interactions between 2D materials and substrates, accurate interatomic potentials between the corresponding atoms are needed. Such potentials are available for graphene and SiO_2, and bombardment of graphene on SiO_2 substrate from swift heavy ions has been simulated in prior work [51]. However, for TMD materials and other types of substrates, most of the potentials are currently not available in the literature. If such potentials are developed in the future, it would be possible to use simulations to study the impact of ion irradiation on the structural damage at the 2D material/substrate interface, which has been shown to have a great impact on the performance of 2D electronics.

APPENDICES

APPENDIX A

Optical images and XPS spectra of ion-irradiated WSe_2 samples

Optical images of ion-irradiated WSe_2 samples

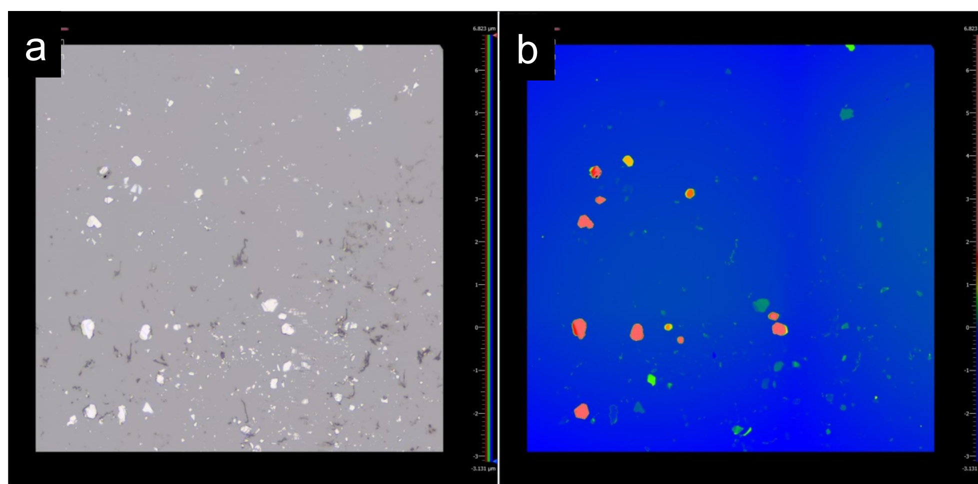

Figure A.1: Optical image of exfoliated WSe_2. (a) Optical image of exfoliated WSe_2 flakes on 6H-SiC substrate taken by white light interferometry (optical profilometry). (b) Using this technique, the thickness of the WSe_2 flakes can also be measured. The thickness ranges from several layers to several microns. The sparse coverage of exfoliated material allows the substrate to be examined in XPS measurements.

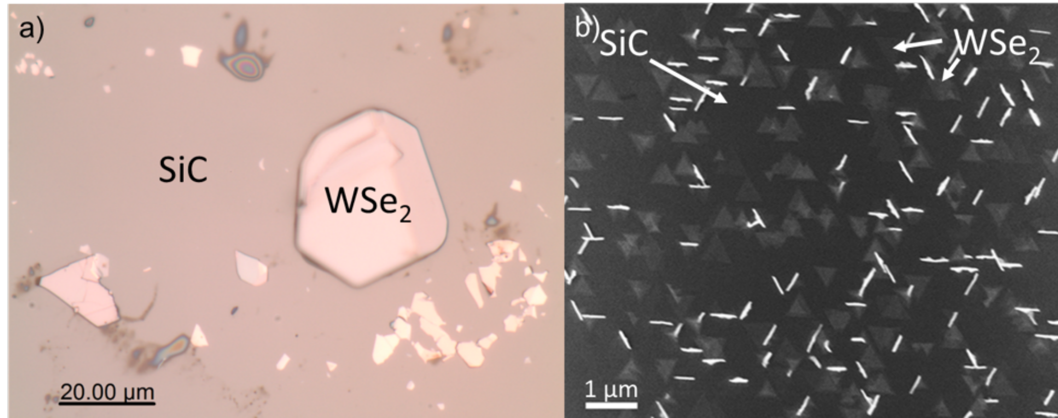

Figure A.2: Images of the exfoliated and directly grown WSe_2 flakes on the SiC substrate. (a) Optical image of exfoliated WSe_2 flakes on the SiC substrate; b) Image of MOCVD-grown WSe_2 flakes on the SiC substrate taken via scanning electron microscopy. Bright white streaks correspond to vertical growth of the WSe_2, leading to fins rather than flakes.

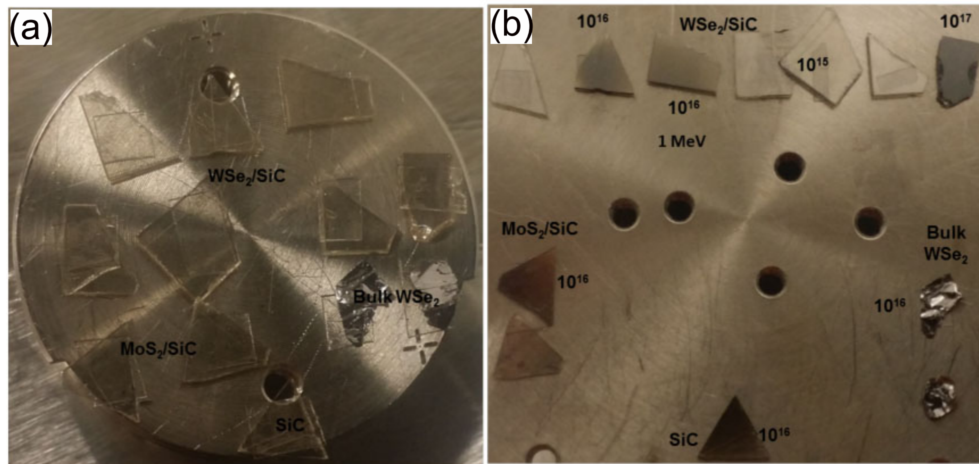

Figure A.3: Proton-irradiated samples before and after irradiation. (a) Digital camera image of the TMD samples before irradiation. The samples are transparent due to the wide bandgap of SiC and the nanoscale dimensions of the WSe_2 and MoS_2. (b) Digital camera image of the TMD samples after proton irradiation. Control samples (unlabeled) and samples exposed to 10^{15} protons/cm^2 are mostly transparent. Samples exposed to 10^{16} protons/cm^2 and 10^{17} protons/cm^2 turn black due to proton beam damage.

XPS spectra of ion-irradiated WSe_2 samples

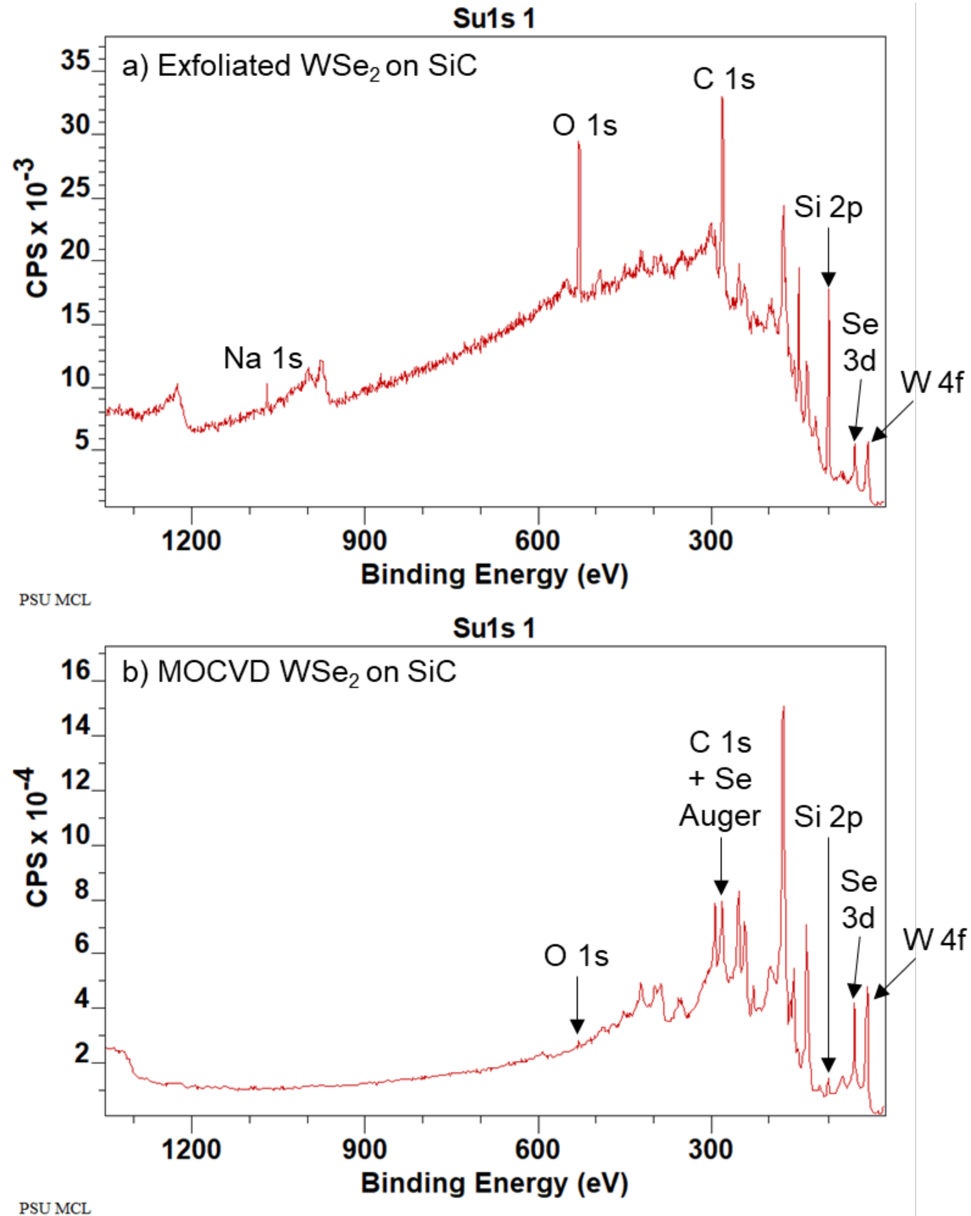

Figure A.4: Representative XPS survey spectra of the WSe_2/SiC heterostructures. (a) Survey spectrum of the WSe_2/SiC heterostructure generated via mechanical exfoliation of the WSe_2. (b) Survey spectrum of the WSe_2/SiC heterostructure generated via direct growth of the WSe_2 by MOCVD. Both spectra are presented without charge correction. The major elemental peaks are labeled here. A trace amount of sodium was also detected on the sample with the exfoliated WSe_2. It is noted that for the case of MOCVD growth of WSe_2, there is a prominent selenium Auger line that overlaps with the C 1s peak.

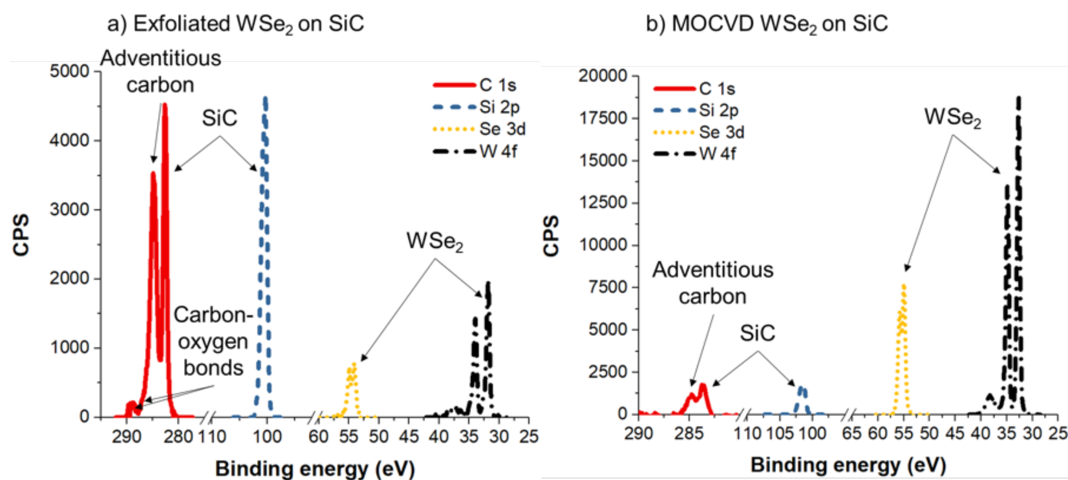

Figure A.5: Representative initial core-level XPS spectra for WSe_2/SiC heterostructures. (a) High-resolution core-level spectra of the WSe_2/SiC heterostructure generated via mechanical exfoliation of the WSe_2. (b) High-resolution core-level spectra of the WSe_2/SiC heterostructure generated via direct growth of the WSe_2 by MOCVD. Spectra are charge corrected as discussed in the main text. Constituent compounds are labeled here. It is noted that for the case of MOCVD growth of WSe_2, there is a prominent selenium Auger line that overlaps with the C 1s peak. The signal from that line was separated from the C 1s signals using data from pristine bulk samples in the high-resolution data, and was subtracted from the spectra presented here. The background has also been subtracted in the spectra.

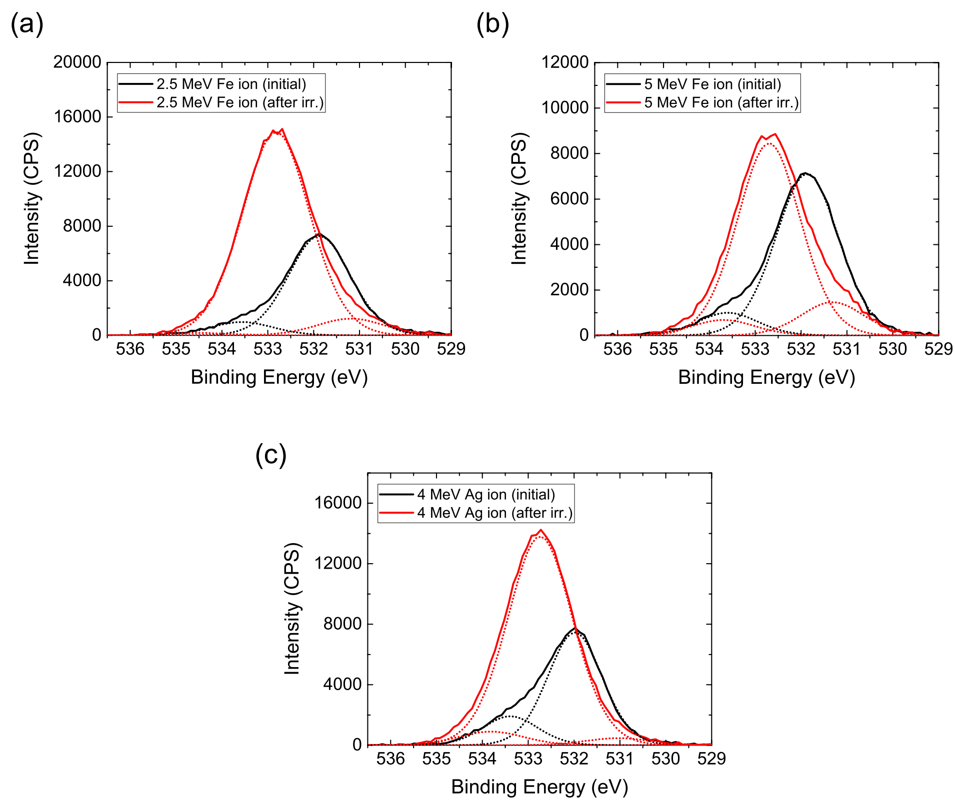

Figure A.6: Change of Oxygen 1s peak spectrum after heavy ion irradiation. O 1s spectra before (black) and after the irradiation (red) for sample exposed to the heavy ions. The initial oxygen spectra contain two chemical environments – one for adsorbed moisture and the other for organic contaminants. The final spectra contain those two peaks and a third peak corresponding to metal oxides.

APPENDIX B

MoS_2 field-effect transistor device fabrication procedure

Fabrication of MoS_2 field-effect transistors

The MoS_2 was exfoliated using the standard tape method onto the target substrates from a natural bulk crystal purchased from SPI supplies. The samples were spun at 4000 rpm for 45 s with MMA EL6 photoresist and baked at 150 °C for 90 s. A second coat of PMMA A3 was spun with identical conditions and baked at 180 °C for 90 s. They were then patterned using a 100-kV Vistec EBPG 5200 electron beam lithography tool with a dose of 300 $\mu C/cm^2$. The develop consisted of immersion for 60 s in 1:1 MIBK:IPA solution followed by 45 s in IPA. 40 nm Ni/30 nm Au contacts are deposited using a Kurt J. Lesker Lab-18 electron beam evaporation tool. Liftoff was then performed in room temperature acetone with a rinse in IPA.

In order to transfer the flakes to a new substrate, the samples were first spun with PMMA A6 at 4000 rpm for 45 s. They were then allowed to dry at room temperature for 24 hours to avoid any film stresses that may result from baking. A razor was used to remove the PMMA around the edge of the sample to allow the solution to

approach the edge of the PMMA at the SiO_2 surface without any irregularities in the PMMA that may have been present at the edge of the sample after the spinning. The substrate with PMMA was then placed in a beaker of 1 molar NaOH solution and allowed to float at the top. The NaOH removed the PMMA film through capillary action, which was then transferred to a series of three deionized water baths using a glass slide. The film was then lifted onto the target substrate and allowed to dry by heating on a hot plate at 50 °C for 10 minutes and then at 70 °C for 10 minutes. Finally, the dried PMMA film was removed in a bath of room temperature acetone leaving the flakes behind on the new substrate.

APPENDIX C

Supplementary simulation results on proton and helium ion irradiation of MoS_2

Classical MD simulation results on proton and helium irradiation of MoS_2

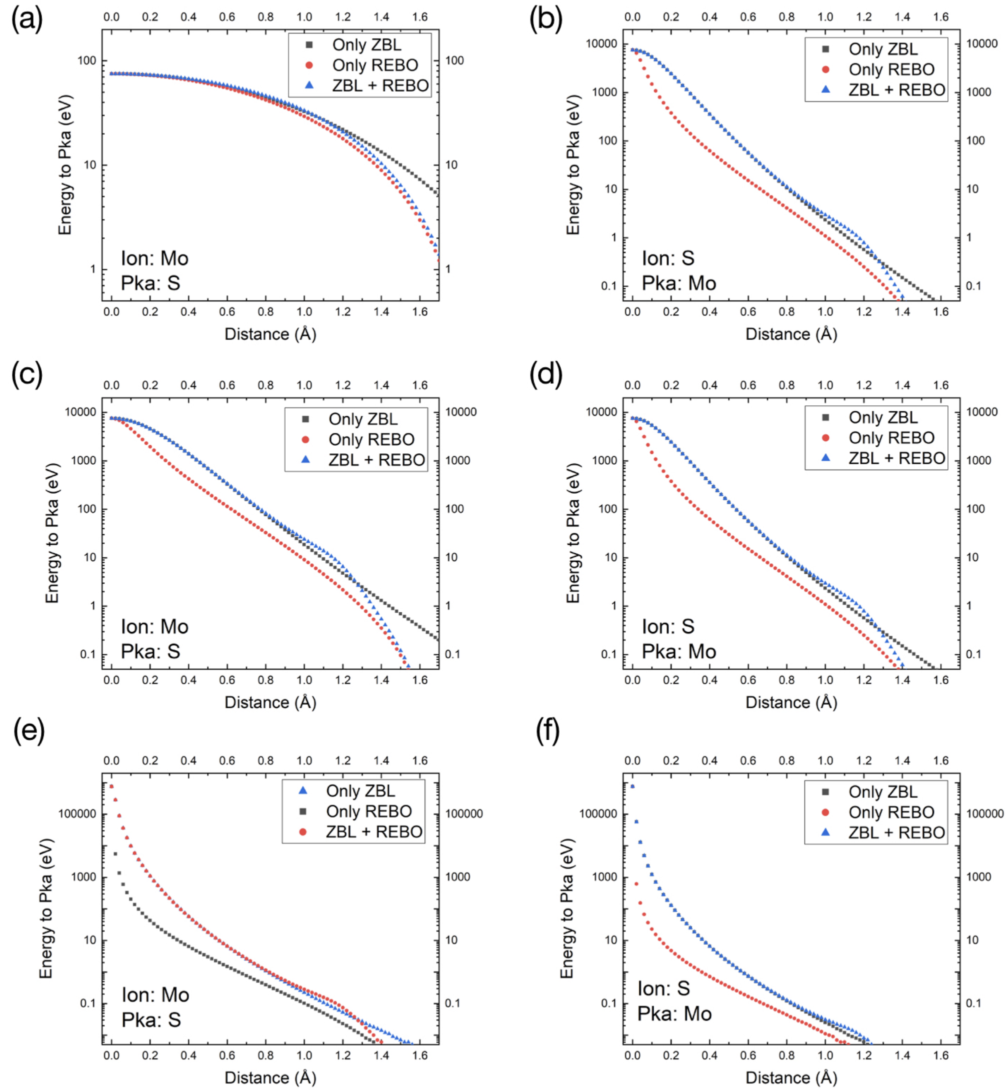

Figure C.1: Energy transfer between Mo and S atoms as a function of the ion impact position with the ZBL, REBO, and combined ZBL/REBO potential. For a Mo ion incident on a S PKA, the energy is shown for an ion kinetic energy of (a) 0.1 keV, (c) 10 keV and (e) 1000 keV. For a S ion incident on a Mo PKA, the energy is shown for an ion kinetic energy of (b) 0.1 keV, (d) 10 keV and (f) 1000 keV.

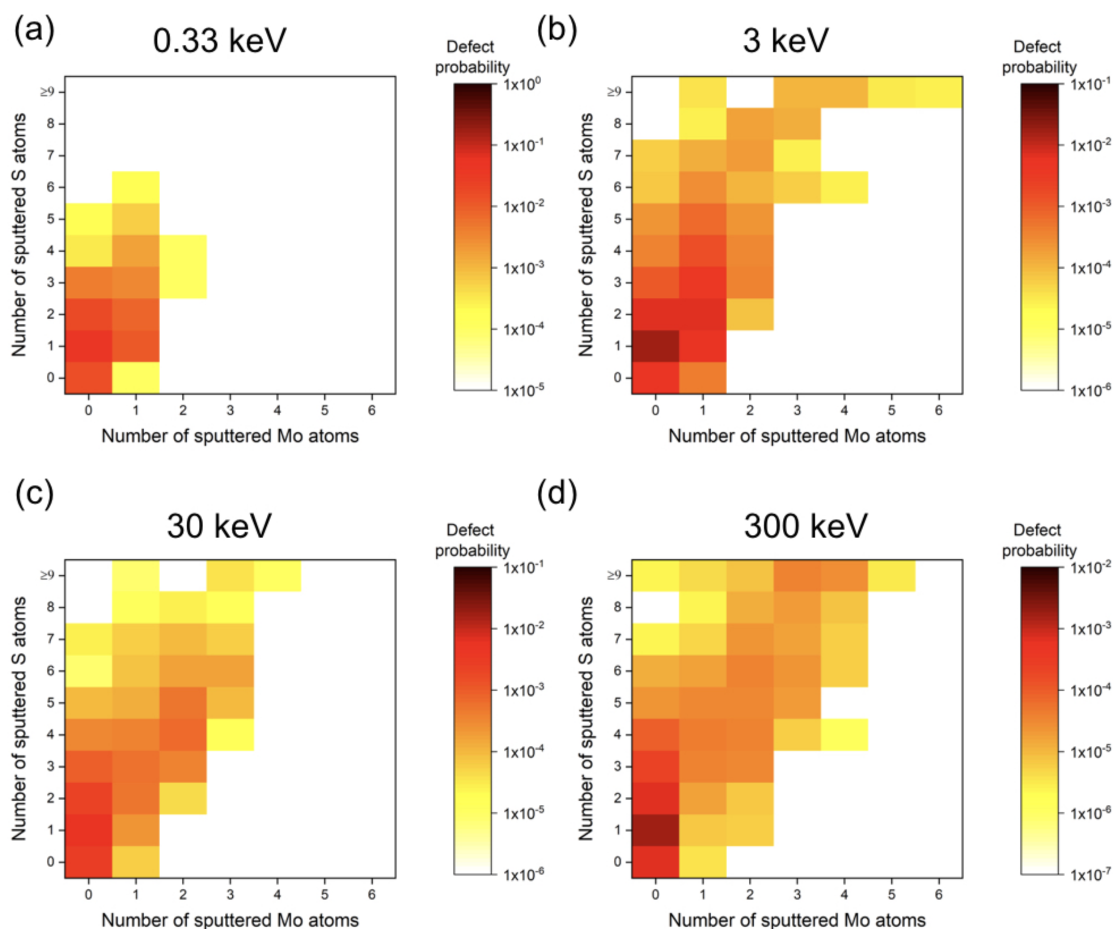

Figure C.2: Probability of defect size as a function of the number of sputtered Mo (X-axis) and S atoms (Y-axis) for a He energy of (a) 0.33 keV, (b) 3 keV, (c) 30 keV, and (d) 300 keV. The probability of zero sputtered Mo and S atom corresponds to the probability of structural disorder without atom being ejected. The scale for the color map is 1×10^{-5} to 1 in (a), 1×10^{-6} to 1×10^{-1} in (b) and (c), and 1×10^{-7} to 1×10^{-2} in (d).

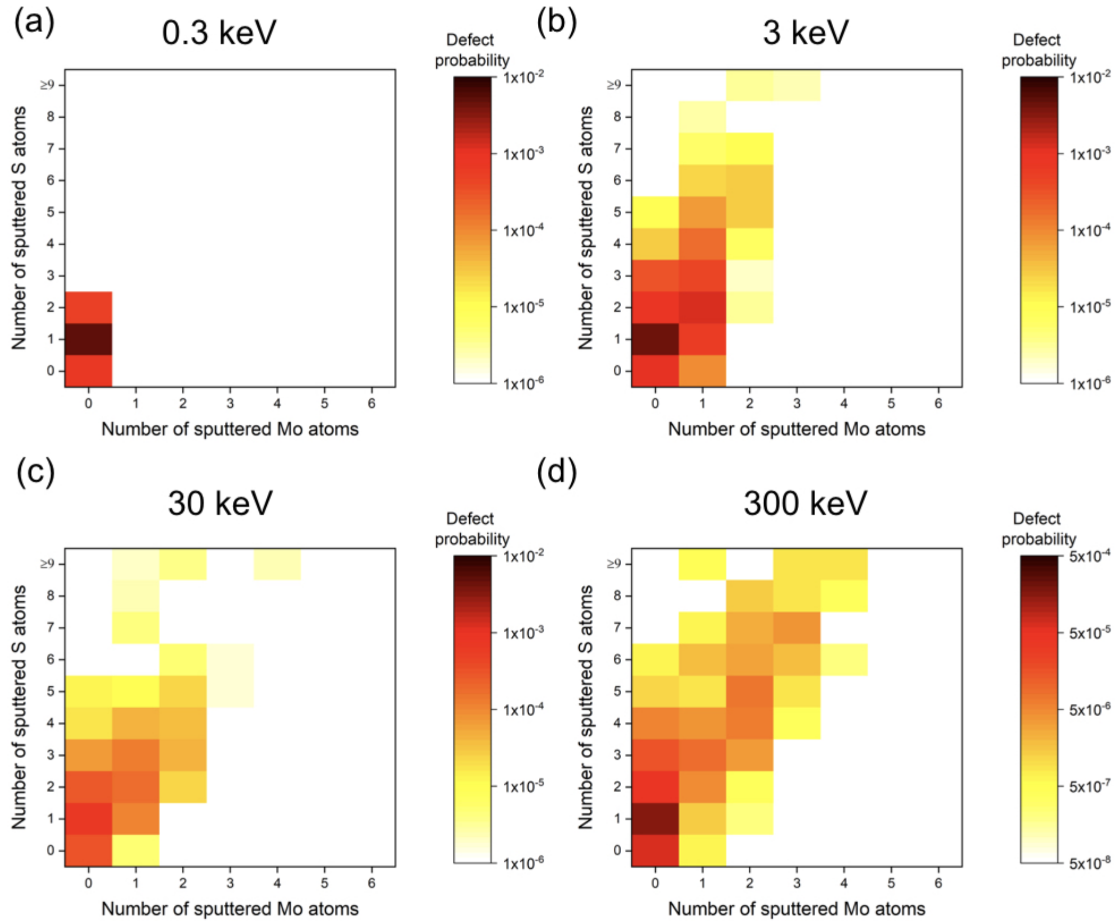

Figure C.3: Probability of defect size as a function of the number of sputtered Mo (X-axis) and S atoms (Y-axis) for a proton energy of (a) 0.3 keV, (b) 3 keV, (c) 30 keV, and (d) 300 keV. The probability of zero sputtered Mo and S atom corresponds to the probability of structural disorder without atom being ejected. The scale for the color map is 1×10^{-6} to 1×10^{-2} in (a)–(c) and 5×10^{-8} to 5×10^{-4} in (d).

BIBLIOGRAPHY

BIBLIOGRAPHY

[1] J. F. Ziegler, M. D. Ziegler, and J. P. Biersack, “SRIM–the stopping and range of ions in matter (2010),” *Nucl. Instr. Meth. Phys. Res. B*, vol. 268, no. 11, pp. 1818–1823, 2010.

[2] K. Santosh, R. C. Longo, R. Addou, R. M. Wallace, and K. Cho, “Impact of intrinsic atomic defects on the electronic structure of MoS_2 monolayers,” *Nanotechnology*, vol. 25, no. 37, p. 375703, 2014.

[3] W. Zhou, X. Zou, S. Najmaei, Z. Liu, Y. Shi, J. Kong, J. Lou, P. M. Ajayan, B. I. Yakobson, and J.-C. Idrobo, “Intrinsic structural defects in monolayer molybdenum disulfide,” *Nano letters*, vol. 13, no. 6, pp. 2615–2622, 2013.

[4] M. Ghorbani-Asl, S. Kretschmer, D. E. Spearot, and A. V. Krasheninnikov, “Two-dimensional MoS_2 under ion irradiation: from controlled defect production to electronic structure engineering,” *2D Materials*, vol. 4, no. 2, p. 025078, 2017.

[5] I. Frank, D. M. Tanenbaum, A. M. van der Zande, and P. L. McEuen, “Mechanical properties of suspended graphene sheets,” *Journal of Vacuum Science & Technology B: Microelectronics and Nanometer Structures Processing, Measurement, and Phenomena*, vol. 25, no. 6, pp. 2558–2561, 2007.

[6] K. Liu and J. Wu, “Mechanical properties of two-dimensional materials and heterostructures,” *Journal of Materials Research*, vol. 31, no. 7, pp. 832–844, 2016.

[7] M. Chhowalla, H. S. Shin, G. Eda, L.-J. Li, K. P. Loh, and H. Zhang, “The chemistry of two-dimensional layered transition metal dichalcogenide nanosheets,” *Nature chemistry*, vol. 5, no. 4, p. 263, 2013.

[8] Q. H. Wang, K. Kalantar-Zadeh, A. Kis, J. N. Coleman, and M. S. Strano, “Electronics and optoelectronics of two-dimensional transition metal dichalcogenides,” *Nat. Nanotechnol.*, vol. 7, no. 11, pp. 699–712, 2012.

[9] S. Z. Butler, S. M. Hollen, L. Cao, Y. Cui, J. A. Gupta, H. R. Gutiérrez, T. F. Heinz, S. S. Hong, J. Huang, A. F. Ismach, *et al.*, “Progress, challenges, and opportunities in two-dimensional materials beyond graphene,” *ACS nano*, vol. 7, no. 4, pp. 2898–2926, 2013.

[10] H. Jin, C. Guo, X. Liu, J. Liu, A. Vasileff, Y. Jiao, Y. Zheng, and S.-Z. Qiao, "Emerging two-dimensional nanomaterials for electrocatalysis," *Chemical reviews*, vol. 118, no. 13, pp. 6337–6408, 2018.

[11] L. Yang, P. Liu, J. Li, and B. Xiang, "Two-dimensional material molybdenum disulfides as electrocatalysts for hydrogen evolution," *Catalysts*, vol. 7, no. 10, p. 285, 2017.

[12] W. Zhang, Z. Huang, W. Zhang, and Y. Li, "Two-dimensional semiconductors with possible high room temperature mobility," *Nano Research*, vol. 7, no. 12, pp. 1731–1737, 2014.

[13] W. Bao, X. Cai, D. Kim, K. Sridhara, and M. S. Fuhrer, "High mobility ambipolar MoS_2 field-effect transistors: Substrate and dielectric effects," *Applied Physics Letters*, vol. 102, no. 4, p. 042104, 2013.

[14] S. Chen, Q. Wu, C. Mishra, J. Kang, H. Zhang, K. Cho, W. Cai, A. A. Balandin, and R. S. Ruoff, "Thermal conductivity of isotopically modified graphene," *Nature materials*, vol. 11, no. 3, p. 203, 2012.

[15] B. Mortazavi, M. Makaremi, M. Shahrokhi, M. Raeisi, C. V. Singh, T. Rabczuk, and L. F. C. Pereira, "Borophene hydride: a stiff 2D material with high thermal conductivity and attractive optical and electronic properties," *Nanoscale*, vol. 10, no. 8, pp. 3759–3768, 2018.

[16] J. Kim, S. S. Baik, S. H. Ryu, Y. Sohn, S. Park, B.-G. Park, J. Denlinger, Y. Yi, H. J. Choi, and K. S. Kim, "Observation of tunable band gap and anisotropic Dirac semimetal state in black phosphorus," *Science*, vol. 349, no. 6249, pp. 723–726, 2015.

[17] J. Wu, B. Wang, Y. Wei, R. Yang, and M. Dresselhaus, "Mechanics and mechanically tunable band gap in single-layer hexagonal boron-nitride," *Materials Research Letters*, vol. 1, no. 4, pp. 200–206, 2013.

[18] R. Quhe, J. Zheng, G. Luo, Q. Liu, R. Qin, J. Zhou, D. Yu, S. Nagase, W. Mei, Z. Gao, *et al.*, "Tunable and sizable band gap of single-layer graphene sandwiched between hexagonal boron nitride," *NPG Asia Materials*, vol. 4, no. 2, p. e6, 2012.

[19] M. Bernardi, M. Palummo, and J. C. Grossman, "Extraordinary sunlight absorption and one nanometer thick photovoltaics using two-dimensional monolayer materials," *Nano letters*, vol. 13, no. 8, pp. 3664–3670, 2013.

[20] B. Cho, J. Yoon, S. K. Lim, A. R. Kim, D.-H. Kim, S.-G. Park, J.-D. Kwon, Y.-J. Lee, K.-H. Lee, B. H. Lee, *et al.*, "Chemical sensing of 2D graphene/MoS_2 heterostructure device," *ACS applied materials & interfaces*, vol. 7, no. 30, pp. 16775–16780, 2015.

[21] G. Fiori, F. Bonaccorso, G. Iannaccone, T. Palacios, D. Neumaier, A. Seabaugh, S. K. Banerjee, and L. Colombo, "Electronics based on two-dimensional materials," *Nature nanotechnology*, vol. 9, no. 10, p. 768, 2014.

[22] S. Y. Zhou, G.-H. Gweon, A. V. Fedorov, P. N. First, W. A. De Heer, D.-H. Lee, F. Guinea, A. H. Castro Neto, and A. Lanzara, "Substrate-induced bandgap opening in epitaxial graphene," *Nature materials*, vol. 6, no. 10, p. 770, 2007.

[23] R. Balog, B. Jørgensen, L. Nilsson, M. Andersen, E. Rienks, M. Bianchi, M. Fanetti, E. Lægsgaard, A. Baraldi, S. Lizzit, *et al.*, "Bandgap opening in graphene induced by patterned hydrogen adsorption," *Nature materials*, vol. 9, no. 4, p. 315, 2010.

[24] F. Schwierz, "Graphene transistors," *Nature nanotechnology*, vol. 5, no. 7, p. 487, 2010.

[25] B. Radisavljevic, A. Radenovic, J. Brivio, V. Giacometti, and A. Kis, "Single-layer MoS_2 transistors," *Nature nanotechnology*, vol. 6, no. 3, p. 147, 2011.

[26] T. Roy, M. Tosun, J. S. Kang, A. B. Sachid, S. B. Desai, M. Hettick, C. C. Hu, and A. Javey, "Field-effect transistors built from all two-dimensional material components," *ACS nano*, vol. 8, no. 6, pp. 6259–6264, 2014.

[27] H. Wang, L. Yu, Y.-H. Lee, Y. Shi, A. Hsu, M. L. Chin, L.-J. Li, M. Dubey, J. Kong, and T. Palacios, "Integrated circuits based on bilayer MoS_2 transistors," *Nano letters*, vol. 12, no. 9, pp. 4674–4680, 2012.

[28] H. Hughes and J. Benedetto, "Radiation effects and hardening of MOS technology: devices and circuits," *IEEE Transactions on Nuclear Science*, vol. 50, no. 3, pp. 500–521, 2003.

[29] T.-P. Ma and P. V. Dressendorfer, *Ionizing radiation effects in MOS devices and circuits*. John Wiley & Sons, 1989.

[30] S. Mathew, T. Chan, D. Zhan, K. Gopinadhan, A. R. Barman, M. Breese, S. Dhar, Z. Shen, T. Venkatesan, and J. T. Thong, "Mega-electron-volt proton irradiation on supported and suspended graphene: A Raman spectroscopic layer dependent study," *J. Appl. Phys.*, vol. 110, no. 8, p. 084309, 2011.

[31] S. Mathew, K. Gopinadhan, T. Chan, X. Yu, D. Zhan, L. Cao, A. Rusydi, M. Breese, S. Dhar, Z. Shen, *et al.*, "Magnetism in MoS_2 induced by proton irradiation," *Applied Physics Letters*, vol. 101, no. 10, p. 102103, 2012.

[32] T.-Y. Kim, K. Cho, W. Park, J. Park, Y. Song, S. Hong, W.-K. Hong, and T. Lee, "Irradiation effects of high-energy proton beams on MoS_2 field effect transistors," *ACS nano*, vol. 8, no. 3, pp. 2774–2781, 2014.

[33] B. Wang, S. Yang, J. Chen, C. Mann, A. Bushmaker, and S. B. Cronin, "Radiation-induced direct bandgap transition in few-layer MoS_2," *Applied Physics Letters*, vol. 111, no. 13, p. 131101, 2017.

[34] I. Childres, L. A. Jauregui, M. Foxe, J. Tian, R. Jalilian, I. Jovanovic, and Y. P. Chen, "Effect of electron-beam irradiation on graphene field effect devices," *Applied Physics Letters*, vol. 97, no. 17, p. 173109, 2010.

[35] G. S. Was, *Fundamentals of radiation materials science: metals and alloys*. Springer, 2016.

[36] M. Born and J. E. Mayer, "Zur gittertheorie der ionenkristalle," *Zeitschrift für Physik*, vol. 75, no. 1-2, pp. 1–18, 1932.

[37] O. Firsov, "Interaction energy of atoms for small nuclear separations," *Soviet Physics JETP-USSR*, vol. 5, no. 6, pp. 1192–1196, 1957.

[38] O. Firsov, "Calculation of atomic interaction potentials," *Zh. Eksp. Teor. Fiz*, vol. 33, p. 696, 1957.

[39] R. Devanathan, T. D. de la Rubia, and W. J. Weber, "Displacement threshold energies in β-SiC," *Journal of nuclear materials*, vol. 253, no. 1-3, pp. 47–52, 1998.

[40] N. Bohr, *The penetration of atomic particles through matter*, vol. 8. I Kommission hos Ejnar Munksgaard, 1953.

[41] A. Sommerfeld, "Asymptotische integration der differentialgleichung des Thomas-Fermischen atoms," *Zeitschrift für Physik A Hadrons and Nuclei*, vol. 78, no. 5, pp. 283–308, 1932.

[42] H. Jensen, "Die ladungsverteilung in ionen und die gitterkonstante des Rubidiumbromids nach der statistischen methode," *Zeitschrift für Physik*, vol. 77, no. 11-12, pp. 722–745, 1932.

[43] G. Molière, "Theorie der streuung schneller geladener teilchen i. einzelstreuung am abgeschirmten coulomb-feld," *Zeitschrift für Naturforschung A*, vol. 2, no. 3, pp. 133–145, 1947.

[44] W. Wilson, L. Haggmark, and J. Biersack, "Calculations of nuclear stopping, ranges, and straggling in the low-energy region," *Physical Review B*, vol. 15, no. 5, p. 2458, 1977.

[45] J. Zeigler, J. Biersack, and U. Littmark, "The stopping and range of ions in solids," *The Stopping and Range of Ions in Matter*, vol. 1, 1985.

[46] H.-P. Komsa, J. Kotakoski, S. Kurasch, O. Lehtinen, U. Kaiser, and A. V. Krasheninnikov, "Two-dimensional transition metal dichalcogenides under electron irradiation: defect production and doping," *Phys. Rev. Lett.*, vol. 109, no. 3, p. 035503, 2012.

[47] A. Ojanperä, A. V. Krasheninnikov, and M. Puska, "Electronic stopping power from first-principles calculations with account for core electron excitations and projectile ionization," *Physical Review B*, vol. 89, no. 3, p. 035120, 2014.

[48] A. Schleife, Y. Kanai, and A. A. Correa, "Accurate atomistic first-principles calculations of electronic stopping," *Physical Review B*, vol. 91, no. 1, p. 014306, 2015.

[49] H. A. Bethe, "Passage of radiations through matter," *Experimental nuclear physics*, 1953.

[50] G. Vineyard, "Thermal spikes and activated processes," *Radiation effects*, vol. 29, no. 4, pp. 245–248, 1976.

[51] S. Zhao and J. Xue, "Modification of graphene supported on SiO_2 substrate with swift heavy ions from atomistic simulation point," *Carbon*, vol. 93, pp. 169–179, 2015.

[52] R. Walker, T. Shi, E. Silva, I. Jovanovic, and J. Robinson, "Radiation effects on two-dimensional materials," *Phys. Status Solidi A*, 2016.

[53] M. G. Stanford, P. R. Pudasaini, A. Belianinov, N. Cross, J. H. Noh, M. R. Koehler, D. G. Mandrus, G. Duscher, A. J. Rondinone, I. N. Ivanov, *et al.*, "Focused helium-ion beam irradiation effects on electrical transport properties of few-layer WSe_2: enabling nanoscale direct write homo-junctions," *Scientific reports*, vol. 6, p. 27276, 2016.

[54] D. S. Fox, Y. Zhou, P. Maguire, A. O'Neill, C. Ó'Coileáin, R. Gatensby, A. M. Glushenkov, T. Tao, G. S. Duesberg, I. V. Shvets, *et al.*, "Nanopatterning and electrical tuning of MoS_2 layers with a subnanometer helium ion beam," *Nano letters*, vol. 15, no. 8, pp. 5307–5313, 2015.

[55] S. A. Francis, J. C. Petrosky, J. W. McClory, and C. D. Cress, "Effects of proton and X-ray irradiation on graphene field-effect transistors with thin gate dielectrics," *IEEE Transactions on Nuclear Science*, vol. 61, no. 6, pp. 3010–3017, 2014.

[56] S. Akcöltekin, H. Bukowska, T. Peters, O. Osmani, I. Monnet, I. Alzaher, B. B. d'Etat, H. Lebius, and M. Schleberger, "Unzipping and folding of graphene by swift heavy ions," *Appl. Phys. Lett.*, vol. 98, no. 10, p. 103103, 2011.

[57] O. Ochedowski, S. Akcöltekin, B. Ban-d'Etat, H. Lebius, and M. Schleberger, "Detecting swift heavy ion irradiation effects with graphene," *Nuclear Instruments and Methods in Physics Research Section B: Beam Interactions with Materials and Atoms*, vol. 314, pp. 18–20, 2013.

[58] O. Ochedowski, K. Marinov, G. Wilbs, G. Keller, N. Scheuschner, D. Severin, M. Bender, J. Maultzsch, F. Tegude, and M. Schleberger, "Radiation hardness

of graphene and MoS_2 field effect devices against swift heavy ion irradiation," *J. Appl. Phys.*, vol. 113, no. 21, p. 214306, 2013.

[59] D. C. Bell, M. C. Lemme, L. A. Stern, J. R. Williams, and C. M. Marcus, "Precision cutting and patterning of graphene with helium ions," *Nanotechnology*, vol. 20, no. 45, p. 455301, 2009.

[60] M. C. Lemme, D. C. Bell, J. R. Williams, L. A. Stern, B. W. Baugher, P. Jarillo-Herrero, and C. M. Marcus, "Etching of graphene devices with a helium ion beam," *ACS nano*, vol. 3, no. 9, pp. 2674–2676, 2009.

[61] O. Lehtinen, J. Kotakoski, A. Krasheninnikov, and J. Keinonen, "Cutting and controlled modification of graphene with ion beams," *Nanotechnology*, vol. 22, no. 17, p. 175306, 2011.

[62] D. Wang, Y. Wang, X. Chen, Y. Zhu, K. Zhan, H. Cheng, and X. Wang, "Layer-by-layer thinning of two-dimensional MoS_2 films by using a focused ion beam," *Nanoscale*, vol. 8, no. 7, pp. 4107–4112, 2016.

[63] W. Li, L. Liang, S. Zhao, S. Zhang, and J. Xue, "Fabrication of nanopores in a graphene sheet with heavy ions: A molecular dynamics study," *Journal of Applied Physics*, vol. 114, no. 23, p. 234304, 2013.

[64] G. Berdiyorov, B. Mortazavi, S. Ahzi, F. Peeters, and M. Khraisheh, "Effect of straining graphene on nanopore creation using Si cluster bombardment: A reactive atomistic investigation," *Journal of Applied Physics*, vol. 120, no. 22, p. 225108, 2016.

[65] C. A. Merchant, K. Healy, M. Wanunu, V. Ray, N. Peterman, J. Bartel, M. D. Fischbein, K. Venta, Z. Luo, A. C. Johnson, *et al.*, "DNA translocation through graphene nanopores," *Nano letters*, vol. 10, no. 8, pp. 2915–2921, 2010.

[66] W. Zhao, O. Hofert, K. Gotterbarm, J. Zhu, C. Papp, and H.-P. Steinrück, "Production of nitrogen-doped graphene by low-energy nitrogen implantation," *J. Phys. Chem. C*, vol. 116, no. 8, pp. 5062–5066, 2012.

[67] H. Wang, Q. Wang, Y. Cheng, K. Li, Y. Yao, Q. Zhang, C. Dong, P. Wang, U. Schwingenschlögl, W. Yang, *et al.*, "Doping monolayer graphene with single atom substitutions," *Nano Lett.*, vol. 12, no. 1, pp. 141–144, 2011.

[68] U. Bangert, A. Bleloch, M. Gass, A. Seepujak, and J. Van den Berg, "Doping of few-layered graphene and carbon nanotubes using ion implantation," *Phys. Rev. B*, vol. 81, no. 24, p. 245423, 2010.

[69] E. P. Bellido and J. M. Seminario, "Molecular dynamics simulations of ion-bombarded graphene," *The Journal of Physical Chemistry C*, vol. 116, no. 6, pp. 4044–4049, 2012.

[70] Z. Bai, L. Zhang, and L. Liu, “Improving low-energy boron/nitrogen ion implantation in graphene by ion bombardment at oblique angles,” *Nanoscale*, vol. 8, no. 16, pp. 8761–8772, 2016.

[71] Z. Bai, L. Zhang, and L. Liu, “Bombarding graphene with oxygen ions: combining effects of incident angle and ion energy to control defect generation,” *The Journal of Physical Chemistry C*, vol. 119, no. 47, pp. 26793–26802, 2015.

[72] V. Ferlet-Cavrois, L. W. Massengill, and P. Gouker, “Single event transients in digital CMOS—A review,” *IEEE Transactions on Nuclear Science*, vol. 60, no. 3, pp. 1767–1790, 2013.

[73] F. W. Sexton, “Destructive single-event effects in semiconductor devices and ICs,” *IEEE Transactions on Nuclear Science*, vol. 50, no. 3, pp. 603–621, 2003.

[74] T. Shi, Q. Peng, Z. Bai, F. Gao, and I. Jovanovic, “Proton irradiation of graphene: insights from atomistic modeling,” *Nanoscale*, 2019.

[75] T. Shi, R. C. Walker, I. Jovanovic, and J. A. Robinson, “Effects of energetic ion irradiation on WSe_2/SiC heterostructures,” *Scientific reports*, vol. 7, no. 1, p. 4151, 2017.

[76] R. C. Walker, T. Shi, B. Jariwala, I. Jovanovic, and J. A. Robinson, “Stability of the tungsten diselenide and silicon carbide heterostructure against high energy proton exposure,” *Applied Physics Letters*, vol. 111, no. 14, p. 143104, 2017.

[77] A. J. Arnold, T. Shi, I. Jovanovic, and S. Das, “Extraordinary radiation hardness of atomically thin MoS_2,” *ACS applied materials & interfaces*, vol. 11, no. 8, pp. 8391–8399, 2019.

[78] Z. Li and F. Chen, “Ion beam modification of two-dimensional materials: Characterization, properties, and applications,” *Applied Physics Reviews*, vol. 4, no. 1, p. 011103, 2017.

[79] Y. Zhou, D. S. Fox, and H. Zhang, “Helium ion microscopy for two-dimensional materials,” in *Helium Ion Microscopy*, pp. 245–262, Springer, 2016.

[80] Q. Peng, W. Ji, and S. De, “First-principles study of the effects of mechanical strains on the radiation hardness of hexagonal boron nitride monolayers,” *Nanoscale*, vol. 5, no. 2, pp. 695–703, 2013.

[81] O. Lehtinen, J. Kotakoski, A. Krasheninnikov, A. Tolvanen, K. Nordlund, and J. Keinonen, “Effects of ion bombardment on a two-dimensional target: Atomistic simulations of graphene irradiation,” *Physical review B*, vol. 81, no. 15, p. 153401, 2010.

[82] M. G. Stanford, P. R. Pudasaini, E. T. Gallmeier, N. Cross, L. Liang, A. Oyedele, G. Duscher, M. Mahjouri-Samani, K. Wang, K. Xiao, *et al.*, “High conduction hopping behavior induced in transition metal dichalcogenides by

percolating defect networks: toward atomically thin circuits," *Advanced Functional Materials*, vol. 27, no. 36, p. 1702829, 2017.

[83] X. Wu, H. Zhao, and J. Pei, "Fabrication of nanopore in graphene by electron and ion beam irradiation: Influence of graphene thickness and substrate," *Computational Materials Science*, vol. 102, pp. 258–266, 2015.

[84] Z. Bai, L. Zhang, H. Li, and L. Liu, "Nanopore creation in graphene by ion beam irradiation: geometry, quality, and efficiency," *ACS applied materials & interfaces*, vol. 8, no. 37, pp. 24803–24809, 2016.

[85] D. Cohen-Tanugi and J. C. Grossman, "Water desalination across nanoporous graphene," *Nano letters*, vol. 12, no. 7, pp. 3602–3608, 2012.

[86] G. López-Polín, C. Gómez-Navarro, V. Parente, F. Guinea, M. I. Katsnelson, F. Perez-Murano, and J. Gómez-Herrero, "Increasing the elastic modulus of graphene by controlled defect creation," *Nature Physics*, vol. 11, no. 1, p. 26, 2015.

[87] X. Wu, H. Zhao, M. Zhong, H. Murakawa, and M. Tsukamoto, "Molecular dynamics simulation of graphene sheets joining under ion beam irradiation," *Carbon*, vol. 66, pp. 31–38, 2014.

[88] H. Vázquez, E. Åhlgren, O. Ochedowski, A. Leino, R. Mirzayev, R. Kozubek, H. Lebius, M. Karlušic, M. Jakšic, A. Krasheninnikov, *et al.*, "Creating nanoporous graphene with swift heavy ions," *Carbon*, vol. 114, pp. 511–518, 2017.

[89] K. Yoon, A. Rahnamoun, J. L. Swett, V. Iberi, D. A. Cullen, I. V. Vlassiouk, A. Belianinov, S. Jesse, X. Sang, O. S. Ovchinnikova, *et al.*, "Atomistic-scale simulations of defect formation in graphene under noble gas ion irradiation," *ACS nano*, vol. 10, no. 9, pp. 8376–8384, 2016.

[90] O. V. Yazyev, "Magnetism in disordered graphene and irradiated graphite," *Physical review letters*, vol. 101, no. 3, p. 037203, 2008.

[91] R. Nair, M. Sepioni, I.-L. Tsai, O. Lehtinen, J. Keinonen, A. Krasheninnikov, T. Thomson, A. Geim, and I. Grigorieva, "Spin-half paramagnetism in graphene induced by point defects," *Nature Physics*, vol. 8, no. 3, p. 199, 2012.

[92] F. Banhart, J. Kotakoski, and A. V. Krasheninnikov, "Structural defects in graphene," *ACS nano*, vol. 5, no. 1, pp. 26–41, 2010.

[93] S. Plimpton, "Fast parallel algorithms for short-range molecular dynamics," *Journal of computational physics*, vol. 117, no. 1, pp. 1–19, 1995.

[94] J. M. Soler, E. Artacho, J. D. Gale, A. García, J. Junquera, P. Ordejón, and D. Sánchez-Portal, "The SIESTA method for *ab initio* order-N materials simulation," *Journal of Physics: Condensed Matter*, vol. 14, no. 11, p. 2745, 2002.

[95] J. P. Perdew, K. Burke, and M. Ernzerhof, "Generalized gradient approximation made simple," *Physical review letters*, vol. 77, no. 18, p. 3865, 1996.

[96] J. F. Ziegler and J. P. Biersack, "The stopping and range of ions in matter," in *Treatise on heavy-ion science*, pp. 93–129, Springer, 1985.

[97] J. Tersoff, "Empirical interatomic potential for carbon, with applications to amorphous carbon," *Physical Review Letters*, vol. 61, no. 25, p. 2879, 1988.

[98] C. L. Kelchner, S. Plimpton, and J. Hamilton, "Dislocation nucleation and defect structure during surface indentation," *Physical review B*, vol. 58, no. 17, p. 11085, 1998.

[99] L. Sun, F. Banhart, and J. Warner, "Two-dimensional materials under electron irradiation," *MRS Bulletin*, vol. 40, no. 1, pp. 29–37, 2015.

[100] J. Kotakoski, J. Meyer, S. Kurasch, D. Santos-Cottin, U. Kaiser, and A. Krasheninnikov, "Stone-Wales-type transformations in carbon nanostructures driven by electron irradiation," *Physical Review B*, vol. 83, no. 24, p. 245420, 2011.

[101] L. Li, S. Reich, and J. Robertson, "Defect energies of graphite: Density-functional calculations," *Physical Review B*, vol. 72, no. 18, p. 184109, 2005.

[102] O. V. Yazyev, I. Tavernelli, U. Rothlisberger, and L. Helm, "Early stages of radiation damage in graphite and carbon nanostructures: A first-principles molecular dynamics study," *Physical Review B*, vol. 75, no. 11, p. 115418, 2007.

[103] Z. Zhu, X. Yang, M. Huang, Q. He, G. Yang, and Z. Wang, "Mechanisms governing phonon scattering by topological defects in graphene nanoribbons," *Nanotechnology*, vol. 27, no. 5, p. 055401, 2015.

[104] H. F. Bettinger, B. I. Yakobson, and G. E. Scuseria, "Scratching the surface of buckminsterfullerene: the barriers for Stone-Wales transformation through symmetric and asymmetric transition states," *Journal of the American Chemical Society*, vol. 125, no. 18, pp. 5572–5580, 2003.

[105] Z. Wang, Y. Zhou, J. Bang, M. P. Prange, S. Zhang, and F. Gao, "Modification of defect structures in graphene by electron irradiation: *Ab initio* molecular dynamics simulations," *The Journal of Physical Chemistry C*, vol. 116, no. 30, pp. 16070–16079, 2012.

[106] W. Zhang, W.-C. Lu, H.-X. Zhang, K. Ho, and C. Wang, "Tight-binding calculation studies of vacancy and adatom defects in graphene," *Journal of Physics: Condensed Matter*, vol. 28, no. 11, p. 115001, 2016.

[107] A. Krasheninnikov and K. Nordlund, "Ion and electron irradiation-induced effects in nanostructured materials," *Journal of applied physics*, vol. 107, no. 7, p. 3, 2010.

[108] S. J. Stuart, A. B. Tutein, and J. A. Harrison, “A reactive potential for hydrocarbons with intermolecular interactions,” *The Journal of chemical physics*, vol. 112, no. 14, pp. 6472–6486, 2000.

[109] R. Rafiee and R. M. Moghadam, “On the modeling of carbon nanotubes: a critical review,” *Composites Part B: Engineering*, vol. 56, pp. 435–449, 2014.

[110] B. Ni, S. B. Sinnott, P. T. Mikulski, and J. A. Harrison, “Compression of carbon nanotubes filled with C_{60}, CH_4, or Ne: predictions from molecular dynamics simulations,” *Physical review letters*, vol. 88, no. 20, p. 205505, 2002.

[111] A. Krasheninnikov, F. Banhart, J. Li, A. S. Foster, and R. M. Nieminen, “Stability of carbon nanotubes under electron irradiation: role of tube diameter and chirality,” *Physical review B*, vol. 72, no. 12, p. 125428, 2005.

[112] A. Zobelli, A. Gloter, C. Ewels, G. Seifert, and C. Colliex, “Electron knock-on cross section of carbon and boron nitride nanotubes,” *Physical Review B*, vol. 75, no. 24, p. 245402, 2007.

[113] A. Merrill, C. D. Cress, J. E. Rossi, N. D. Cox, and B. J. Landi, “Threshold displacement energies in graphene and single-walled carbon nanotubes,” *Physical Review B*, vol. 92, no. 7, p. 075404, 2015.

[114] S. T. Skowron, I. V. Lebedeva, A. M. Popov, and E. Bichoutskaia, “Energetics of atomic scale structure changes in graphene,” *Chemical Society Reviews*, vol. 44, no. 10, pp. 3143–3176, 2015.

[115] A. W. Robertson, C. S. Allen, Y. A. Wu, K. He, J. Olivier, J. Neethling, A. I. Kirkland, and J. H. Warner, “Spatial control of defect creation in graphene at the nanoscale,” *Nature communications*, vol. 3, p. 1144, 2012.

[116] L. Liu, M. Qing, Y. Wang, and S. Chen, “Defects in graphene: generation, healing, and their effects on the properties of graphene: a review,” *Journal of Materials Science & Technology*, vol. 31, no. 6, pp. 599–606, 2015.

[117] S. H. M. Jafri, K. Carva, E. Widenkvist, T. Blom, B. Sanyal, J. Fransson, O. Eriksson, U. Jansson, H. Grennberg, O. Karis, *et al.*, “Conductivity engineering of graphene by defect formation,” *Journal of Physics D: Applied Physics*, vol. 43, no. 4, p. 045404, 2010.

[118] J.-H. Chen, W. G. Cullen, C. Jang, M. Fuhrer, and E. D. Williams, “Defect scattering in graphene,” *Physical review letters*, vol. 102, no. 23, p. 236805, 2009.

[119] A. Lherbier, S. M.-M. Dubois, X. Declerck, Y.-M. Niquet, S. Roche, and J.-C. Charlier, “Transport properties of graphene containing structural defects,” *Physical Review B*, vol. 86, no. 7, p. 075402, 2012.

[120] A. Zandiatashbar, G.-H. Lee, S. J. An, S. Lee, N. Mathew, M. Terrones, T. Hayashi, C. R. Picu, J. Hone, and N. Koratkar, "Effect of defects on the intrinsic strength and stiffness of graphene," *Nature communications*, vol. 5, p. 3186, 2014.

[121] D. Boukhvalov and M. Katsnelson, "Chemical functionalization of graphene with defects," *Nano letters*, vol. 8, no. 12, pp. 4373–4379, 2008.

[122] R. Faccio, L. Fernández-Werner, H. Pardo, C. Goyenola, O. N. Ventura, and Á. W. Mombrú, "Electronic and structural distortions in graphene induced by carbon vacancies and boron doping," *The Journal of Physical Chemistry C*, vol. 114, no. 44, pp. 18961–18971, 2010.

[123] R. Beams, L. G. Cançado, and L. Novotny, "Raman characterization of defects and dopants in graphene," *Journal of Physics: Condensed Matter*, vol. 27, no. 8, p. 083002, 2015.

[124] J.-K. Huang, J. Pu, C.-L. Hsu, M.-H. Chiu, Z.-Y. Juang, Y.-H. Chang, W.-H. Chang, Y. Iwasa, T. Takenobu, and L.-J. Li, "Large-area synthesis of highly crystalline WSe_2 monolayers and device applications," *ACS nano*, vol. 8, no. 1, pp. 923–930, 2013.

[125] V. Podzorov, M. Gershenson, C. Kloc, R. Zeis, and E. Bucher, "High-mobility field-effect transistors based on transition metal dichalcogenides," *Appl. Phys. Lett.*, vol. 84, no. 17, pp. 3301–3303, 2004.

[126] H. Fang, S. Chuang, T. C. Chang, K. Takei, T. Takahashi, and A. Javey, "High-performance single layered WSe_2 p-FETs with chemically doped contacts," *Nano Lett.*, vol. 12, no. 7, pp. 3788–3792, 2012.

[127] S. Das and J. Appenzeller, "WSe_2 field effect transistors with enhanced ambipolar characteristics," *Appl. Phys. Lett.*, vol. 103, no. 10, p. 103501, 2013.

[128] S. M. Eichfeld, L. Hossain, Y.-C. Lin, A. F. Piasecki, B. Kupp, A. G. Birdwell, R. A. Burke, N. Lu, X. Peng, J. Li, *et al.*, "Highly scalable, atomically thin WSe_2 grown via metal–organic chemical vapor deposition," *ACS nano*, vol. 9, no. 2, pp. 2080–2087, 2015.

[129] H. Liu, L. Jiao, L. Xie, F. Yang, J. Chen, W. Ho, C. Gao, J. Jia, X. Cui, and M. Xie, "Molecular-beam epitaxy of monolayer and bilayer WSe_2: a scanning tunneling microscopy/spectroscopy study and deduction of exciton binding energy," *2D Mater.*, vol. 2, no. 3, p. 034004, 2015.

[130] S. Das, R. Gulotty, A. V. Sumant, and A. Roelofs, "All two-dimensional, flexible, transparent, and thinnest thin film transistor," *Nano Lett.*, vol. 14, no. 5, pp. 2861–2866, 2014.

[131] H.-J. Chuang, X. Tan, N. J. Ghimire, M. M. Perera, B. Chamlagain, M. M.-C. Cheng, J. Yan, D. Mandrus, D. Tománek, and Z. Zhou, "High mobility WSe_2 p-and n-type field-effect transistors contacted by highly doped graphene for low-resistance contacts," *Nano Lett.*, vol. 14, no. 6, pp. 3594–3601, 2014.

[132] B. W. Baugher, H. O. Churchill, Y. Yang, and P. Jarillo-Herrero, "Optoelectronic devices based on electrically tunable p–n diodes in a monolayer dichalcogenide," *Nature Nanotechnol.*, vol. 9, no. 4, pp. 262–267, 2014.

[133] S. Mathew, T. Chan, D. Zhan, K. Gopinadhan, A.-R. Barman, M. Breese, S. Dhar, Z. Shen, T. Venkatesan, and J. T. Thong, "The effect of layer number and substrate on the stability of graphene under MeV proton beam irradiation," *Carbon*, vol. 49, no. 5, pp. 1720–1726, 2011.

[134] C. Abromeit, "Aspects of simulation of neutron damage by ion irradiation," *J. Nucl. Mater.*, vol. 216, pp. 78–96, 1994.

[135] D. Mazey, "Fundamental aspects of high-energy ion-beam simulation techniques and their relevance to fusion materials studies," *J. Nucl. Mater.*, vol. 174, no. 2, pp. 196–209, 1990.

[136] W. Oldham and A. Milnes, "Interface states in abrupt semiconductor heterojunctions," *Solid-State Electronics*, vol. 7, no. 2, pp. 153–165, 1964.

[137] E. Stassinopoulos and J. P. Raymond, "The space radiation environment for electronics," *Proc. IEEE.*, vol. 76, no. 11, pp. 1423–1442, 1988.

[138] W. Jaegermann and D. Schmeisser, "Reactivity of layer type transition metal chalcogenides towards oxidation," *Surf. Sci.*, vol. 165, no. 1, pp. 143–160, 1986.

[139] M. Yamamoto, S. Dutta, S. Aikawa, S. Nakaharai, K. Wakabayashi, M. S. Fuhrer, K. Ueno, and K. Tsukagoshi, "Self-limiting layer-by-layer oxidation of atomically thin WSe_2," *Nano Lett.*, vol. 15, no. 3, pp. 2067–2073, 2015.

[140] P. Zhao, D. Kiriya, A. Azcatl, C. Zhang, M. Tosun, Y.-S. Liu, M. Hettick, J. S. Kang, S. McDonnell, S. KC, *et al.*, "Air stable p-doping of WSe_2 by covalent functionalization," *ACS nano*, vol. 8, no. 10, pp. 10808–10814, 2014.

[141] Z. Li, S. Yang, R. Dhall, E. Kosmowska, H. Shi, I. Chatzakis, and S. B. Cronin, "Layer control of WSe_2 via selective surface layer oxidation," *ACS nano*, vol. 10, no. 7, pp. 6836–6842, 2016.

[142] A. Azcatl, K. Santosh, X. Peng, N. Lu, S. McDonnell, X. Qin, F. de Dios, R. Addou, J. Kim, M. J. Kim, *et al.*, "HfO_2 on UV–O_3 exposed transition metal dichalcogenides: interfacial reactions study," *2D Materials*, vol. 2, no. 1, p. 014004, 2015.

[143] E. Kraut, R. Grant, J. Waldrop, and S. Kowalczyk, "Precise determination of the valence-band edge in X-ray photoemission spectra: Application to measurement of semiconductor interface potentials," *Phys. Rev. Lett.*, vol. 44, no. 24, p. 1620, 1980.

[144] M.-H. Chiu, C. Zhang, H.-W. Shiu, C.-P. Chuu, C.-H. Chen, C.-Y. S. Chang, C.-H. Chen, M.-Y. Chou, C.-K. Shih, and L.-J. Li, "Determination of band alignment in the single-layer MoS_2/WSe_2 heterojunction," *Nat. Commun.*, vol. 6, 2015.

[145] Q. Jing, G. Wu, Y. Zhang, F. Gao, X. Cai, Y. Zhao, W. Li, and G. Du, "Band alignment of InN/6H-SiC heterojunction determined by X-ray photoelectron spectroscopy," *Appl. Phys. Lett.*, vol. 105, no. 6, p. 063510, 2014.

[146] C. J. McHargue and J. Williams, "Ion implantation effects in silicon carbide," *Nucl. Instr. Meth. Phys. Res. B*, vol. 80, pp. 889–894, 1993.

[147] W. Weber, L. Wang, N. Yu, and N. Hess, "Structure and properties of ion-beam-modified (6H) silicon carbide," *Mater. Sci. Eng. A*, vol. 253, no. 1, pp. 62–70, 1998.

[148] A. A. Lebedev, D. Davydov, A. N. Kuznetsov, E. V. Bogdanova, V. V. Kozlovski, N. Savkina, *et al.*, "Deep centres appearing in 6H and 4H SiC after proton irradiation," in *Mater. Sci. Forum*, vol. 338, pp. 973–976, Trans Tech Publ, 2000.

[149] T. Dalibor, G. Pensl, H. Matsunami, T. Kimoto, W. Choyke, A. Schöner, and N. Nordell, "Deep defect centers in silicon carbide monitored with deep level transient spectroscopy," *Phys. Status Solidi A*, vol. 162, no. 1, pp. 199–225, 1997.

[150] L. Henry, M.-F. Barthe, C. Corbel, P. Desgardin, G. Blondiaux, S. Arpiainen, and L. Liszkay, "Silicon vacancy-type defects in as-received and 12-MeV proton-irradiated 6H - SiC studied by positron annihilation spectroscopy," *Phys. Rev. B*, vol. 67, no. 11, p. 115210, 2003.

[151] W. Puff, A. G. Balogh, and P. Mascher, "Vacancy-type defects in proton-irradiated 6H-and 4H-SiC: A systematic study with positron annihilation techniques," in *Mater. Sci. Forum*, vol. 338, pp. 969–972, Trans Tech Publ, 2000.

[152] P. Xia, X. Feng, R. J. Ng, S. Wang, D. Chi, C. Li, Z. He, X. Liu, and K.-W. Ang, "Impact and origin of interface states in MOS capacitor with monolayer MoS_2 and HfO_2 high-k dielectric," *Scientific reports*, vol. 7, p. 40669, 2017.

[153] S. Zhang, C.-G. Wang, M.-Y. Li, D. Huang, L.-J. Li, W. Ji, and S. Wu, "Defect structure of localized excitons in a WSe_2 monolayer," *Physical review letters*, vol. 119, no. 4, p. 046101, 2017.

[154] H. Kobayashi, T. Sakurai, M. Takahashi, and Y. Nishioka, "Interface states at SiO_2/6H-SiC (0001) interfaces observed by X-ray photoelectron spectroscopy measurements under bias: Comparison between dry and wet oxidation," *Physical Review B*, vol. 67, no. 11, p. 115305, 2003.

[155] R. C. Walker, G. R. Bhimanapati, T. Shi, K. Zhang, S. M. Eichfeld, I. Jovanovic, and J. A. Robinson, "Stability of semiconducting transition metal dichalcogenides irradiated by soft X-rays and low energy electrons," *Applied Physics Letters*, vol. 110, no. 17, p. 173102, 2017.

[156] S. Zhou, Ç. Girit, A. Scholl, C. Jozwiak, D. Siegel, P. Yu, J. Robinson, F. Wang, A. Zettl, and A. Lanzara, "Instability of two-dimensional graphene: Breaking sp^2 bonds with soft X-rays," *Physical Review B*, vol. 80, no. 12, p. 121409, 2009.

[157] O. Lang, Y. Tomm, R. Schlaf, C. Pettenkofer, and W. Jaegermann, "Single crystalline GaSe/WSe_2 heterointerfaces grown by van der Waals epitaxy. II. junction characterization," *Journal of applied physics*, vol. 75, no. 12, pp. 7814–7820, 1994.

[158] M. Bozack, "Surface studies on SiC as related to contacts," *physica status solidi (b)*, vol. 202, no. 1, pp. 549–580, 1997.

[159] M. Tangi, P. Mishra, C.-C. Tseng, T. K. Ng, M. N. Hedhili, D. H. Anjum, M. S. Alias, N. Wei, L.-J. Li, and B. S. Ooi, "Band alignment at GaN/single-layer WSe_2 interface," *ACS applied materials & interfaces*, vol. 9, no. 10, pp. 9110–9117, 2017.

[160] C.-H. Chen, C.-L. Wu, J. Pu, M.-H. Chiu, P. Kumar, T. Takenobu, and L.-J. Li, "Hole mobility enhancement and p-doping in monolayer WSe_2 by gold decoration," *2D Materials*, vol. 1, no. 3, p. 034001, 2014.

[161] S. Seidel, "Recent results on diamond radiation tolerance," *Journal of Instrumentation*, vol. 9, no. 01, p. C01013, 2014.

[162] P. A. Newman and H. Wegener, "Effect of electron radiation on silicon nitride insulated gate field effect transistors," *IEEE Transactions on Nuclear Science*, vol. 14, no. 6, pp. 293–298, 1967.

[163] V. Brasch, Q.-F. Chen, S. Schiller, and T. J. Kippenberg, "Radiation hardness of high-Q silicon nitride microresonators for space compatible integrated optics," *Optics express*, vol. 22, no. 25, pp. 30786–30794, 2014.

[164] J. Felix, J. Schwank, D. M. Fleetwood, M. Shaneyfelt, and E. P. Gusev, "Effects of radiation and charge trapping on the reliability of high-κ gate dielectrics," *Microelectronics Reliability*, vol. 44, no. 4, pp. 563–575, 2004.

[165] N. Alov, D. Kutsko, I. Spirovova, and Z. Bastl, "XPS study of vanadium surface oxidation by oxygen ion bombardment," *Surface Science*, vol. 600, no. 8, pp. 1628–1631, 2006.

[166] N. V. Alov, "Surface oxidation of metals by oxygen ion bombardment," *Nuclear Instruments and Methods in Physics Research Section B: Beam Interactions with Materials and Atoms*, vol. 256, no. 1, pp. 337–340, 2007.

[167] S. Dhar, O. Seitz, M. D. Halls, S. Choi, Y. J. Chabal, and L. C. Feldman, "Chemical properties of oxidized silicon carbide surfaces upon etching in hydrofluoric acid," *J. Am. Chem. Soc.*, vol. 131, no. 46, pp. 16808–16813, 2009.

[168] T. Taylor, "The surface composition of silicon carbide powders and whiskers: An XPS study," *J. Mater. Res.*, vol. 4, no. 01, pp. 189–203, 1989.

[169] C. Serre, L. Calvo-Barrio, A. Pérez-Rodríguez, A. Romano-Rodríguez, J. Morante, Y. Pacaud, R. Kögler, V. Heera, and W. Skorupa, "Ion-beam synthesis of amorphous SiC films: Structural analysis and recrystallization," *J. Appl. Phys.*, vol. 79, no. 9, pp. 6907–6913, 1996.

[170] M. D. Hampton, *Hydrogen Materials Science and Chemistry of Metal Hydrides*, vol. 71. Springer Science & Business Media, 2002.

[171] J. Alay and M. Hirose, "The valence band alignment at ultrathin SiO_2/Si interfaces," *J. Appl. Phys.*, vol. 81, no. 3, pp. 1606–1608, 1997.

[172] T. R. Oldham and F. McLean, "Total ionizing dose effects in MOS oxides and devices," *IEEE Transactions on Nuclear Science*, vol. 50, no. 3, pp. 483–499, 2003.

[173] S. Mouri, Y. Miyauchi, and K. Matsuda, "Tunable photoluminescence of monolayer MoS_2 via chemical doping," *Nano letters*, vol. 13, no. 12, pp. 5944–5948, 2013.

[174] H. Terrones, F. López-Urías, and M. Terrones, "Novel hetero-layered materials with tunable direct band gaps by sandwiching different metal disulfides and diselenides," *Scientific reports*, vol. 3, p. 1549, 2013.

[175] K. F. Mak, C. Lee, J. Hone, J. Shan, and T. F. Heinz, "Atomically thin MoS_2: a new direct-gap semiconductor," *Physical review letters*, vol. 105, no. 13, p. 136805, 2010.

[176] W. Wu, D. De, S.-C. Chang, Y. Wang, H. Peng, J. Bao, and S.-S. Pei, "High mobility and high on/off ratio field-effect transistors based on chemical vapor deposited single-crystal MoS_2 grains," *Applied Physics Letters*, vol. 102, no. 14, p. 142106, 2013.

[177] Z. Fan, Z. Wei-Bing, and T. Bi-Yu, "Electronic structures and elastic properties of monolayer and bilayer transition metal dichalcogenides MX_2 (M= Mo, W; X= O, S, Se, Te): a comparative first-principles study," *Chinese Physics B*, vol. 24, no. 9, p. 097103, 2015.

[178] R. Lv, J. A. Robinson, R. E. Schaak, D. Sun, Y. Sun, T. E. Mallouk, and M. Terrones, "Transition metal dichalcogenides and beyond: synthesis, properties, and applications of single-and few-layer nanosheets," *Accounts of chemical research*, vol. 48, no. 1, pp. 56–64, 2014.

[179] S. Das, H.-Y. Chen, A. V. Penumatcha, and J. Appenzeller, "High performance multilayer MoS_2 transistors with scandium contacts," *Nano letters*, vol. 13, no. 1, pp. 100–105, 2012.

[180] H. Iwai, "Future of nano CMOS technology," *Solid-State Electronics*, vol. 112, pp. 56–67, 2015.

[181] J. R. Schwank, M. R. Shaneyfelt, D. M. Fleetwood, J. A. Felix, P. E. Dodd, P. Paillet, and V. Ferlet-Cavrois, "Radiation effects in MOS oxides," *IEEE Transactions on Nuclear Science*, vol. 55, no. 4, pp. 1833–1853, 2008.

[182] P. Dhakras, P. Agnihotri, H. Bakhru, H. L. Hughes, and J. U. Lee, "TID effects in reconfigurable MOSFETs using 2-D semiconductor WSe_2," *IEEE Transactions on Nuclear Science*, vol. 65, no. 1, pp. 53–57, 2017.

[183] M.-Y. Lu, S.-C. Wu, H.-C. Wang, and M.-P. Lu, "Time-evolution of the electrical characteristics of MoS_2 field-effect transistors after electron beam irradiation," *Physical Chemistry Chemical Physics*, vol. 20, no. 14, pp. 9038–9044, 2018.

[184] C. X. Zhang, A. Newaz, B. Wang, E. X. Zhang, G. X. Duan, D. M. Fleetwood, M. L. Alles, R. D. Schrimpf, K. I. Bolotin, and S. T. Pantelides, "Electrical stress and total ionizing dose effects on MoS_2 transistors," *IEEE Transactions on Nuclear Science*, vol. 61, no. 6, pp. 2862–2867, 2014.

[185] S. Hong, D. Fu, J. Hou, D. Zhou, B. Wang, Y. Sun, P. Liu, and K. Liu, "Robust photoluminescence energy of MoS_2/graphene heterostructure against electron irradiation," *Science China Materials*, vol. 61, no. 10, pp. 1351–1359, 2018.

[186] W.-K. Hong, C. Lee, D. Nepal, K. E. Geckeler, K. Shin, and T. Lee, "Radiation hardness of the electrical properties of carbon nanotube network field effect transistors under high-energy proton irradiation," *Nanotechnology*, vol. 17, no. 22, p. 5675, 2006.

[187] Y. Zhao, D. Li, L. Xiao, J. Liu, X. Xiao, G. Li, Y. Jin, K. Jiang, J. Wang, S. Fan, *et al.*, "Radiation effects and radiation hardness solutions for single-walled carbon nanotube-based thin film transistors and logic devices," *Carbon*, vol. 108, pp. 363–371, 2016.

[188] D. A. Neamen, *Semiconductor physics and devices: basic principles*. New York, NY: McGraw-Hill,, 2012.

[189] D. Fleetwood, P. Winokur, R. Reber Jr, T. Meisenheimer, J. Schwank, M. Shaneyfelt, and L. Riewe, "Effects of oxide traps, interface traps, and "border traps" on metal-oxide-semiconductor devices," *Journal of Applied Physics*, vol. 73, no. 10, pp. 5058–5074, 1993.

[190] K. Liu, C.-L. Hsin, D. Fu, J. Suh, S. Tongay, M. Chen, Y. Sun, A. Yan, J. Park, K. M. Yu, *et al.*, "Self-passivation of defects: effects of high-energy particle irradiation on the elastic modulus of multilayer graphene," *Advanced Materials*, vol. 27, no. 43, pp. 6841–6847, 2015.

[191] D. W. Brenner, O. A. Shenderova, J. A. Harrison, S. J. Stuart, B. Ni, and S. B. Sinnott, "A second-generation reactive empirical bond order (REBO) potential energy expression for hydrocarbons," *Journal of Physics: Condensed Matter*, vol. 14, no. 4, p. 783, 2002.

[192] T. Liang, S. R. Phillpot, and S. B. Sinnott, "Parametrization of a reactive many-body potential for Mo–S systems," *Physical Review B*, vol. 79, no. 24, p. 245110, 2009.

[193] J. A. Stewart and D. Spearot, "Atomistic simulations of nanoindentation on the basal plane of crystalline molybdenum disulfide (MoS_2)," *Modelling and Simulation in Materials Science and Engineering*, vol. 21, no. 4, p. 045003, 2013.

[194] P. Young, "Lattice parameter measurements on molybdenum disulphide," *Journal of Physics D: Applied Physics*, vol. 1, no. 7, p. 936, 1968.

[195] S. M. Sze *et al.*, *Modern semiconductor device physics*. John Wiley, 1998.

[196] D. M. Fleetwood, "Evolution of total ionizing dose effects in MOS devices with moore's law scaling," *IEEE Transactions on Nuclear Science*, vol. 65, no. 8, pp. 1465–1481, 2017.

[197] E. Stassinopoulos, O. Van Gunten, G. Brucker, A. Knudson, and T. Jordan, "The damage equivalence of electrons, protons, alphas and gamma rays in rad-hard MOS devices," *IEEE Transactions on Nuclear Science*, vol. 30, no. 6, pp. 4363–4367, 1983.

[198] M. R. H. Kinnison, James D and T. M. Jordan, "Estimation of the charged particle environment for earth orbits," *Johns Hopkins APL Technical Digest*, vol. 11, no. 3 and 4, pp. 300–309, 1990.